Spectroscopic investigation of deposited InP nanocrystals and small Cu clusters

Dissertation

Zur Erlangung des Doktorgrades
des Fachbereichs Physik
der Universität Hamburg

vorgelegt von
Mihai Sorin Adam
aus Braşov/Rumänien

Hamburg
2004

Gutachter der Dissertation :	Priv. Doz. Dr. T. Möller
	Prof. Dr. W. Hansen
Gutachter der Disputation:	Priv. Doz. Dr. T. Möller
	Prof. Dr. R. L. Johnson
Datum der Disputation:	4 Juni 2004
Vorsitzender des Prüfungsausschusses	Dr. H. D. Rüter
Vorsitzender des Promotionsausschusses:	Prof. Dr. R. Wiesendanger
Dekan des Fachbereichs Physik:	Prof. Dr. G. Huber

Abstract

Indium phosphide (InP) nanocrystals with mean particle diameter in the 3-4 nm range and size distribution 8-10% of the average diameter were synthesized by methods of colloidal chemistry. Capping of the nanocrystal surface with a shell of organic ligands allowed both the achievement of a high stability of nanocrystalline properties and the solubility of particles in different solvents. InP nanocrystals with enhanced photoluminescence (PL) efficiency were obtained by photo-assisted etching of the nanocrystal surface with hydrofluoric acid (HF); the PL quantum efficiency of the resulting InP nanocrystals was about three orders of magnitude higher than the "as prepared" InP samples and approached ~ 40% at room temperature. Photoelectron Spectroscopy (PES) with synchrotron radiation was used to reveal the changes of the nanocrystals that were responsible for the dramatic improvement of the PL efficiency. The analysis of high resolution In 3d and P 2p core-levels confirmed significant changes of the nanocrystal surface structure. These changes were induced by the post-preparative nanocrystals treatments and allowed the proposal of a model for the etching mechanism. The photo-assisted treatment of InP nanocrystals selectively removes phosphorus atoms from the nanocrystal surface. These atoms form surface states located inside the band gap of the "as-prepared" InP nanocrystals and provide non-radiative recombination pathways.

With the pick-up method, Cu atoms are loaded into host Ar clusters. This results in the formation of small Cu clusters with a broad size distribution (50% of the average size). The average sizes of the resulting clusters were measured to be approx. 5-15 atoms/cluster using a Time of Flight Mass Spectrometer. The spectroscopic investigation was performed on deposited Cu clusters embedded in an Ar matrix. The samples were deposited on a cold substrate (10K). The depth homogeneity and stability of the deposited clusters were monitored with help of PES. The main investigation method for the Cu cluster was X-ray Absorption Spectroscopy (XAS) in the X-ray Absorption Near Edge Structure (XANES) regime, yielding information about the electronic and geometric structure of the deposited clusters. For better statistics, the acquisition of the absorption spectra for Cu $L_{3,2}$ edge was performed simultaneously in two different modes: Total Electron Yield (TEY) and Auger Yield. XANES spectra (Ar $L_{3,2}$ edge) were also recorded for pure or Cu doped Ar matrices. The Cu clusters had icosahedral structure with a bond length of approx. 2. 23 Å which was around ~ 6% shorter than the Cu single crystal (2.556 Å). Spectroscopic measurements revealed that already for 5-6 atoms/cluster, electrons from the 3d band had already partially hybridized with the 4s band.

Kurzfassung

InP-Nanokristalle mit einer mittleren Partikelgröße im Bereich 3-4 nm und einer enge Größenverteilung (8-10 % des mittleren Durchmessers) wurden mit Hilfe der Kolloid-Chemie synthetisiert. Durch die Bedeckung der Nanokristalloberfläche mit einer Schicht aus organischen Liganden wurde eine hohe Stabilität der Eigenschaften der Nanokristalle sowie gute Lösbarkeit der Partikel in verschiedenen Lösungsmitteln erreicht. InP-Nanokristalle mit verbesserter Effizienz der Photolumineszenz (PL) wurden durch photounterstütztes Ätzen der Nanokristalloberfläche mit HF erzeugt; die PL-Quanteneffizienz ist etwa drei Größenordnungen höher im Vergleich zu den unbehandelten InP-Proben und erreicht ~ 40 % bei Raumtemperatur. Mit Hilfe der Photoelektronenspektroskopie (PES) konnten Veränderungen der Nanokristalle nachgewiesen werden, die zu dieser deutlichen Verbesserung der PL-Effizienz geführt haben. Eine Analyse von hochaufgelösten Messungen der In 3d und P 2p Rumpfzustände bestätigte, dass signifikante Änderungen der Struktur der Nanokristalloberfläche durch die postpräperative Behandlung der Nanokristalle auftreten und ermöglichte die Formulierung eines Modells für den Ätzmechanismus. Das photounterstütze Ätzen der InP-Nanokristalle entfernt selektiv Phosphoratome aus der Nanokristalloberfläche, die in unbehandelten InP-Nanokristallen Oberflächenzustände in der Bandlücke bilden und so zu nichtstrahlender Rekombination führen.

Weiterhin wurden mit der "Pick-up"-Methode Cu-Atome in Ar-Cluster eingelagert auf diese Weise und kleine Cu-Cluster mit einer relativ schmalen Größenverteilung erzeugt. Die mittlere Größen der resultierenden Cluster von ca. 5-15 Atomen pro Cluster wurden mit einem Flugzeit-Massenspektrometer bestimmt. Spektroskopisch wurden deponierte Cu-Cluster, eingebettet in eine Ar-Matrix, untersucht. Die Proben wurden auf einem kalten Substrat (10 K) deponiert. Die Homogenität über die Tiefe und die Stabilität der deponierten Proben wurden mittels PES bestimmt. Die wichtigste Untersuchungsmethode für die Cu-Cluster war die Röntgenabsorptionsspektroskopie ("X-Ray Absorption Spectroscopy", XAS) im XANES-Bereich ("X-Ray Absorption Near Edge Structure"), die Informationen über die elektronische und geometrische Struktur der deponierten Proben liefert. Um die Statistik zu verbessern wurden die Absorptionsspektren für die Cu $L_{2,3}$-Kante simultan mit zwei Messverfahren, der Gesamtelektronausbeute (TEY, "Total Electron Yield") und der Auger-Ausbeute aufgenommen. XANES-Spektren wurden ausserdem für reine und Cu-dotierte Ar-Matritzen aufgenommen. Die Clusters besitzen Ikosahedral-Struktur mit einer um 6% kleiner Bindungslänger als in Festkörper. Die Röntgenabsorption Messungen zeigen, dass bereits bei 5-6 Atomen, Elektronen aus den 3d Band das 4s Band partiell füllen.

Content

Abstract

Kurzfassung

1. Introduction 1

2. The experimental setup 5
   2.1 General layout 5
   2.2 Devices 11
      2.2.1 The cluster source 11
      2.2.2 The oven 12
      2.2.3 Manipulator + cryostat: TEY detection 14
      2.2.4 The electron analyzer 16
      2.2.5 The sputter ion gun 18
      2.2.6 The x-ray source 18
      2.2.7 The transfer system 19
      2.2.8 The reflectron time of flight spectrometer 19
   2.3 Synchrotron radiation-the BW3 beamline 21
   2.4 The alignment of the setup 22
      2.4.1 The alignment for the cluster experiment 22
      2.4.2 The alignment of the analyzer chamber 22

3. Investigation techniques 25
   3.1 Photoelectron spectroscopy 25
   3.2 X-ray absorption 28
   3.3 Instrumental resolution; core level spectra 33

4. InP nanocrystals 37
   4.1 Preparation of InP nanocrystals 38
   4.2 Bulk InP (110) surface 41

4.2.1 Clean InP (110) surface 41
4.2.2 Oxidation of InP(110) surface 47
4.3 Photoelectron spectra of InP nanocrystals 51
4.3.1 InP as prepared nanocrystals 51
4.3.2 InP methanol washed 58
4.3.3 InP pyridine 60
4.3.4 InP oxidized 64
4.3.5 InP nanocrystals HF etched under nitrogen atmosphere 66
4.3.6 Highly luminescent InP etched nanocrystals 69
4.3.7 TOPO capped sample 72
4.3.8 TOPO capped sample-HF etched 74
4.3.9 In 3d core-level spectra 80
4.4 Discussion of the etching mechanism. Conclusion 81

5. Cu clusters 91
5.1 Cluster production and deposition 92
5.2 Mass spectra and deposition of Cu clusters 97
5.3 X-ray photoelectron spectroscopy investigation 99
5.4 Absorption spectra 105
5.4.1 The Ar XANES 105
5.4.2 The Cu XANES 107
5.5 The theoretical simulated spectra. Comparison with the experiment 117
5.6 The case of Cu islands on Au substrate 121

6. Summary 125

Acknowledgements

References

Chapter 1. Introduction

In the early days of the physical sciences, the main goal of the researchers was to determine the elementary constituents of matter (atoms, molecules, nuclei). Since many basics aspects are essentially understood now, a present challenge for science is to use atoms and molecules as building blocks for new materials with remarkable variations in fundamental electrical, optical and magnetic properties relative to the "infinitely extended" solid [1, 2]. In this context, the field of clusters and nanocrystals, which concerns the ensembles of a few atoms to a few thousands of atoms, appears especially fascinating, since these systems are intermediate between small molecules and bulk solids.

Nowadays, technological developments permit the synthesis and characterization of clusters consisting of virtually any chemical element (or combination of different elements) in the periodic table. The advances in theoretical calculations allow fundamental understanding of these new materials and also have a predictive capability to guide new experimental work.

There are several ways of producing nanoparticles. "Gas-phase" cluster synthesis (supersonic jets, gas aggregation, laser vaporization, ion sputtering) allows mass selection and size determination of the resulting clusters. Clusters of different materials can be prepared by gas aggregation [3], laser vaporization [4] and ion sputtering [5, 6] techniques. Detailed information is available in the literature.
In case of "chemical" synthesis the nanocrystals are typically grown in solution around small nuclei [7]. The resulting metallic or semiconductor nanoparticles are surrounded (passivated) by shells of organic ligands (see chapter 4) and size selection methods are very successful. The resulting nanostructures are stable in solution at room temperature and can often be handled like ordinary chemical substances facilitating further treatments or ligand exchange.
The surface growth modes, such as Stranski-Krastanov [8] are self-assembly techniques. The substrate nature and orientation play a decisive role and only a limited number of substances can be deposed by means of molecular beam epitaxy (MBE). Ultra high vacuum (UHV) conditions are also required.

Semiconductor clusters and nanocrystals are especially interesting materials since they exhibit strongly size dependent optical and electrical properties.
The investigation of the size selected semiconductor InP nanocrystals (3-4 nm diameter) using **photoelectron spectroscopy (PES)** technique is presented in the first part of this work. Quantum

confinement theory predicts that the band gap of a semiconductor nanocrystal increases compared to bulk values with decreasing particle size, and, below a critical threshold the material features are determined not only by its chemical composition, but also by the size.

The "chemical" synthesis and first characterization such as **T**ransmission **E**lectron **M**icroscopy (**TEM**), **X**-**r**ay **D**iffraction (**XRD**), **P**hoto-**l**uminescence (**PL**) quantum efficiency of the InP samples were done by the Weller group, Institute for Physical Chemistry, University of Hamburg.

One of the major challenges is the fabrication of nanocrystals exhibiting high photoluminescence efficiency. Luminescent nanocrystals attract steadily growing interest as long-lived dyes for optical microscopy of biological samples [9], emitting species in hybrid LED's [10], etc. The main obstacles for achieving efficient photoluminescence are the unpassivated atoms on the nanoparticle surface that provide energy states inside the band gap. Organically capped II-VI and III-V semiconductor nanocrystals still display a number of unpassivated surface sites, due to the nature of the passivation by organic ligands. It is very difficult, for example, to simultaneously passivate (cap) both anionic and cationic contributions at the surface with the same type of organic capping agent. Due to the finite number of atoms inside a nanocrystal, the high surface-to-volume ratio has dramatic effects, particularly for the optical and electronic properties. For example, in case of a 3 nm diameter InP nanocrystal, ~30% of its 1000 atoms are located at the particle surface. Therefore, the control of nanocrystal surface has been a critical issue to obtain nanocrystals with efficient and stable luminescence.

In case of InP, high PL quantum efficiency (up to 30%) is achieved with help of special treatments and one option is etching of the particle surface with certain fluorine compounds in the presence of light. High resolution photoelectron spectroscopy using synchrotron radiation is a powerful tool in the investigations of surfaces and interfaces. Since the inelastic mean free path length is a function of the photoelectron kinetic energy, one can vary the sampling depth, by simply tuning the photon energy. Hence, the photoelectron spectra of a particular core-level measured with different excitation energies make it possible to distinguish between the volume and the surface atoms from which one can establish the type of chemical bonds existing on the nanocrystal surface.

For a better understanding of the surface structure of InP nanocrystals and the changes occurring at the nanocrystals surface upon HF-treatment, the InP nanocrystals capped with different organic ligands like trioctylphosphine / trioctylphosphine oxide (TOP/TOPO) mixture and pyridine were investigated. Also, the investigation of InP nanocrystals etched with HF under various conditions is presented. A general description of the etching mechanism, based on the sample preparation and PES investigation is proposed.

The ideas behind the Cu cluster experiment were guided by two main aspects. The first one concerns a new method of preparation for thin films of embedded metal clusters. The second aspect is the understanding of the electronic and geometrical properties of small Cu clusters.

Small Cu clusters are produced by a pick-up technique [11]. In the first step, rare gas clusters are prepared using the method of supersonic jets [12]. Then, with the help of an oven [13], Cu atoms are evaporated and loaded (embedded) inside the host Ar rare gas clusters. This method has the advantage of producing cluster beams of pure or embedded clusters, with an average size and composition that can be conveniently tuned by simply modifying the pressure of the rare gas and temperature of the oven. The cluster beam structure can be monitored with the help of a time of flight mass-spectrometer. The electronic properties of Cu clusters embedded in Ar are preserved since the rare gas shell is chemically inert.

Samples consisting of thin films of embedded Cu clusters are deposited on cold substrates (10K) and investigated with help of spectroscopic methods.

The stability and homogeneity of the deposited clusters are monitored by means of the **PES** technique.

Absorption **N**ear **E**dge **S**tructure (**XANES**) with synchrotron radiation is a powerful tool for studying electronic and geometric structure of dilute, low range order systems. The **XANES** measurements can predict in a direct way the bond length and spatial orientation around the excited atoms inside the small Cu clusters.

The electronic structure of atomic Cu is known to be $[Ar]3d^{10}4s^{1}$ [124], but the bulk Cu is better describe by an $[Ar]3d^{10-x}\ 4s^{1+x}$ [126] like configuration with x=0.4. This variation is called *valence change* and investigation on small Cu clusters might provide information on the dynamic of the process.

The **XANES** measurements should indicate differences between a pure Ar matrix and a Cu doped one. There are changes expected also between the small Cu clusters embedded in Ar and the Cu bulk fcc structure. From theoretical predictions, an icosahedral like geometry is expected in case of Cu_{13} cluster. It will be interesting to compare the theoretical calculations with the experimental data.

At room temperature the Ar matrix evaporates and the small Cu clusters coagulate on the gold sample holder surface. A very important question is if the small metal clusters retain their properties even without the protective Ar shell. The measured absorption spectra have also to be compared with the published data corresponding to Cu-Au disordered alloys.

In conclusion, the main task of the present work is to shed light on the surface structure of the InP nanocrystals and the electronic and geometric structure of small Cu clusters.

Chapter 2 The experimental set-up: a combined cluster production and spectroscopic facility

The apparatus used to obtain the experimental data for the present work is described in this chapter.
The measurements on semiconductor nanocrystals prepared by chemical methods were done on an existing UHV setup, built up by Manfred Riedler [18]. The machine equipped with an electron analyzer is suitable for high resolution photoemission study on deposited samples by means of synchrotron radiation or classical x-ray sources. This setup was further up-graded to fill the complex requirements regarding the cluster production and *in-situ* cold deposition of the samples. The cluster characterization required new detectors; a *Time Of Flight* (*TOF)* spectrometer (mass determination), and a *Total Electron Yield (TEY)* counter (absorption measurements).
Also the existing detectors like the electron analyzer had to be reconfigured to a new operation modus, the so-called *Constant Final State Mode* (see section 2.2.4) for *Auger Yield* absorption measurements. Typically, the electron analyzer is operated in the *XPS* mode and the results are the photoemission spectra.
Because of the rather unusual combination of techniques, a fairly detailed description will be presented here, along with the rationale behind some of the design decisions.

2.1 General layout

One of the essential requirements for the cluster experiment was to design a set up that provides high intensity cluster beams inside the deposition chamber and Reflectron TOF mass spectrometer (see section 2.2.8) region combined with the possibility of investigating the deposited samples under UHV conditions.
The condition of having high intensity cluster beams in the deposition chamber is achieved with the help of a very compact design due to the fact that the intensity of the beam is proportional with $1/d^2$ where d is the distance from the source. In other words, the distance between cluster source and oven and distance between oven and deposition chamber (or Reflectron TOF in case of mass determination) should be as short as possible.
All the spectroscopic measurements are done using synchrotron radiation. Due to limited beam time the UHV conditions for the deposition chamber, analyzer chamber and the transfer system must be obtained after bake out (48 hours).

The Reflecton TOF cannot be baked out and for this reason a valve has to be installed between the mass spectrometer and the deposition chamber.

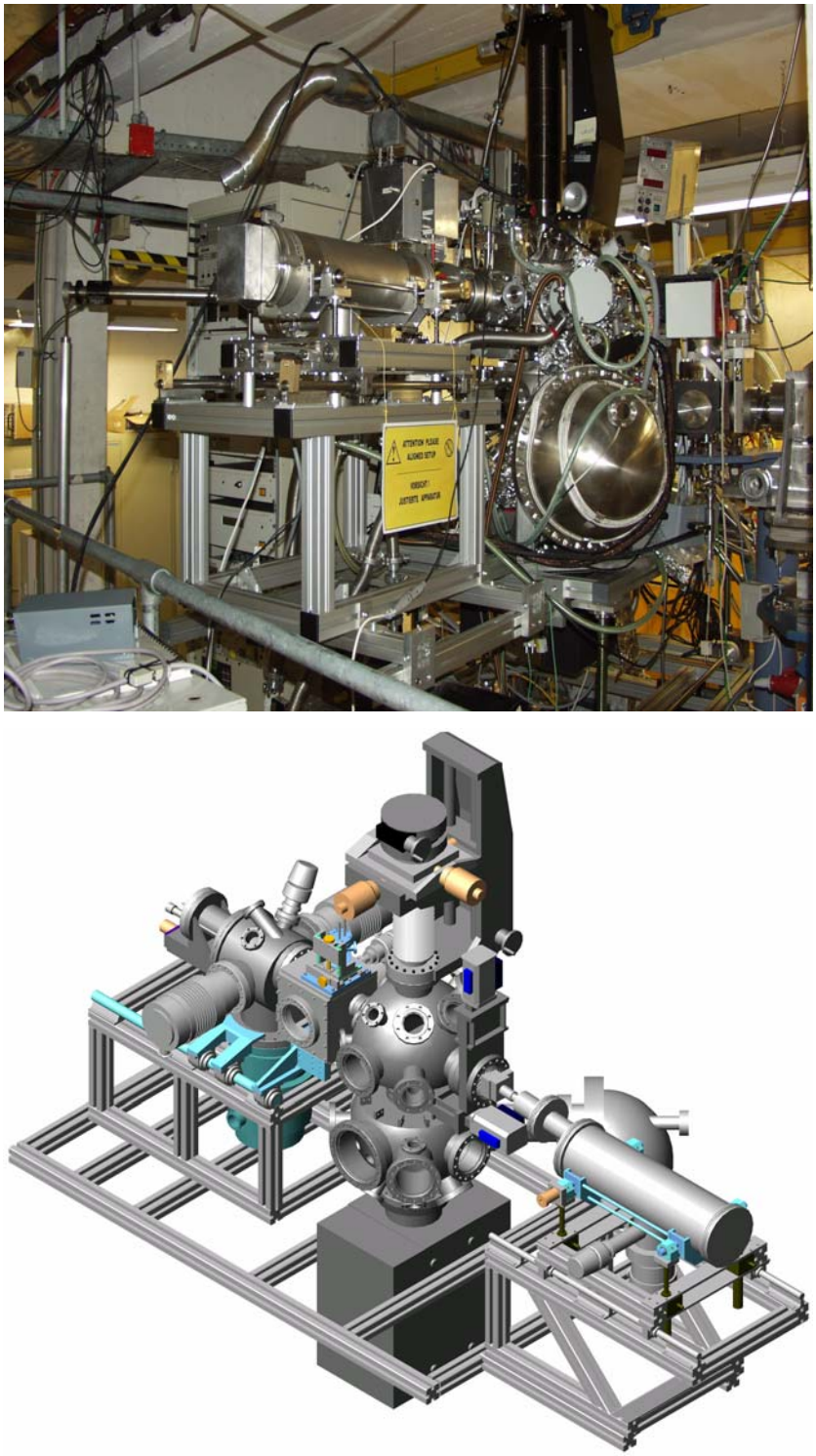

Figure 2.1 The picture of the setup installed at the BW3 platform (top). b) 3D view of the apparatus, the main parts are visible (bottom). The pre-chamber and the transfer system are left out for clarity. From [22]

The bake out procedure is not required in case of cluster and oven chamber due to the relatively high working pressure (10^{-3}-10^{-4} mbar) during cluster production. Another valve is placed between the oven chamber and the pre-chamber making possible to vent separately the cluster and oven chamber and refill, for example, the crucible.

Figure 2.1 shows the experimental setup mounted on the BW3 beamline platform (top picture) and a 3 dimensional drawing (bottom). The pre-chamber and transfer system are detailed in the **figure 2.3**.

The cluster source chamber has a cylindrical like shape and accommodates the cluster source. There are two DN 38 CF flanges where a window flange and a compact full range gauge (*balzers Instruments*) [14] are installed. The bottom DN 150 CF flange is connected to a large Balzer-Pfeiffer turbo pump (TMU 1000 - 880l/s pumping power) [15].

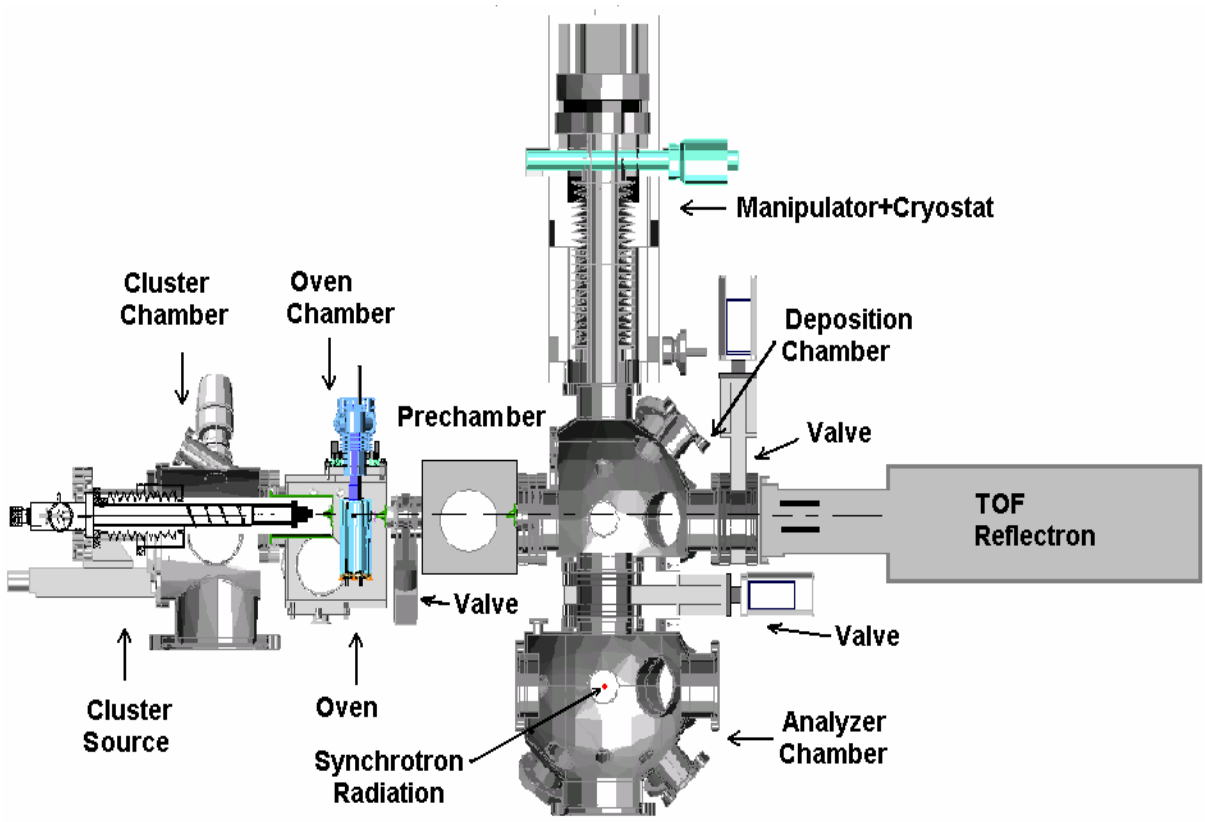

Figure 2.2. Side view of the experimental station. The primary cluster beam delivered by the cluster source (left) has to pass several skimmers and is detected with the help of the TOF mass spectrometer. The spectroscopic investigation of the deposited samples take place in the analyzer chamber. A very good alignment for the cluster experiment is crucial. Modified from [22]

Two *Wide range* turbo pumps (TPU 180H - 180 l/s) attached to the DN 100 CF flanges together with oil free *Varian Triscroll* vacuum pump (25.2 m^3/h) are used [16]. The cluster source is connected with a large KF flange. For a compact and flexible design the cluster source penetrates (enters) the space corresponding to the oven chamber. A small cylinder is attached by screws and together with a 1mm skimmer delimitate the "real" volume of the cluster chamber and create a differential pumping stage.
The pressure with the gas admission valve off is in the 10^{-7} mbar range and during cluster production raises up to 10^{-3}-10^{-2} mbar.
The oven chamber has a cube like shape with rectangular flanges on the top and bottom faces. The oven is attached to the top flange and the bottom flange is blind. Two Balzer-Pfeiffer *Wide range* turbo pumps are fixed on the DN 100 CF side flanges and the fore-pump is a *Varian Scroll* vacuum pump (12.6 m^3/h). On the left side (from the direction of the cluster beam) there are three DN 16CF flanges that are equipped with a full range gauge (*balzers Instruments*), a beam shutter and an optional gas line where with the help of a small capillary one can dope the primary rare gas clusters [97].
A second 2mm skimmer is placed on the internal wall of the exit flange.
The pressure when no gas is let inside is typically 10^{-8}-10^{-7} mbar and in case of Cu cluster experiment (Ar clusters, oven on) the working pressure has values in the 10^{-4}-10^{-3} mbar regime.

Future plans include a second oven that can be installed on the bottom rectangular flange of the oven chamber and will allow the co-doping of the primarily cluster beam or production of core-shell structures. The modifications of the existing construction (oven and cluster source chamber) are minimal: the cluster source nozzle has to be retracted about 100-120 mm (it can be done easily) and the small cylinder that sustains (supports) the skimmer may be replaced with a shorter one. A second oven can be fixed on the rectangular bottom flange, just few mm distance from the existing oven.

The pre-chamber having a cube like shape is separated by a UHV *VAT* DN 40 CF valve [17] from the oven chamber. A 210 l/s turbo pump (Balzer-Pfeiffer) and a cold cathode gauge are attached on the side DN 100CF flanges. The main purpose of adding this extra chamber was to reduce the Ar/Cu ratio for the deposited samples. The negative aspect is the reduced in intensity of the cluster beam and consequently lower signal of the Reflectron TOF. Future plans consider the idea of mass selection for the cluster beam and such device may be connected (installed) in the pre-chamber. A third skimmer with 5 mm diameter is placed on the internal wall of the exit flange. With the valve closed the pressure is in the 10^{-10} mbar range and raises up to 10^{-7} mbar during the cluster experiment (valve open).
The cluster source, oven and pre-chamber (made from stainless steel) were machined in the DESY workshop.

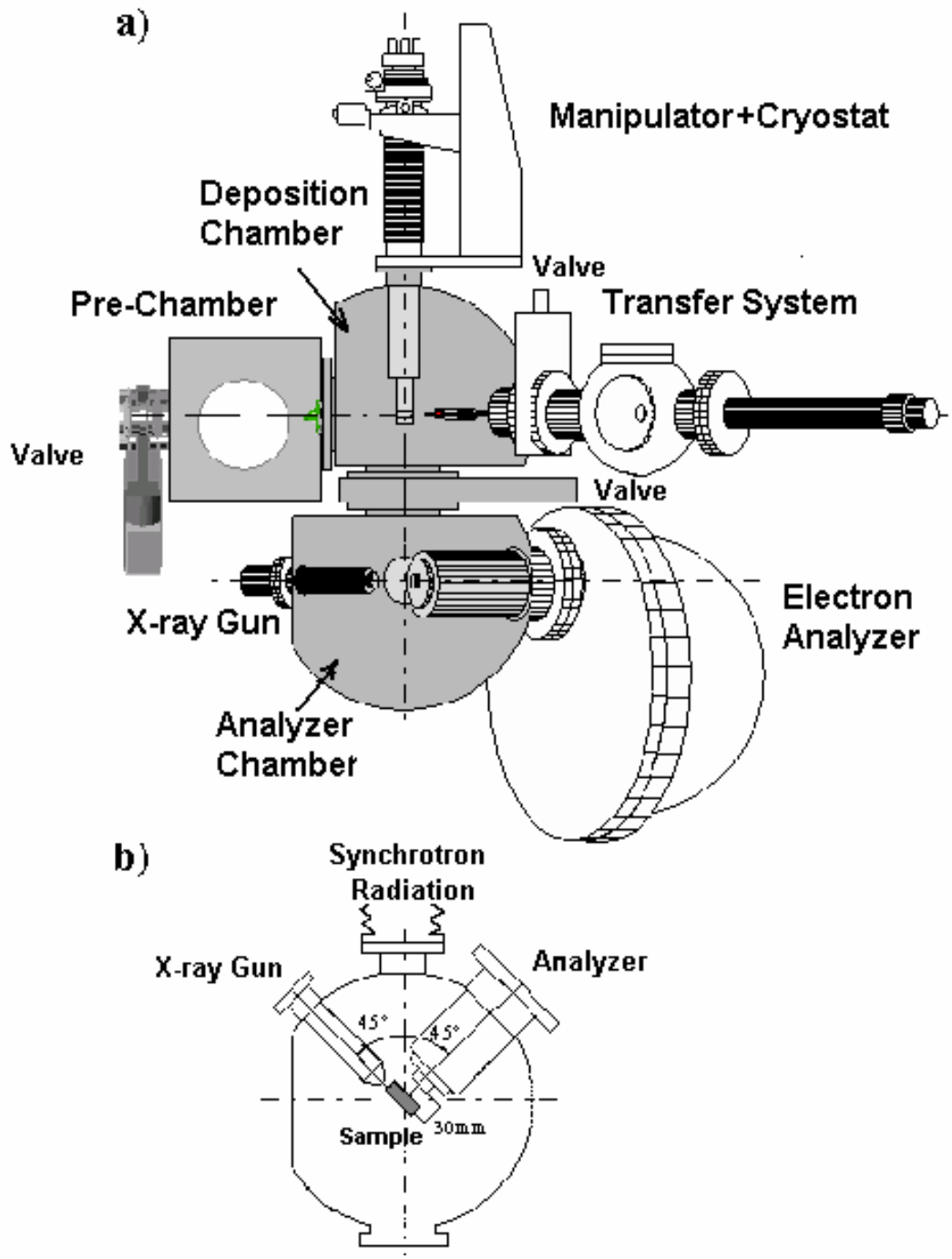

Figure 2.3. Schematic representation of the UHV (bakeable) part of the experimental setup:

a) Side view

b) Top view of the analyzer chamber

The pre-chamber and the transfer system are visible here - see a). The sample position during the investigation with synchrotron radiation is sketched in figure b). The valve between deposition and analyzer chamber is kept closed during cluster deposition. From [18].

The exit DN 100 CF flange of the pre-chamber is connected to the deposition chamber (**figure 2.3 a**). The hemispherical shape chamber has 19 flanges with different sizes and the idea behind the original design is detailed depicted in [18]. In case of the present experiment 12 of them were blind or window flanges.

The preparation chamber supports the cryostat and the *xyz* manipulator that are connected on the top DN 100 CF flange. The transfer system that is also visible in **figure 2.3 a)** is connected at one of the side DN 63 CF flange. Additional devices like sputter gun, cleaving jaws, compact full range gauge (*balzers Instruments* [14]) and one oil free *TPU 180HM* (170 l/s) turbo pump form *Pfeifer Vacuum* [15] are attached on the side flanges (not shown). Both deposition and pre-chamber turbo pumps are connected to a XDS 10 scroll pump (11m^3/h) from *BOC EDWARDS* [19]. A DN 100CF *VAT* vacuum valve separates the deposition chamber from the *TOF* mass spectrometer. A skimmer wall (10mm diameter) is used as gasket between the *VAT* valve and the *Reflectron TOF* creating a differential pumping stage.

The pressure is in the 10^{-7}-10^{-8} mbar range when the cluster beam passes through the chamber or deposition takes place and 10^{-9} mbar are measured with a *balzers* full range gauge when the valve between oven and pre-chamber is closed.

The analyzer chamber is built on top of a *Varian StarCell 500* [16] ion pump (410 l/s). There are all together 20 different sizes CF flanges but majority of them (15) are blind or window flanges. The x-ray gun, the electron analyzer and the connection to the BW3 beamline are sketched in figure 3b). A *VAT* DN 100 CF vacuum valve separates the analyzer chamber from the deposition chamber. This valve is kept open except when the cluster beam enters the deposition chamber or the sputter gun is in used. Only then, the valve has to be closed in order to preserve UHV conditions (10^{-9} mbar) in the analyzer chamber. The pressure in the analyzer chamber is monitored during experiment by a *balzers* cold cathode gauge or the ion pump.

Both deposition and analyzer chamber were manufactured by *Vacuum Generators* [20]. The deposition chamber was made of stainless steel but the analyzer chamber had to be made of Mu metal for an efficient magnetic screening required in case of high resolution measurements with the Omicron electron analyzer.

The setup is supported by an aluminum frame and four wheels provide good mobility on smooth surfaces. During the experiments the frame rests on four legs. The height of the setup is further adjusted with help of an electro-motor (up to extra 310mm). This makes the setup flexible and compatible with other beamlines or synchrotron facilities.

Since there are no valve between the turbo pumps and the corresponding chambers, the setup has to be always nitrogen vented before moving to the synchrotron beamline. The experimental apparatus is placed on the BW3 platform with help of a fork lift of the DESY Transport Group.

2.2 DEVICES

2.2.1 The cluster source

The main purpose of the cluster source is to produce of the primary Ar cluster beam. The adiabatic gas expansion through the cold nozzle results in efficient condensation of the rare gas since the temperature drops rapidly and produces Ar clusters. For detail information about the cluster production and the theory behind the process see chapter 5.

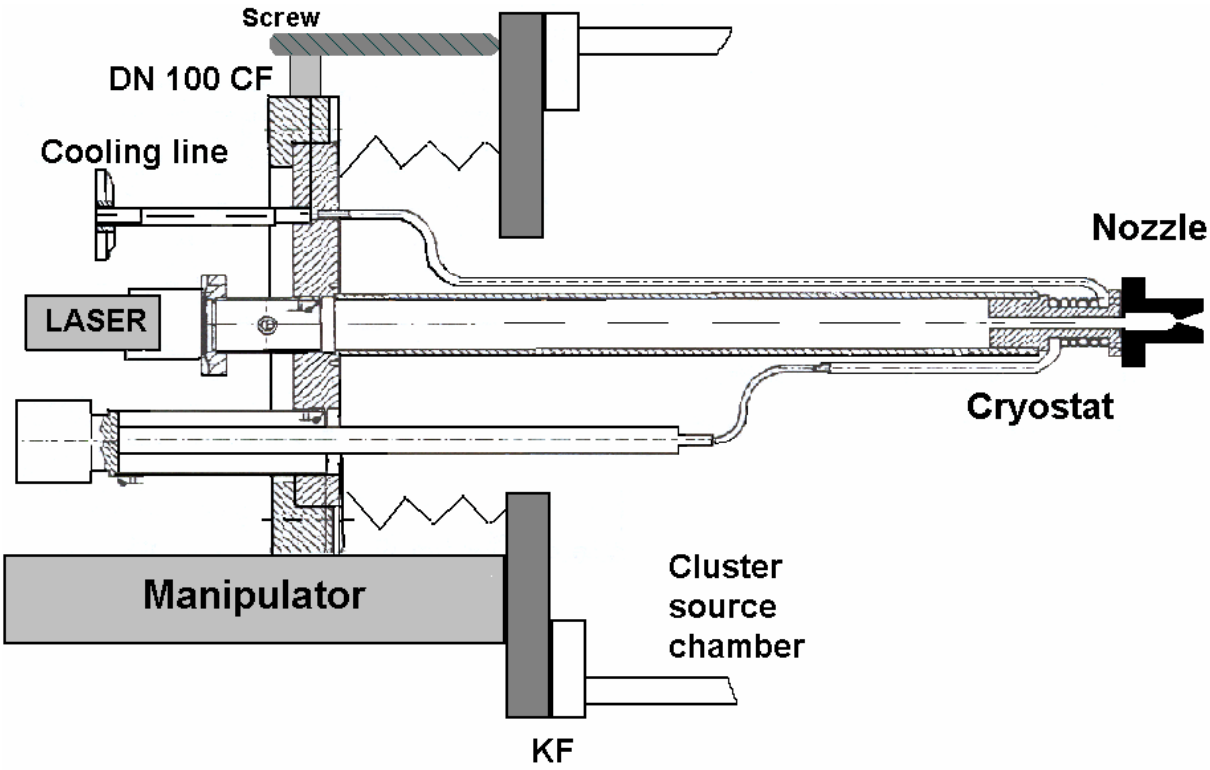

Figure 2.4. Schematic representation of the cluster source. The heating element and the temperature sensor, both connected to the outer surface of the cryostat are not visible here. Modified from [18]

The main components of the device are depicted in **figure 2.4**. A stainless steel tube (20×2×395 mm) is connected on the center axle of a DN 100 CF flange. The tube is closed with a DN 16 CF window

flange. A commercial semiconductor red light laser is installed in front of the small window flange making easier the alignment of the cluster experiment. A 40 mm long copper tube with 4 mm internal diameter ends the vacuum part of the stainless steel tube. The copper block (cryostat) is cooled with help of liquid nitrogen and the copper nozzle connected with screws to this cryostat is sealed with In gaskets in order to obtain high thermal conductivity. Since the nozzle geometry influences the cluster production (see chapter 5), the optimum choice for each particular experiment has to be made. In the present case a conical shape nozzle with diameter $d_{nozzle}=300\ \mu m$ and half opening angle of 8^o is used.
The cryostat copper block may be heated up by a $50\ \Omega$ resistor. The nozzle temperature T_0 is measured with help of a *LakeShore* Si-diode; the control of the heating element and the temperature reading is supported by a *Lake Shore 300* cryo-controller [21].
The lowest temperature (for the nozzle) that can be reach with help of liquid nitrogen cooling is 77K.
The previous described device is mounted on a *xyz*-manipulator that makes the alignment of the cluster source possible (not shown here). The typical distance between nozzle and first skimmer is 7-8 mm. The connection to the cluster source chamber is done with help of a KF flange.
The cryostat is pumped with help of a membrane pump; the liquid nitrogen continuous flow is regulated in a way that the gas pressure at the end of the exhausting line is about *300 mbar* any time during the cluster production and under those conditions a 100 l dewar supplies sufficient cooling agent for up to 2 weeks experiments.

2.2.2 The oven

The capture of atoms or molecules by a primarily rare gas cluster beam, the so-called pick up technique has recently rapidly gained popularity. Typically, a beam of rare gas clusters produced by adiabatic expansion in a supersonic jet is passed through a region that contains vapor of the substance of interest and under specific conditions the picked up atoms are stored by the primarily clusters. For more information about the process see chapter 5.
The doping material (for the present investigation-Cu) used for the pick up process is evaporated with help of an electrical heated oven (**figure 2.5**). High priority in the design has been the minimization and the convenient manipulation of the device.
The crucible made of boron-nitride can be easily refilled or replaced. The entrance and exit holes with 5 mm diameter are placed on the direction of the cluster beam. The crucible is covered with a hat made also from boron-nitride that prevents the evaporating material for contaminating the whole oven.

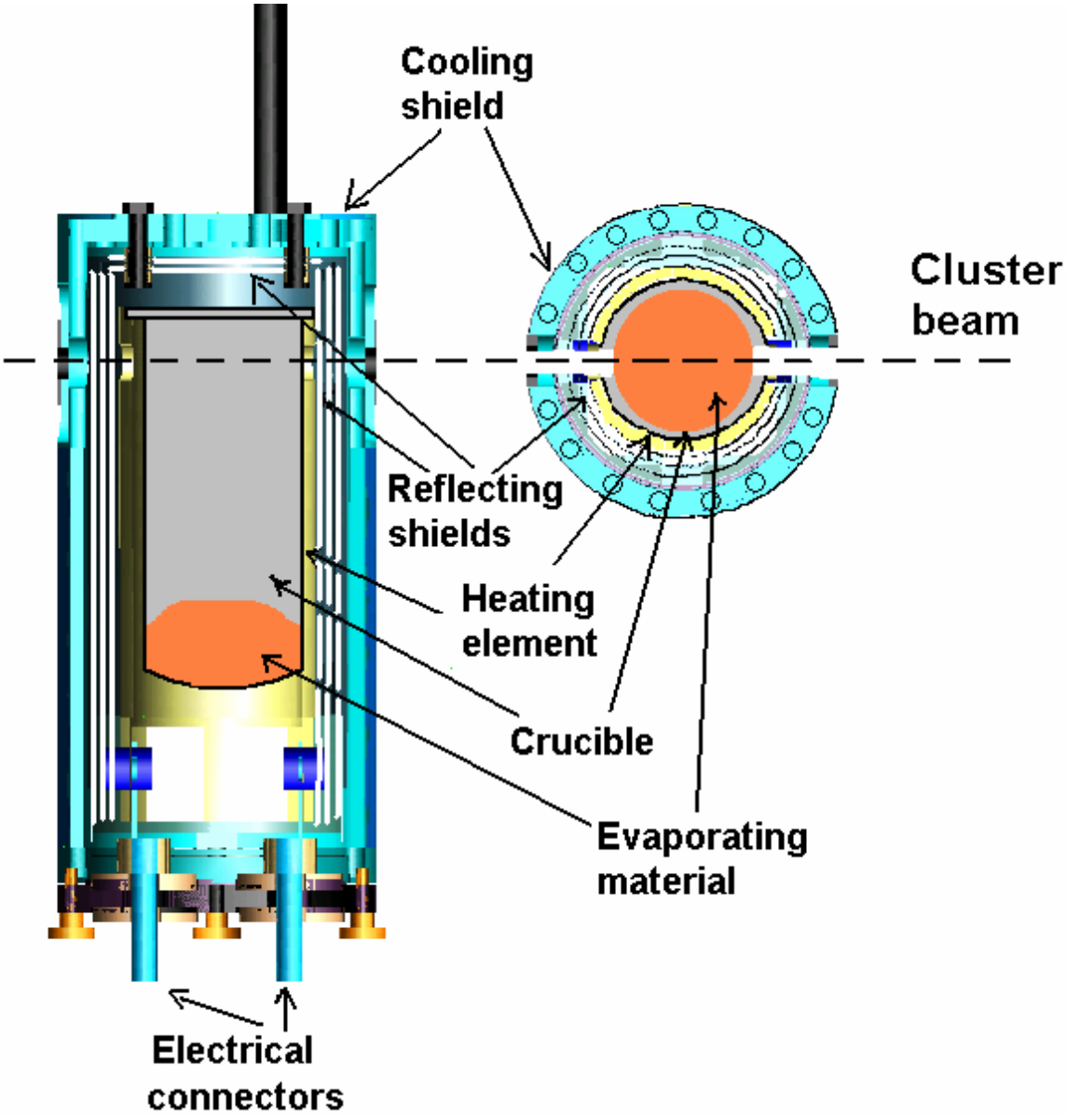

Figure 2.5. The key elements of the oven, side (left) and top (right) view. Modified from [22]

The heating element from *Advance Ceramics Corporation* [23] has a tube like shape and is made of boron-nitride; the graphite heating wires are integrated in the tube walls. The electrical connectors (see bottom of the left image, figure 5) consist of niobium wires that are suitable for high temperature conditions during the experiments.

Temperatures higher than 1200ºC, required for an efficient pick up process (see chapter 4), are measured with a *type C* thermocouple [23]. The sensor is mounted on the inner wall of the heating element and it is capable of accurate temperature readings in the 0 - 2300°C range. A HC3500 heater controller from *tectra* [24] was used.

Niobium shields placed around the heating element significantly reduce the heating lost through radiation and together with the cooling shield (water cooled) keep the temperature low at the oven outer surface. For example, the Pt100 sensor measures outer surface temperatures of 22ºC and 25ºC (!) when the internal (crucible) temperatures are 22ºC and 1310ºC (!), respectively.
The outer surface temperature has to be monitored any time the oven is switched on; if the PT100 sensor displays significant increase in temperature, the oven should be immediately switched off in order to prevent the overheating of the oven in case of malfunction of the cooling system.
The amount of material evaporated during several months of experimental work was very low, less than 15% of the original 2 cm^3 high purity Cu.

2.2.3 Manipulator + cryostat; TEY detection

One of the essential requirements for doing low temperature investigations is good thermal contact between the sample and the cryostat. Usually, this is achieved by either immersing the sample in cryogenic refrigerant or using a contact gas. In both cases the sample is enclosed by walls at low temperature, almost completely eliminating radiative heat-input into the sample. However, in-situ sample deposition and photoemission techniques call for a sample with at least one face open to the ultra high vacuum, thereby excluding the immersion in liquid or use of a contact gas. This means that the only way of cooling the samples is by direct solid to solid contact. In the present case, the need of new sample holder for each particular sample deposition makes difficult to employ effective radiation shielding.
A UHV compatible *Konti* cryostat from *Cryovac* [25] is installed on a DN 63 CF flange (**figure 2.6**). The device may be cooled with liquid He or may be heated by a 50 W heating element covering a wide temperature regime from 10 to 700K. The liquid He-transfer tube that continuously supplied the cryostat is centered on the top of the device and is fully rotate-able (360º). The exhaust line for the He gas is pumped with help of a He sealed pre-pump ($10m^3$/h) supplied by Cryovac. The liquid helium flow is regulating by leak valves.
A sapphire (Al_2O_3) disk is connected between the heat exchanger and the Cu "cold finger"-see **figure 2.6**. Sapphire is a good thermal conductor and in the same time a very good insulator, this means that the "cold finger" is electrically isolated from the experimental chamber. It is very hard material, so the risk of breakage is reduced.

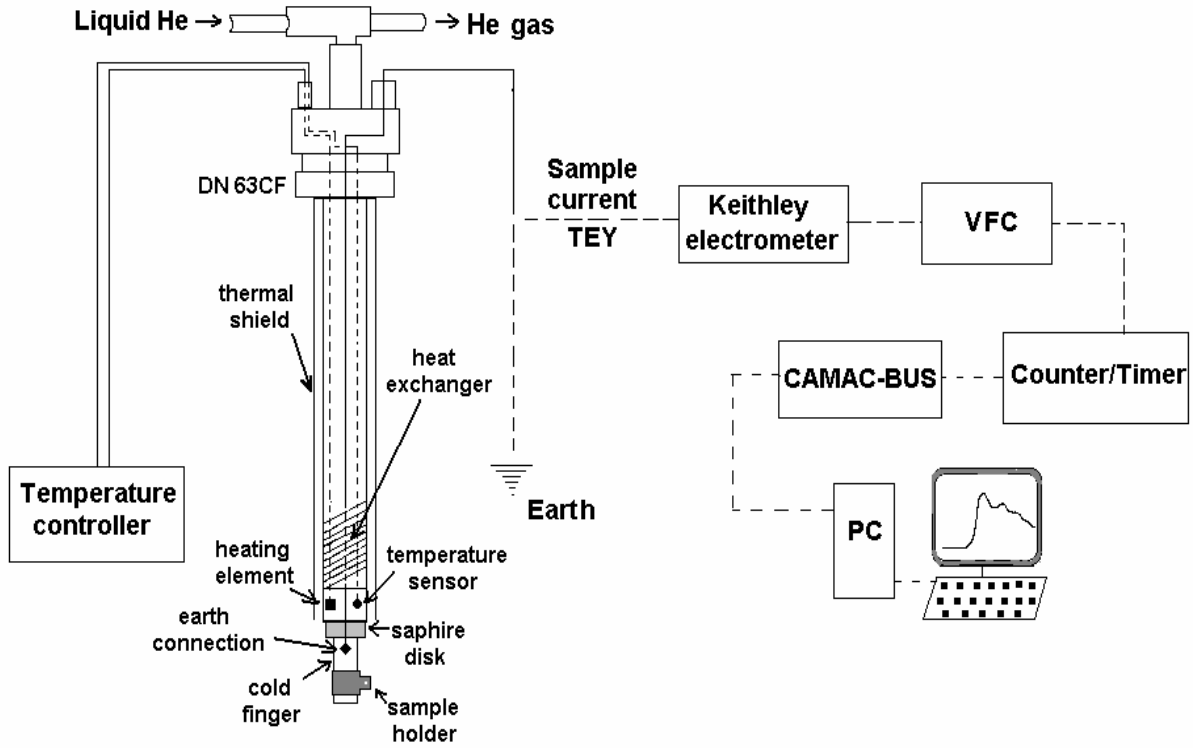

Figure 2.6. The main elements of the Konti cryostat together with the detection chain for the sample current measurements (TEY) are sketched here.

The sample holder is attached to the "cold finger" with help of springs. An electrical connection is attached to the cold finger with help of a shielded cable, preventing the sample from charging during experiments.

Since the sample holder is several tens of mm distance from the temperature sensor position one would expect a few Kelvin difference between the temperature readings of the *LTC 11 temperature controller* [26] and the real temperature of the sample (holder.) The heating element is activated by the same *LTC 11 controller*.

The cold finger made of copper was supplied by *Omicron* [27] and the sample holder(s) consisting of simple rectangular blocks of OFHC (oxygen-free high conductivity) copper (for cold Cu clusters deposition) or stainless steel (for InP samples) are machined in the *Hasylab workshop*.

The cryostat is mounted on a differentially pump rotary platform that allows 360º rotation. A triple axis *xyz* manipulator from Caburn MDC [28] allows travel of the cryostat (sample holder) on *x* (±25 mm), *y* (±2.5 mm) and *z* (0 to 310 mm) directions; it provides very precise motion (*xy* motions are micrometers driven) and manipulation of the sample inside ultra-high vacuum environments.

Both cryostat and manipulator are bakeable up to 230ºC.

TEY

The sample current ***T**otal **E**lectron **Y**ield* (***TEY***) is recorded with help of the detection chain depicted in **figure 2.6**. Briefly, the shielded cable (isolated wire) coming from the "cold finger" is now connected to the Keithley electrometer [29]. A ***V**oltage to **F**requency **C**onverter* (***VFC***) transfers the signal to the *Counter/Timer* than to the *CAMAC BUS*. Finally the signal is displayed on the beamline *PC* monitor.

2.2.4 Electron analyzer

The kinetic energy of the photoelectrons is measured by an EA 125 U 7/7 125 mm hemispherical electron analyzer [30] supplied by Omicron Nanotechnology [27]. The principle of operation is sketched in **figure 2.7**. The photoelectrons coming from the sample are focused by an electrostatic lens system onto the entrance slit. After the slit they enter a space defined by two concentric hemispheres, between which a potential difference is applied. The electrons are deflected more or less parallel to the hemispherical surfaces, depending on their kinetic energy: electrons with the desired energy (the so called pass-energy E_{pass}, determined by the potential difference between the hemisphere and their radii) follow trajectories that refocus them on the exit slit, where they are detected by the channeltron detectors (7 channels). The electrons with too high or too low energy miss the exit slit. A complete spectrum could be obtained by scanning the pass energy E_{pass} – the so called ***F**ixed **R**etarding **R**atio (**FRR**)*, but this has the disadvantage that the resolution (which is proportional with the pass energy) becomes energy-dependent. Instead, usually the pass energy is kept constant and the variable *retardation* potential slows down the electrons in the lens system before they enter the hemispheres - ***F**ixed **A**nalyzer **T**ransmission (**FAT**)*.

The EIS software that controls the electron analyzer has a Windows standard remote control interface, which can be used to perform custom experiments. It can be accessed from any Windows programming environment which supports COM / OLE Remote Control such as Visual Basic, Visual C++ and Visual Basic for Applications.

In our case a Visual Basic interface allows us to performed ***C**onstant **F**inal **S**tate* (***CFS***) experiments. ***CFS*** mode means that the excitation source energy is scanning and the analysis energy remains constant. In other words only electrons having a fixed kinetic energy are detected (present case - Cu Auger LVV) while the excitation energy is scanned (around the Cu $L_{3,2}$ edges).

The results are Auger yield spectra, which correspond to some extent to absorption spectra; for more information see chapter 3.

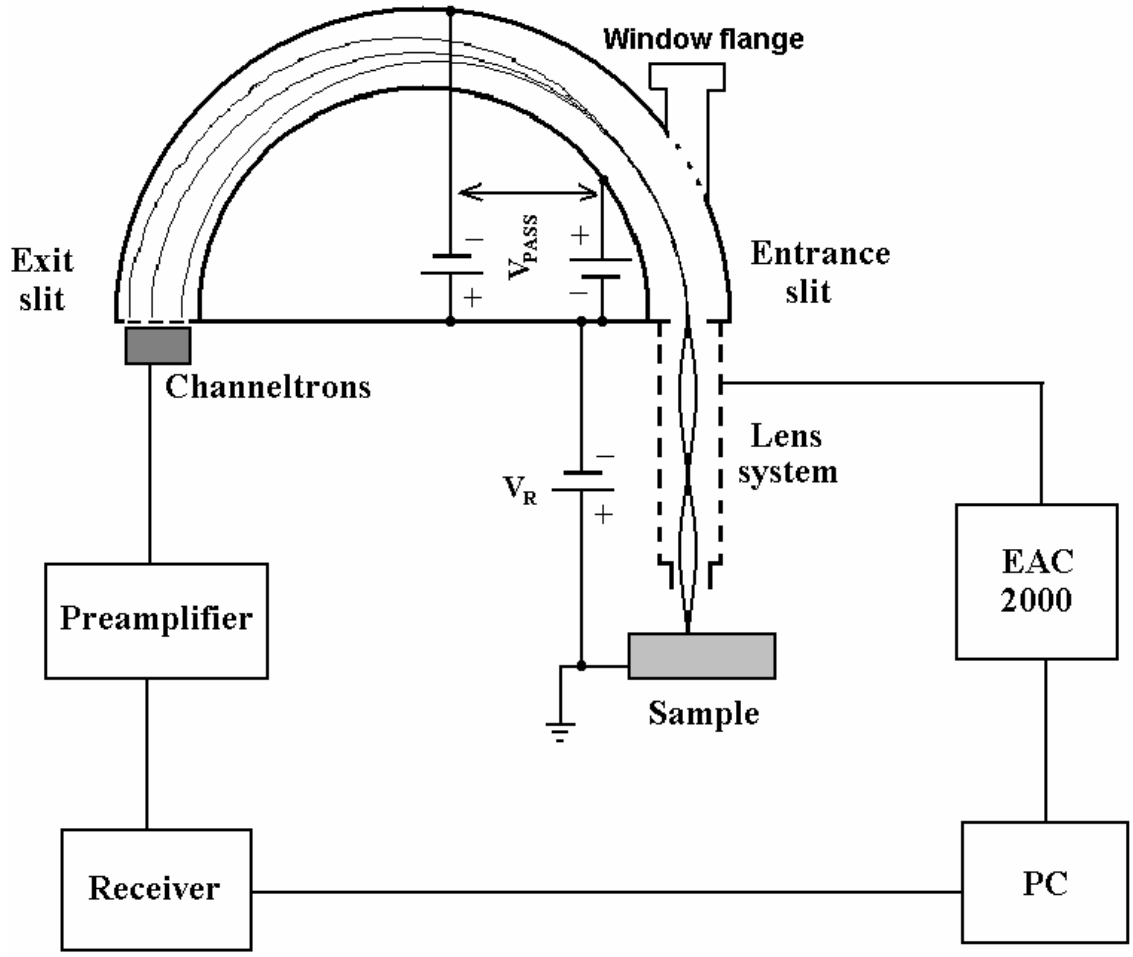

Figure 2.7. Schematic diagram of a hemispherical electron analyzer, giving an impression of the electrons paths. The detection chain is also sketched here. The sample can be visualized through the small window flange of the analyzer.

The lens system is also design to define the analysis area and angular acceptance of electrons, which pass through the hemispherical analyzer: magnification mode *high*, *medium* and *low* with the corresponding acceptance angle - *8º*, *4º* and *1º* respectively. The analysis areas (diameter) for a 6mm Ø entrance aperture are 6mm (magnification low), 3 mm (medium) and <1.5 mm (for magnification high).

Variable slits are located at the entrance and exit of the analyzer. These are selected manually by means of external rotary feedthroughs.

Seven channel electron multipliers (Channeltrons) are place across the exit slit of the analyzer and the signal is amplified by a factor of 10^8. The small current pulse at the output of the Channeltron is passed through a vacuum feedthrough and then directly into the preamplifier. The electrical signal is converted into an optical signal and passed with the help of optical fiber on to a receiver. The pulses are counted and processed and the electron energy spectrum is displayed on the computer monitor.

2.2.5 Sputter Ion Gun

Our sputter gun was supply by the Omicron Nanotechnology [27]. The ISE 5 ion gun [31] was occasionally used during the experimental work and only for cleaning substrates.
Briefly, the argon gas is fed into the gas cell. With the help of a longitudinal magnetic field Ar ions are generated between the anode and cathode.
The ions are extracted from the gas cell through an aperture in the cathode plate and into a flight tube. A focus element located inside the flight tube enables the ion beam to be focused onto the sample.
The safe operation of the device requires a base pressure below 1×10^{-7} mbar inside the experimental chamber (deposition chamber) before running the ion gun. During the sputtering procedure the Ar leak valve is slowly opened and the pressure should never exceed more than 2×10^{-4} mbar as this may drive the gun into a self-destruction discharge condition.

2.2.6 X-ray source

The DAR 400 is an X ray source [32] provide by the Omicron Nanotechnology [27]. The source is equipped with a twin anode that allows either Mg K_α or Al K_α radiation to be selected.
The electrons are extracted from a heated filament to bombard the selected surface of an anode (Mg or Al target) at high positive potential. The water-cooling prevents the anode from getting too hot and protects against target evaporation. The X rays generated in the surface of the anode pass through a thin aluminum window that acts as a partial vacuum barrier between the source and the sample region. The pressure in the experimental chamber should be less than 2×10^{-8} mbar when the source is switched on.
The DAR 400 gun is installed on a manipulator that makes possible to vary the distance to the sample (recommended distance $d\leq 10$mm).

The X ray source was used only for routine analysis during periods with no access at synchrotron radiation.

2.2.7 Transfer system

The transfer (load lock) system is sketched in **figure 2.3 a)**. It was supplied by the *Caburn MDC* [28] and allows convenient and practical ways for transferring samples in and out of the vacuum system. The load lock system includes a magnetic sample transporter, a gate valve and a small spherical staging chamber equipped with quick access door and observation view port. The transfer system (gate valve) is attached on a side DN 64CF flange of the deposition chamber. During experiment the gate valve is kept closed. The sample holder is changed in air and for that only the transfer system has to be vented. After replacing the sample holder, the load lock system is pump down by a turbo pump (*Pfeifer Vacuum TPU 180HM*). There is no need bake out, pressures in the 10^{-9}-10^{-8} mbar range can be achieved in less then one hour pumping. Then, the gate valve is opened and the new sample holder is driven into deposition chamber with help of the magnetic sample transporter and attached to the cold finger.

2.2.8 The Reflectron TOF

The cluster mass spectra are recorded with the help of a ***Reflectron Time of Flight*** spectrometer [33]. Time-of-flight (TOF) spectrometers combine a relatively simple mechanical setup with fast electronic data acquisition. The typical mass resolution is $\Delta m/m \approx 2000$ and the maximum detection range is 25000 amu (atomic mass units).

The clusters are ionized by the electron gun with an impact energy that can be tuned in the 4-250 eV range.

TOF mass spectrometry is based on the fact that for a fixed kinetic energy E the mass m and the velocity v of the ions are correlated:

$$m = 2E / v^2 \qquad (2.1)$$

By measuring the time t the ions need for traveling a fixed distance s the velocity v and from equation (2.1) the mass m of the ions can be calculated.

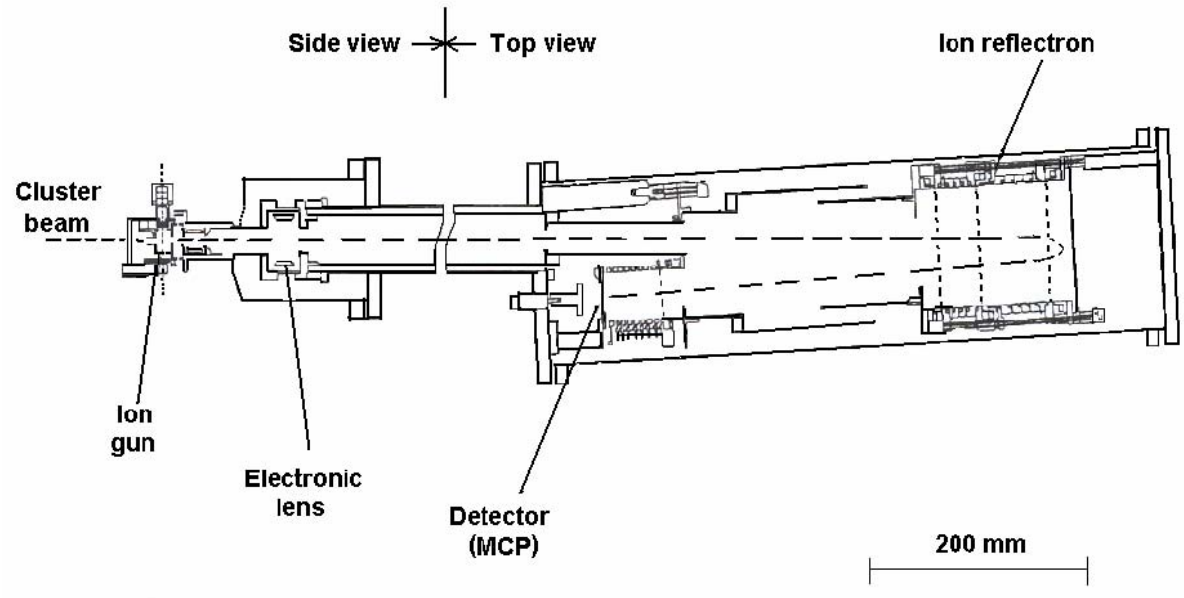

Figure 2.8. Schematic diagram of the Reflectron Time of Flight mass spectrometer. The path of the cluster beam is shown as dash line. From [33]

Spatial focusing is required since the length *s* of the flight path in the spectrometer is not identical for all the ions due to ion creation that takes place in a finite volume. By using an appropriate potential distribution of the ion extraction field ("Wiley-McLaren-criterium") [34] it can be achieved that the ions which have to travel a longer distance have larger kinetic energies, i.e. all the ions arrive at the same time at the detector independent of their starting positions.

The different starting energies of the ions (caused by space charge effects, fragmentation, desorption) may reduce the resolution. This effect can be compensated by passing the ions through an ion reflector ("Reflectron TOF spectrometer"). Faster ions penetrate deeper into the repelling electric field of the ion reflector i.e. they have to travel a larger distance. All the ions arrive at the same time at the detector, independent of their starting energy ("energy focussing") [35, 36].

Both focusing methods have in common that the increase in resolution doesn't lead to smaller signal amplitude.

The signal is detected with the help of multichannel plate (mcp) detectors. The Reflectron TOF spectrometer voltages are manually selected. The electron gun parameters and data acquisition are controlled by the TOF computer.

The pressure during measurements should not exceed more than 1×10^{-6} mbar.

Fine tuning-up/down, left/right of the Reflectron makes the alignment of the cluster experiment possible.

2.3 Synchrotron radiation - the BW3 beamline

High energy electrons forced to adopt a bent trajectory emit electromagnetic waves called synchrotron radiation. The characteristic of the emitter radiation naturally depend on the electron beam which is circulating under UHV condition (10^{-10}-10^{-9} mbar) in the so called "storage ring".
Synchrotron radiation is the only available continuous light source that can cover the spectral range from vacuum ultraviolet to hard x-rays. One of the most important characteristics of the synchrotron radiation is its high brilliance - useful for studying low dimensional or dilute samples. For a given energy the brilliance is defined by the number of photons per second per mm^2 (source area) per mrad (opening angle) and for an energy bandwidth equal to 0.1% of the energy under consideration.
In case of modern synchrotron facilities there are two types of insertion devices: wigglers and undulators. Each comprises a succession of small magnets of alternating polarity. The resulting magnetic fields force the electrons to oscillate around linear trajectories. The light cones emitted at each bend superimpose and in case of wigglers their intensity increases proportionally. The deviations in the undulators are weaker, thus the light cones from different bends overlap and through the phenomenon of interference the resulting spectrum has a brilliance up to 10^4 higher than that produced by simple bending magnets. The wavelength maximum of the emitted radiation can be shifted by varying the the undulator gap.
More information about the synchrotron radiation and insertion devices can be found in [37].
The present experiments were performed at the BW3 beamline on the DORIS III storage ring at HASYLAB / DESY in Hamburg, Germany. The positrons in the storage ring have 4.5 GeV kinetic energy and an average beam current of 120 mA. Two interchangeable undulators cover the 15-1800 eV spectral range. The first optical element of the beamline is a water cooled mirror follow by a modified Zeiss SX-700 plane grating monochromator. It consists of a premirror, a plane grating and a spherical focusing mirror which focuses the light onto the exit slit that can be manually adjusted. The monochromatized light from the exit slit is refocused by a toroidal mirror into a spot of 100 (vertical) × 200 (horizontal) μm. Typical flux at sample is ~10^{12} photons/s in 0.1% bandwidth at 500 eV for 100 mA electron ring current. The energy resolution at 500 eV with the 80μm exit slit is ~186 meV; for the formula giving the monochromator resolution see (3.3).

Data acquisition and running of the beamline is performed with a μ-Vax computer through a CAMAC controlled.
For more detailed information about BW3 beamline see [38, 39].

2.4 Alignment of the setup

A very good alignment is crucial for acquisition of high quality data. An overview of the cluster experiment is shown in **figure 2.2** and that of the analyzer chamber in **figure 2.3 b**).

2.4.1 Alignment for the cluster experiment

The alignment for the cluster experiment is done typically before the beamtime for the following two main reasons:
- first, one needs time to find the best parameters (pressure and temperature) for the cluster production
- second, the alignment of the cluster experiment requires 1-2 days and this amount of time can be saved for experiments with synchrotron radiation.

The cluster experiment adjustment results in the following way: the whole setup has to be vented and all valves are open (see **figure 2.2**). The Reflectron TOF is disconnected and a window is placed on the corresponding KF flange. The oven and all skimmers are removed. The red laser connected on the back of the cluster source (see **figure 2.4**) is switched on and cluster source is gentle moved is such a way that the light spot exit the KF window flange exactly in the center (middle).
Once the laser spot is on the right position the setup is pumped down. Since the cluster source is connected with a bellow to the KF flange, it happens often that the alignment is lost once the pressure drops in cluster source chamber. To overcome this problem one has to tighten the top screw (see **figure 2.4**) firmly against the wall.
The setup is once again vented and the first skimmer is installed. If the laser spot is on the right place, the valve in front of the reflectron flange can be closed; the window flange used for alignment is removed and the Reflectron TOF is reconnected.
A beam of Ar clusters is produced and the Reflectron position is adjusted to give the higher intensity for the measured clusters. Finally the other 2 skimmers and the oven are placed in position and the setup is ready for producing Ar or Cu clusters.
The alignment of the cluster experiment is preserved when the setup is vented and installed at the BW3 beamline platform.

2.4.2 Alignment for the analyzer chamber

The setup is vented and connected with a bellow to the synchrotron line (see **figure 2.3 b**). The beamline is set to provide "*zero order light"* (visible white light). The light should enter the

synchrotron flange and exit the opposite window flange exactly in the center. The radiation focusing point has to be on the sample holder for manipulator coordinates *x=0 mm*, *y=0 mm* and *z= 39 mm*. The alignment of the setup with respect to the beamline is facilitated by a compressed air device that allows smooth horizontal movements. The height of the setup is easily tuned with help of an electromotor.

If the alignment is right, the focusing point on the sample holder is clearly visible from the analyzer window flange (see **figure 2.7**). Then, the setup can be pump down and bake out.

Fine tuning of the sample holder position (*xyz*) has to be done before each measurement.

Chapter 3. Investigation techniques

3.1 Photoelectron spectroscopy

Photoemission spectroscopy (PES) is a technique to probe occupied electronic states.
The spectral domain lower than 40 eV corresponding to ultraviolet (UV) radiation is mainly used to study the valence band structure and the investigation method is known as Ultraviolet Photoelectron Spectroscopy (UPS).
Soft X-ray Photoelectron Spectroscopy (XPS) corresponding to radiation up to 1500 eV is more effective for the investigation of the core level states. This technique is also especially useful because the local electronic structure can be probed. The discovery during the early days of XPS that non-equivalent atoms of the same chemical element have slightly different binding energies had a stimulating effect on the whole field; much of the early work and the basic ideas are discussed by Siegbahn et al. [40]. The photoemission peaks are shifted with respect to the main line of to the "pure" element. These shifts are also referred to as ***chemical shifts*** and the technique as ***ESCA*** *(**E**lectron **S**pectroscopy for **C**hemical **A**nalysis)*. The non-equivalence of atoms can rise in several ways: different chemical bonding, oxidation state, bond length, angle variation, etc. [42].
A particular case of ***chemical shifts*** are the ***surface core-level shifts (SCS)***. They originate from a different coordination, i.e., bonding, of the surface atoms. The shifts are rather small (0.1-0.3 eV) and only limited number was experimentally proved in the last 10-15 years.
In 1887 Herz observed that a spark between two electrodes occurs with higher probability if the negative electrode is illuminated by UV radiation. The correct interpretation of this effect was given by Einstein [41]. He postulated that light was composed of discrete quanta of energy E_ν, this energy being proportional to ν, the frequency of the light: $E_\nu = h\nu$.
The kinetic energy of the escaping photoelectron is given by the following equation:

$$E_{kin} = h\nu - E_B - W_s \qquad (3.1)$$

where $h\nu$ is the energy of the excitation photon

E_b is the binding energy of the electron inside the atom

W_s is the work function of the sample

The photoemission effect is sketched in **figure 3.1**. The binding energy E_B of the initial state is defined as the energy difference between the initial state and the Fermi level. The Fermi level cannot be measured in insulator samples. The W_s work function represents the difference between the Fermi level and vacuum level. Its value varies for different samples, typically in the 2-5 eV range.

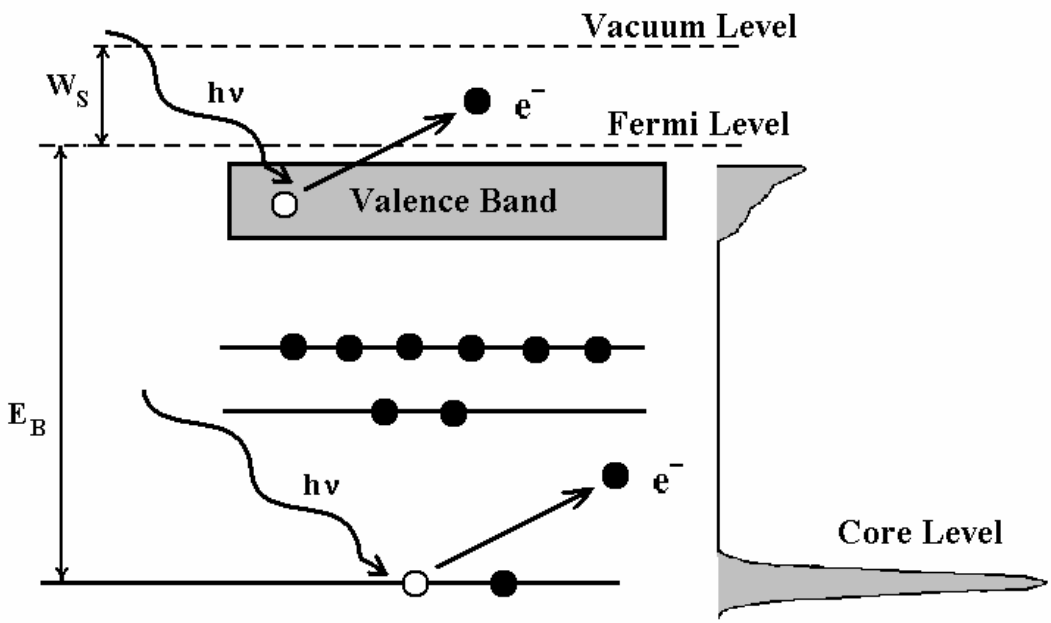

Figure 3.1. Energy diagram of a photoemission process. The electrons can originated either from the localized core level or from the delocalized valence states

As a result of the photoemission process a hole is created inside the atom, which is now in an excited state. Information about the photoemission effect is available in the literature [42, 43, 44, 45, 46]. Transition to the ground state requires that the core level hole is filled by an electron from the outer shell. The result may be a radiative one, the fluorescence photon. In case of excitation with soft X-ray the fluorescence probability is very low. The non-radiative process occurs with higher probability and the result is the emission of a secondary electron, the so-called Auger electron. The energy of the Auger electrons does not dependent on the primary excitation. This behavior makes them suitable for absorption measurements (see next paragraph).

The Auger lines are also visible in the photoelectron spectra. Both Auger and fluorescence are two step processes, unlike simple photoionization, which can be considered as one-step process [47].

The ***one-step model*** of the photoemission process consists of the excitation of an occupied electronic state inside the solid, by absorption of the incident photon, into an empty state outside the solid.

Another approach is the so-called ***three-step model*** of photoemission process. The first step is the photoexcitation of an electron from a filled state follow by the transport of the electron to the surface (second step). The process ends with the escape of the electron into the vacuum (third step).

The escape depth is determined by electron-electron and electron-phonon scattering. Only those electrons that originate from atoms near the surface can leave the sample without energy loss. They produce sharp feature in the photoelectron spectra and are therefore, the most useful. The electrons suffering inelastic scatters contribute mainly to the background intensity and provide less information (***secondary electrons***).

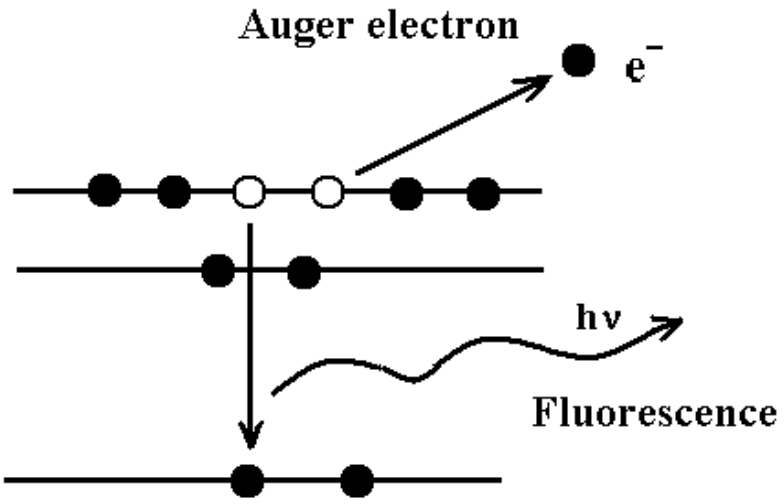

Figure 3.2. Schematic presentation of the Auger and fluorescence process

The electron escape depth depends mainly on the photoelectron kinetic energy and follows a similar curve for most materials. Due to the fact that this escape depth versus photoelectron kinetic energy curve is only weakly material dependent, it is often referred to as ***universal curve***. The minimum escape depth, of few angstroms correspond to a kinetic energy of about 50 eV, (**figure 3.3**). For such small escape depths the information obtained is characteristic of the surface rather than the bulk.

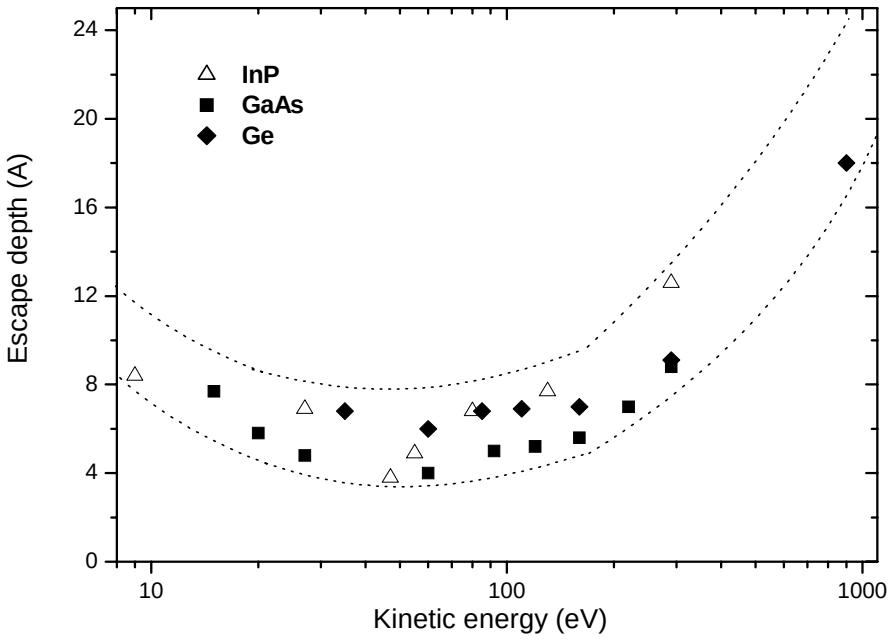

Fig. 3.3. Universal curve for the escape depth of photoelectrons in different semiconductor samples. The values are taken from Ref. [48, 49]

3.2 X-ray absorption

The X-ray Absorption Spectroscopy (XAS) is a technique to probe empty electronic stated and was first used in the 1920s for structural investigation of the matter. Long range order is not required, this means that comparable with the diffraction techniques the absorption measurements provide structure information for both non crystalline and crystalline solids.

By tuning the excitation energy one can probe the partial density of states (empty electronic states) from the bottom up the top of the conduction band in case of condensed matter (**figure 3.4 a**) or discrete unoccupied levels (up to ionization potential) in case of atoms and molecules.

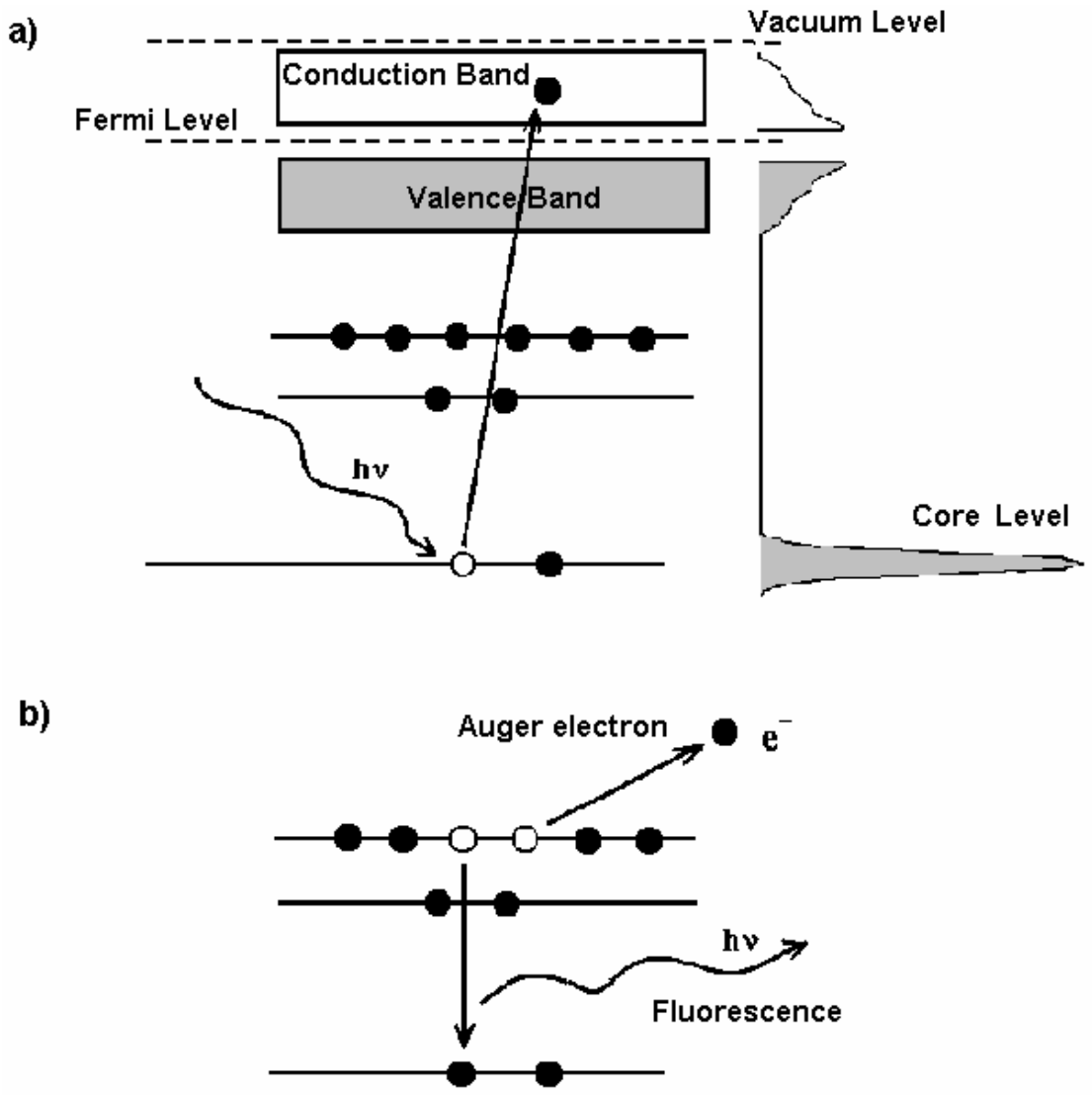

Figure 3.4 a) Schematic representation of absorption process in case of condensed matter. The core electron that absorbs the phonon is projected into the conduction band. b) the decay products (fluorescence or Auger electron) resulting after absorption are sketched here.

The absorption coefficient is proportional with the transition probability from an initial state |i> to a final state |f > that can be calculated from Fermi's "Golden Rule" [40].
The dipole selection rules assure that the angular momentum *l* has to change with 1 for an allowed transition or in other words $\Delta l = \pm 1$. For example, in case of the K-edge, the electrons that are in the most tight bound (*1s* core level) can have transitions only to the *np* electronic states.

Several techniques for measuring absorption spectra have been developed and can be labeled as direct or indirect detection [50, 51].

The direct one and the most obvious way is to measure the absorption of the sample by monitoring the incoming I_0 and the transmitted *I* flux. The absorption is simply given by:

$$\mu x = \ln\left(\frac{I_0}{I}\right) \tag{3.2}$$

where μ is linear absorption coefficient and *x* is the sample thickness. This method is somehow technical limited by the thickness of the sample. For example, in case of soft X-rays, regime the light is completely absorbed after passing few μm.

The indirect detection techniques are based on the fact that the probability of exciting an electron from a core level and the subsequent core hole creation is actually giving the absorption coefficient. Therefore, any process whose statistical average is proportional to the annihilation of the core hole is also proportional to the absorption coefficient and can be used for XAS detection. The core hole can be filled by a radiative or nonradiative electronic transition from a lower binding energy level. Radiative transitions result in *fluorescence* X-ray emission, while *Auger* electrons are produced in the nonradiative process (**figure 3.4 b**).
Auger emission and X-ray *fluorescence* are competing processes and their relative strengths depend on the atomic number of the absorber. For light elements, with Z less than 30, the Auger emission has a larger probability to occur that the fluorescence. For the same element, the fluorescence yield is lower for the L-edge than for K-edge.
For investigation of Cu $L_{2,3}$-edges the *Auger yield* collected with our Omicron electron analyzer is an obvious choice.
If all the electrons are measured, including the secondary ones the technique is called total electron yield – *TEY*. The *TEY* detection for the present investigation means measuring the sample current. The technical details are given in the experimental section.
The *Auger yield* measurements are rather (more) surface sensitive with a sampling depth comparable with photoelectron *escape depth* (see photoemission section). For Ar LMM electrons with a kinetic

energy of 213 eV the escape depth is about 10 Å while for the kinetic energy of Cu LVV Auger electrons is 917 eV with a corresponding escape depth around 15-20 Å.

The *TEY* spectra are more bulk sensitive with a sampling depth given by the electron *penetration length*. The electron penetration length is defined as the length, after which the electron has deposited all its energy in the material. For Cu L-edge the value was found to be around 100 Å [52].

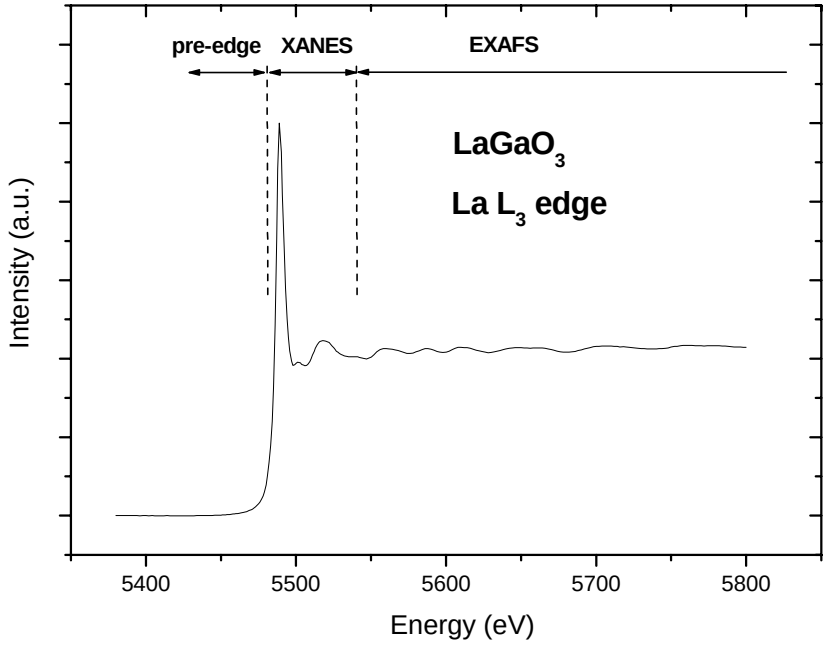

Figure 3.5. Schematic representation of the absorption spectrum for La L_3 edge of a bulk $LaGaO_3$ sample. The spectrum is divided in three distinct regions: the pre-edge, the near edge structure XANES and the fine structure range EXAFS that stretches hundreds eV from the absorption edge. From [1)]

Absorption spectra can be divided in three different regions:

- the *pre-edge structures*
- the *X-ray Absorption Near Edge Structure* (*XANES*)
- the *Extended X-ray Absorption Fine Structure* (*EXAFS*)

The *pre-edge* range defines discrete transition of the excited electrons to the unoccupied bound states. Sharp features are clearly visible particularly in case of absorption spectra of atoms, molecules and

[1] measured by R. Nietubyc at LURE, Orsay, France, 2001

insulators. The absorption edge corresponds to a photon having enough energy to just free a bound electron inside the atom, in other words, it gives the Fermi level (of the sample).

The near edge structure *XANES* covers the range between the absorption edge and the point at which the extended x-ray absorption fine structure *EXAFS* begins and stretches typically few tens of eV above the edge. A more accurate definition for the *XANES/EXAFS* limit is given by Bianconi [53]. He suggest that the energy limit should be that at which the wavelength of the excited electron is equal to the distance between the absorbing atom and its nearest neighbors.

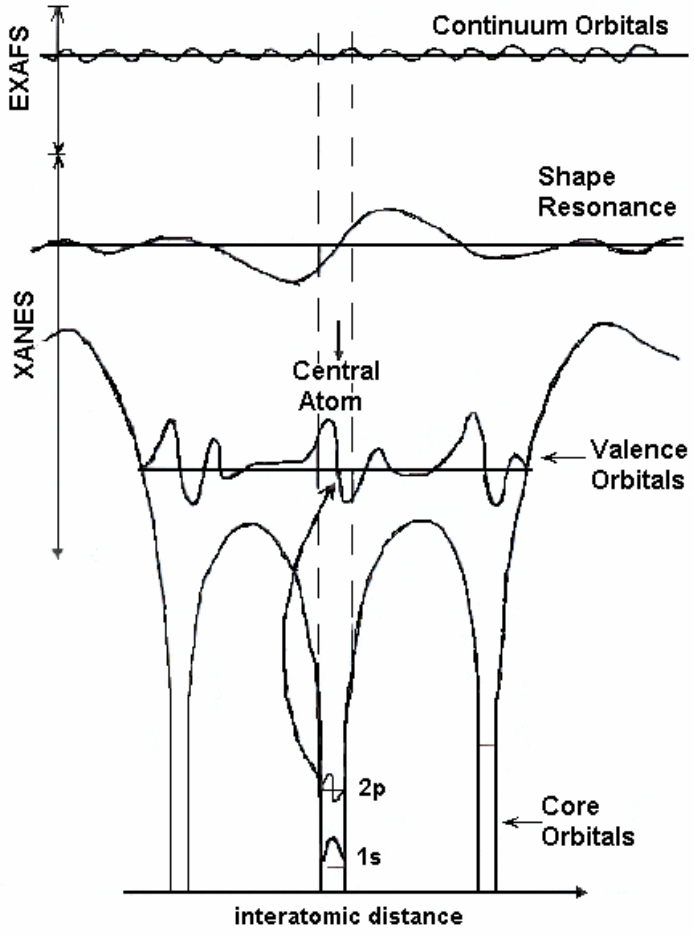

Figure 3.6. Pictorial view of the core initial states and of the final state radial wave functions for core transition. Important to notice the contribution and amplitude for XANES and EXAFS regimes. From [50]

In the *XANES* regime, the multiple scattering of the excited electron confers sensitivity to the details of the spatial arrangement of the atoms neighboring the absorbing one, not only their radial distances but also bond angles.

For crystalline materials, the multiple scattering and the band structure approaches are two equivalent ways to calculate the same unoccupied density of states.

Important to notice that *XANES* structures are usually much stronger than the EXAFS oscillation, a practical aspect when studying dilute systems (**see figure 3.6**).
High experimental resolution (less than 1 eV) is required for investigating the sharp structures in this regime.

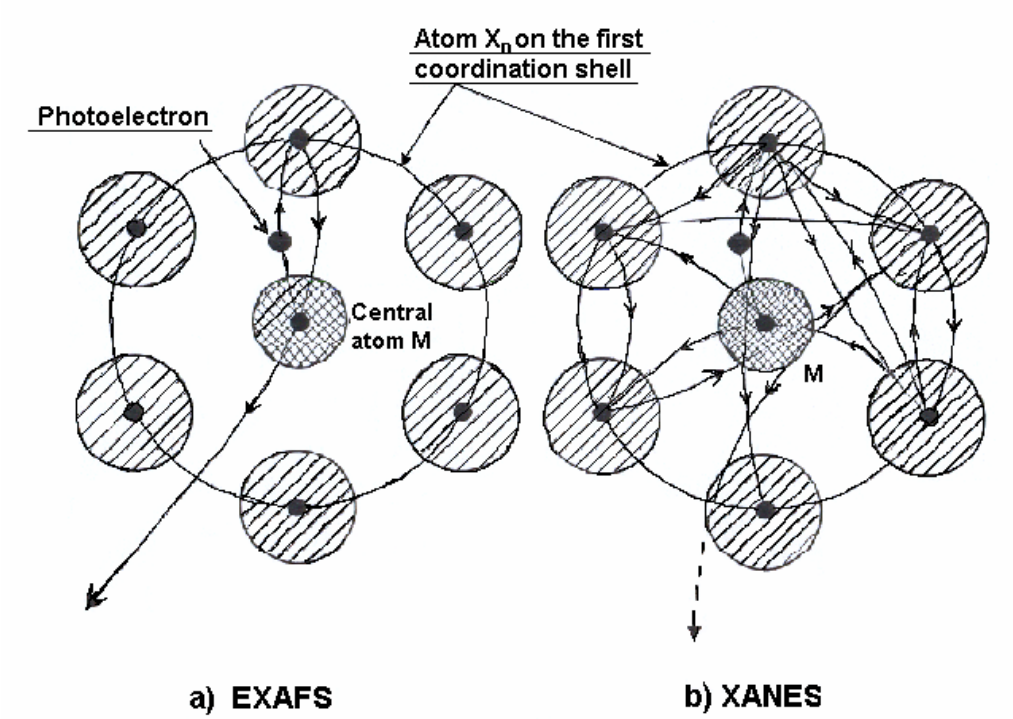

Figure 3.7. Scattering process for EXAFS and XANES, single and multiple scattering are sketched here. From [50]

The *EXAFS* range extends hundreds of eV above the *XANES* limit and is based on the single scattering approximation (as long as the scattering is low). The outgoing wave function is scattered backward only once from the surrounding atoms before being combined with the unscattered wave.
From the point of view of the scattering theory, one can say that at high energies the scattering of the excited electrons is so weak that the main contributions to the final state wave function in the vicinity of the absorbing atom come from paths in which the electron is scattered only once (single scattering). Once the photoelectron energy is lowered into the *XANES* region, multiple scattering becomes more and more important-see **figure 3.7**.
Because the EXAFS region is dominated by the single scattering the information it contains is purely geometrical and rather easily extracted (Fourier transformation) [50].

EXAFS does not occur for isolated atoms but only appears when atoms are in a condensed state. It gives no information on long-range order and thus does not replace diffraction techniques but only complements them.
Low experimental resolution (~6 eV) is sufficient for *EXAFS* investigations.

3.3 Instrumental resolution. Core level spectra

Photoelectron spectroscopy technique requires an appropriate light (radiation) source. Laboratory sources like ***gas discharge lamps*** or ***X-ray tubes*** (metallic anodes) are used for producing UV (vacuum ultraviolet) photons and X-ray photons, respectively and the techniques are called UPS and XPS, respectively. One common emission line in the soft X-ray regime is the Al K_α with an energy of 1486.6 eV. However this line is much broader (~1eV) than those of the gas discharge lamps and its width determinates the rather poor overall resolution. The use of an x-ray monochromator can reduce the width to ~0.1eV but also results in a considerable loss in intensity and deterioration of the signal-to-noise ratio.
The gap between UV and X-ray photons is bridged by synchrotron radiation. High energy electrons (~GeV) confined by magnetic fields move in an nearly circular orbit and emit a continuum of radiation extending from the far infrared to energies of few keV. When coupled with a suitable monochromator, synchrotron radiation provides a tunable light source covering all energies of interest for photoelectron spectroscopy with a spectral resolution better than 0.1 eV. Since the inelastic mean free path of the photoelectrons is directly dependent on its kinetic energy, one can vary the sampling depth, by simply tuning the photon energy. Hence, the photoelectron spectra of a particular core-level measured with different excitation energies, make it possible to distinguish between volume and surface atoms.
The energy resolution $\Delta E_{monochr}(eV)$ of the SX 700 monochromator installed at the Hasylab BW3 beamline is given by the following formula:

$$\Delta E_{monochr} = 2.08 \cdot 10^{-4} \cdot E_{hv}^{3/2} \cdot d_{slit}(mm) \qquad (3.3)$$

where E_{hv} is the radiation energy and d_{slit} is the width of the monochromator exit slit.

The hemispherical electron analyzer type EA 125 U7/7 is a multichannel detection system from Omicron. There are two modes of analyzer operation *Fixed Retarding Ratio (**FRR**)* and *Fixed Analyzer Transmission (**FAT**)* [30]. *In the Fixed Retarding Ratio (**FRR**) Scan Mode*, the electrons entering the analyzer are retarded with the help of the lens system that provides a constant ***k*** ratio of their kinetic energy $\boldsymbol{E_k}$ to analyzer pass energy $\boldsymbol{E_p}$:

$$k = \frac{E_k - \phi_a}{E_p} \approx \frac{E_k}{E_p} \tag{3.4}$$

where Φ_a is the analyzer work function

Resolution and sensitivity are very much dependent on the kinetic energy. Particularly the resolution decreases considerably for kinetic energies higher than 150 eV (see 3.5).

The other mode is *Fixed Analyzer Transmission (**FAT**) Scan Mode*, in which the analyzer pass energy ***E*$_p$ is** held constant and the retarding voltage is changed. The advantages are constant resolution throughout the whole kinetic energy range and increased sensitivity for the low kinetic energy regime. All the measurements were performed in the ***FAT** Scan Mode*.

The analyzer is a band pass energy filter for electrons at a specific energy E_p and has a finite energy resolution ΔE_a which is dependent on the chosen mode of operation and specific operating conditions. The energy resolution of the analyzer is given approximately [30] by:

$$\Delta E_a = E_p \left(\frac{\frac{d_{entr} + d_{exit}}{2}}{2R_0} + \alpha^2 \right) \tag{3.5}$$

where d_{entr} is the diameter of the entrance slit, d_{exit} is the width of the exit slit, R_0 mean radius of hemisphere, α half angle of electrons entering the analyzer (at the entrance slit; in radius units – in our case α=3º)

The total instrumental resolution is given by:

$$\Delta E_{inst} = \sqrt{\Delta E_a^2 + \Delta E_{monochr}^2} \tag{3.6}$$

hν eV	d_{slit} μm	E_{pass} eV	d_{enter} mm	d_{exit} mm	ΔE_{instr} meV
176	80	5	6	5	130
176	80	10	6	5	250
291	80	10	6	5	260
368	80	10	6	5	270
579	80	10	6	5	340

Table 3.1 - the total instrumental resolution for different radiation and pass energies. The electron analyzer has the main contribution at the instrumental resolution in case of low excitation energies

The shape and position of a core level line is determined by intrinsic and extrinsic factors. Intrinsic parameters are the binding energy, the spin orbit splitting, the branching ratio and the lifetime of the core hole system. Instrumental resolution of analyzer and the spectral broadening (determined by the monochromator) represent the extrinsic contributions. According to the photoelectron emission theory the peak shapes are typically given by a Lorentzian contribution due to the limited lifetime of the core hole state and a Gaussian broadening mostly due to the incoming radiation energy profile and the resolution of the analyzer. Gaussian contribution may also be related to the thermal broadening, chemical, structural and electronic (by dopants) inhomogeneities in the surrounding of the emitting atom.

The electron core level spectra are typically fitted with Voigt functions. The Voigt function *f(E)* is a convolution of a Lorentzian L(E):

$$L(E) = \left\{ 1 + 4\frac{(E - E_L)^2}{\Gamma_L{}^2} \right\}^{-1} \tag{3.7}$$

and Gaussian G(E):

$$G(E) = \exp\left\{ -4\ln 2\frac{(E - E_G)^2}{\Gamma_G{}^2} \right\} \tag{3.8}$$

functions and it was found to give the best results in fitting the core-level lines:

$$f(E) = f(L * G) = \int_{-\infty}^{\infty} L(E')G(E - E')dE' \tag{3.9}$$

The parameters $E_{L,G}$ and $\Gamma_{L,G}$ are the peak position and the full width at half maximum (FWHM), respectively.

Chapter 4. InP nanocrystals

In this chapter the investigations of the size selected semiconductor **InP nanocrystals** using **photoelectron spectroscopy (PES)** technique with synchrotron radiation are presented. These samples were prepared in H. Weller's group (Institute for Physical Chemistry, University of Hamburg) by an organometallic approach using indium chloride ($InCl_3$) and tris-(trimethylsilyl)phosphine ($[(CH_3)_3Si]_3P$) as precursors as well as trioctylphosphine (TOP) and trioctylphosphine oxide (TOPO) as stabilizing and size regulating agents. As prepared InP nanocrystals, exhibit poor photoluminescence (PL) quantum yield, usually less than 1%. However, the PL quantum yield can be drastically enhanced to about 20-30% with some additional treatments like photoetching of the nanoparticle surface with fluorine compounds. The nanocrystals posses large surface to volume ratio and hence, the surface structure of these nanocrystals play an important role in determining their properties. So, it is necessary to investigate and understand the surface structure of these nanocrystals, in order to improve their properties for potential applications in nanostructured devices.

The interest for nanoscale materials experienced great development in the last decade leading to a new interdisciplinary field of science. Semiconductor solids exhibit strong size-dependent properties in the range of approximately 1-20 nm resulting in a number of technologically relevant and scientifically challenging areas [54].

Under UV radiation and depending on the preparation methods some QDs show strong photoluminescence yield, a desirable property for the development of optoelectronic devices. It would be useful to clarify the chemical nature of the surface states in order to improve the photoluminescence yield for further nanostructure applications.

While II-VI semiconductor nanocrystals were intensively studied during the last decade, less information is available for their III-V analogues. One reason is that III-V semiconductors are more covalent compounds and high temperatures are usually required for their synthesis. Only a limited number of papers discussing the synthesis and characterization of InP [55, 56, 57, 58], GaP [59] and InAs [60, 61] nanocrystals appeared in the last few years. The III-V compounds usually have relatively covalent bonding and direct band gap structure, larger bulk exciton radii and smaller effective masses which makes them promising candidates for various optoelectronic devices. Another important aspects are so called "green chemical principles" dominating modern chemistry that base on the development of environmentally friendly chemical methodologies and materials [62]. From this point of view III-V compounds like InP are more attractive than the high toxicity cadmium-related II-VI ones.

A point of special interest is the fabrication of highly luminescent nanocrystals. Therefore, the particle surface has to be passivated, i.e., surface dangling bonds which give rise to non-radiative recombination have to be saturated for example by organic ligands. In case of InP efficient passivation of the surface requires special treatments and one option is etching with certain suitable fluorine compounds.

One of the powerful techniques to investigate surfaces is Photoelectron Spectroscopy (PES) combined with variable photon energy source, which gives the possibility to tune the surface sensitivity of the experiment. Modern synchrotron sources satisfy these needs with high photon fluxes and better energy resolutions. High resolution In 3d and P 2p core level spectra of several (different) InP nanocrystal samples were measured at different excitation energies. Commercially available InP bulk crystals oriented in (110) direction were also analyzed for the comparison and to get a better understanding of the nanoscale InP crystals.

4.1. Preparation of InP nanocrystals

Size selected InP nanocrystals were prepared by the standard method developed by Nozik et al. [63], based on Well's method of nanocrystal synthesis [64]. The results are nanoscaled samples with high degree of crystalinity [55, 65]. Briefly, the following reaction has been performed in a glove box, under protective nitrogen atmosphere:

$$InCl_3 + \left[(CH_3)_3Si\right]_3P \xrightarrow{150-280^0C,\ \text{stabilizing agents}} InP + 3(CH_3)_3SiCl \qquad (4.1)$$

with TOPO-TOP as particle stabilizing agents (to prevent the formation of bulk InP phase).
A schematic drawing of the TOP and TOPO ligands is presented in **figure 4.1**.

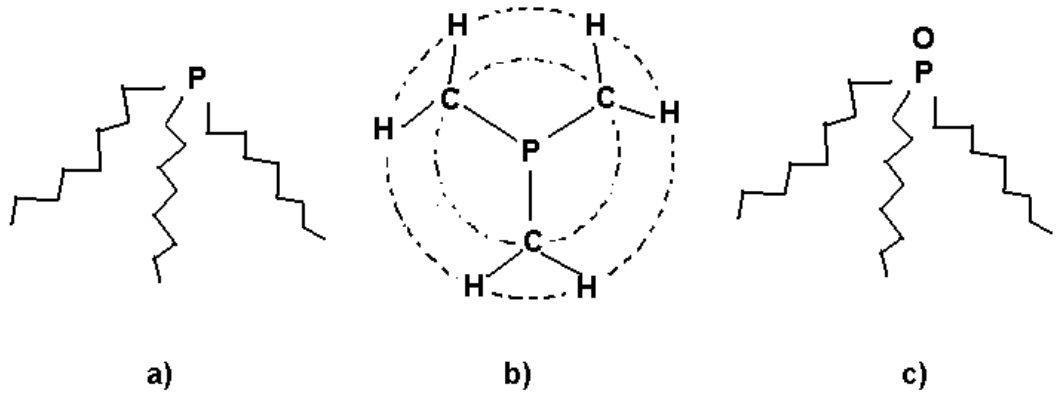

Figure 4.1. Schematic representation of the a) TOP and c) TOPO ligands; b) spatial view for the TOP molecule. Chemical formula for the *Trioctylphosphin* is **$(C_8H_{17})_3P$** and for *Trioctylphosphin oxide*-**$(C_8H_{17})_3PO$**

The InP particles formed after the nucleation stage are usually amorphous and annealing for 1-6 days at temperature above 250°C is required to obtain crystalline InP nanoparticles. The results are nanocrystals with sizes from ~2.2 to 6 nm. The relatively broad size distribution (~25-30%) requires post-preparative size selective precipitation. The size selection technique is detailed in [65]. Briefly, the as prepared InP nanocrystals with broad size distribution are dispersed in toluene. After adding methanol the nanocrystals start to coagulate and the largest nanoparticles exhibit the strongest attractive van der Waals forces and aggregate before the smaller nanoparticles. The large nanocrystals that coagulate first can be isolated by filtration (0.2 μm membrane filter) and can be re-dissolved in toluene. This procedure is then repeated several times. From the InP crude solution one can obtain up to ten size selected fractions with a diameter distribution narrower than 8-10% of the average size.

The powder X-ray diffraction (P-XRD) patterns of as prepared nanoparticles reveal the bulk InP structure (zinc-blende phase) and the broadening of the diffraction peaks increases once the particle size decreases. The diffraction measurements yield also an approximately In:P ratio of 1:1.

By simple considering the Schrödinger equation for the case of an electron confined inside a cube of volume L^3 one obtains an energy dependence of $E(L) \sim 1/L^2$. However this result proves to be inadequate for describing the size dependence of the band gap E_g of nanoparticles. Fu and Zunger presented pseudopotential plane wave electronic structure calculations for InP quantum dots [66] and the theoretical results agree with the corresponding experimental data. The size (diameter d) of the quantum dots is related with the gap value E_g by the following equation:

$$E_g(d) = E_g^{bulk} + \frac{A}{d^n} \qquad (4.2)$$

where

$$E_g^{bulk}(10\,K) = 1.45\,eV$$
$$n = 1.3611$$
$$A = 55.2527$$

The gap values of size selected InP QDs can be estimated from absorption measurements:

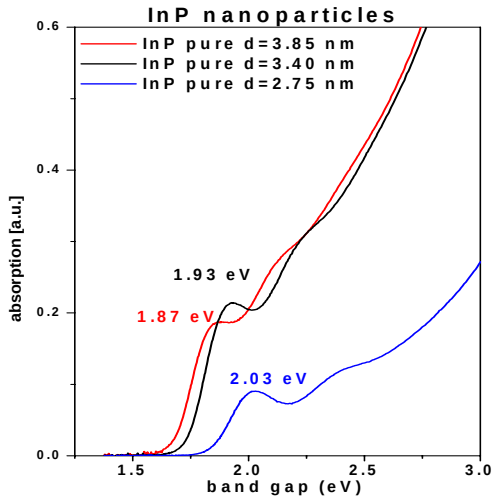

Figure 4.2. Variation of the band gap with the size of the InP nanocrystals. From [65]

A direct method of measuring the size of the nanocrystals is the TEM (transmission electron microscopy) technique. High resolution TEM images of InP nanocrystals show crystalline nanoparticles with resolve lattice fringes, see **figure 4.3.**

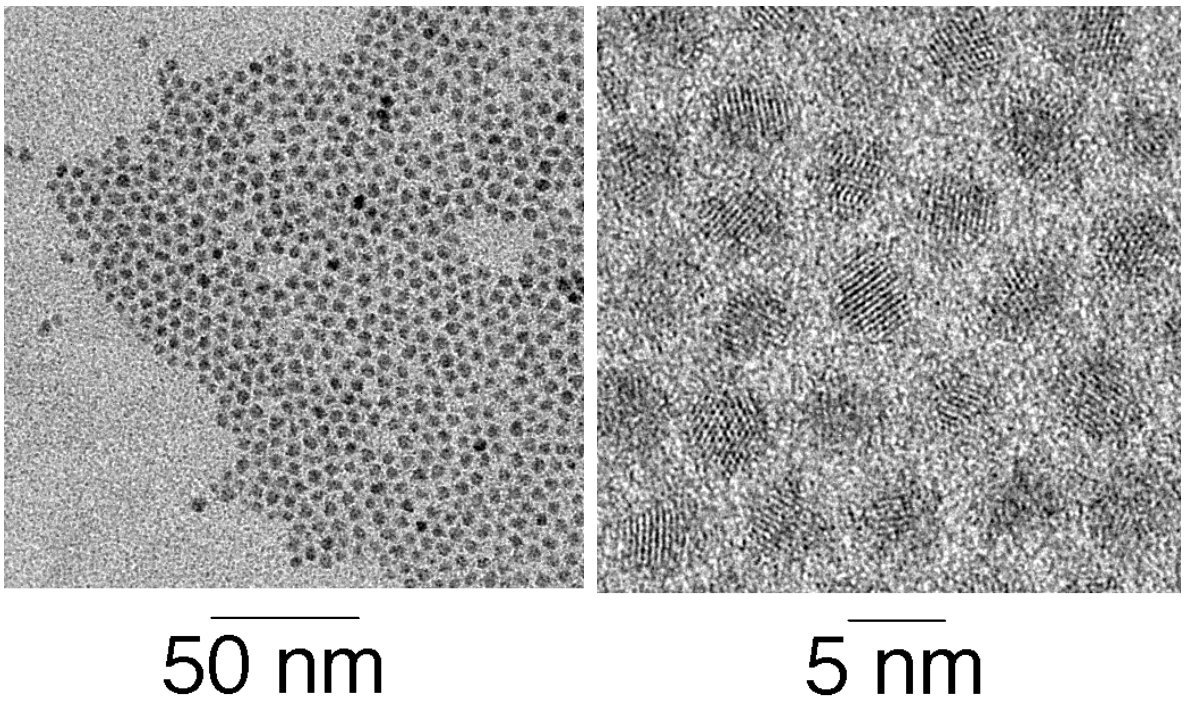

Figure 4.3. TEM (left) and HRTEM (right) of size selected InP. [65]

Another way of comparing the sizes obtain by TEM is simply to measure the broadening of the peaks provided by the XRD technique. The broader the peak, the smaller the nanoparticle mean size is [65].
As prepared, the InP nanocrystals display poor luminescence properties, due to non-passivated surface sites (dangling bonds, DBs), which provide surface states in the band gap. A phosphorous dangling bond leads to an energy state just above the valence band, which acts as a trap for the photogenerated holes providing non-radiative recombination pathways. Similarly, the In dangling bond has an energy level below the conduction band [66].
Experimental and theoretical studies [58, 66] suggest that proper post-preparative modification of the particle surface eliminate the undesirable dangling bonds. Passivated dots are expected to have no surface states in the gap and over a wide range of ligands the band-edge states of the nanocrystals are unchanged.
A very successful way of improving the luminescent properties proves to be the HF treatment of the InP nanoparticles. Nevertheless, the existing procedure of HF etching is not reproducible with respect to the resulting PL quantum efficiency and a systematically study of the whole process is required.

TEM images of the etched InP nanocrystals show that the nanocrystals retain after etching their monodispersity and crystallinity. The resulting particle diameter is comparable with the value corresponding for "pure" nanoparticle and diffraction measurements indicate an In to P ratio close to one and there are signs for small amount of fluorine (less than 10%) in the etched InP nanocrystals.

4.2 Bulk InP(110) surface

4.2.1 Oxygen free InP (110) surface

In order to allow a detailed analysis and discussion of nanocrystal properties, a bulk InP sample was investigated under the same experimental conditions.

The III-V InP semiconductor crystallized in the cubic ***"zincblende"*** structure and can be easily cleaved along the (110) surface. The "***zincblende***" structure consists of two interpenetrating face centered Bravais lattices, displaced along the body diagonal of the cubic cell by one quarter of the diagonal length (see **figure 4.4 a**). The chemical bonding has ionic contribution and the coordination number for the volume atoms is 4 (i.e., the number of neighboring atoms is the same for both In (cation) and P (anion) and it is 4). But the surface atoms have only 3 neighboring atoms and 1 dangling bond. Nearest neighbor distance for InP bulk is 0.254nm, $d_{110} = a_0\sqrt{2}/4$ is the distance between (110) lattice planes with a_0=0.583 nm [67].

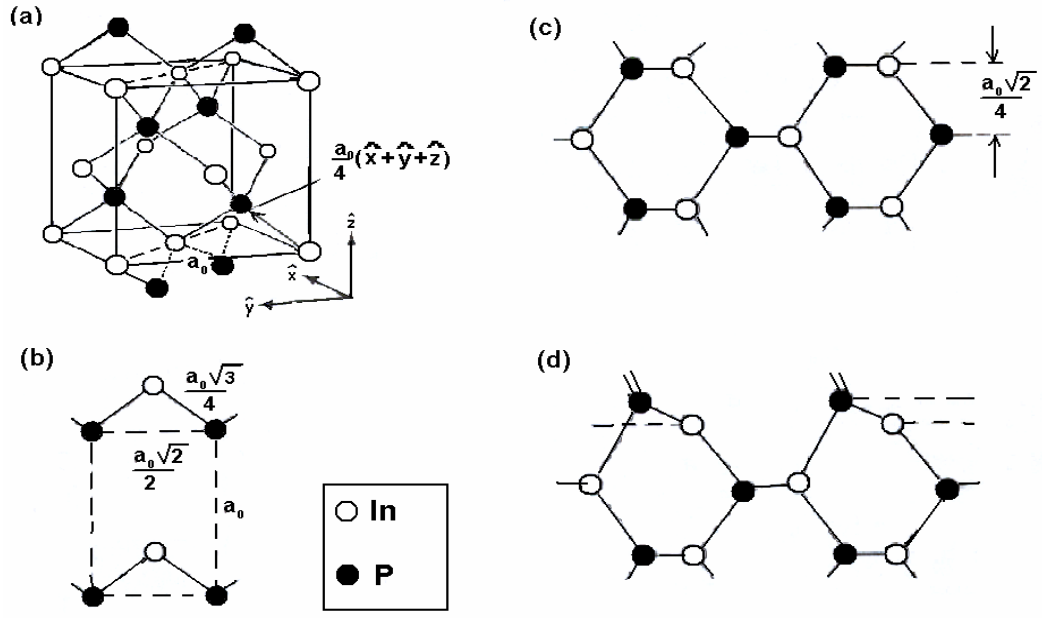

Figure 4.4. a) Atomic arrangement of bulk InP with zincblende structure. b) Top view for bulk InP truncated (110) surface. c) Side view of the (110) surface (surface atoms are not relaxed). d). Side view of the (110) surface (surface atoms are relaxed, with the P atoms raised)-From [67].

No reconstructions are reported in case of cleaved clean InP (110) surfaces, however, the top most atoms relax with the anions being raised [67]. This relaxation results in slightly different binding energies of the core-levels for surface atoms when compared with the bulk atoms (***S**urface **C**ore-level **S**hift-**SCS***). The corresponding photoemission spectra for **In 4d** core-level lines and **P 2p** core level lines are shown in **figure 4.6 a)** and **4.7 b)**, respectively.

A good review of these investigations has been reported by Mönch [67, 68]. The present discussion is limited only for InP(110) surface.

Experimental results regarding the InP(110) ***SCS*** were obtained by T. Kendelewicz [69]. In case of **In 4d** core level spectra the fitting procedure revealed a surface peak shifted by 0.3 eV to higher binding energy relative to its bulk counterpart. The spin-orbit splitting was in this case 0.86 eV. However, the authors were not able to resolve a shift in case of **P 2p** and assume that its value is too small.

A successful way of fitting both **In 4d** and **P 2p** core-level spectra is presented in the work of W. G. Wilke [70]. The results for **In 4d** are consistent with the previous observations of T. Kendelewicz and the ***SCS*** value is 0.325±0.026 eV. The spin-orbit splitting was found to be 0.87 eV and the Lorentzian width is 0.22 eV. The line shape analysis gave a spin-orbit splitting of 0.85 eV for **P 2p** level. With a Lorentzian width of 0.16 eV the magnitude of the ***SCS*** is 0.307±0.02 eV towards lower binding energies. Further, the assignment for the shifted **P 2p** surface core-levels was confirmed by analyzing the data measured after depositing about 1 monolayer of CdS on top of a InP(110) surface. Wilke reported that CdS grows epitaxially on InP(110) in a metastable zinc-blende structure [71]. This means that the growth of the epitaxial CdS overlayer removed the ***SCS*** because the vacuum termination of the substrate (InP(110)) is removed. The topmost In and P atoms are in a similar environment as those in the bulk crystal and the results are narrower peaks by the fact that the SCS signal is now significantly reduce in intensity comparable with the clean InP(110) surface.

The InP bulk sample used in the present investigation is from **Crys Tec Gmbh (**n type-doped with S atoms, with a S concentration of $(4.5\text{-}5.0)\times10^{18}$ /cm^3) was cleaved in UHV at a base pressure of $p=2\cdot10^{-9}$ mbar.

The resulting (110) surface was investigated using PES with synchrotron radiation in the regime of 291-579 eV. The EDC spectrum measured using an excitation energy hv=579eV shows the lines corresponding to only In and P, which confirms the surface is free from C, O or other impurities –see **figure 4.5**.

The theoretical branching ratio in case of spin orbit splitting is given by the following equation:

$$b.r.=l/(l+1) \qquad \text{for angular momentum } l>0 \tag{4.3}$$

This means that for **P 2p** core level lines the branching ratio is 1/2 and the ratio for the **In 3d** lines is 2/3.

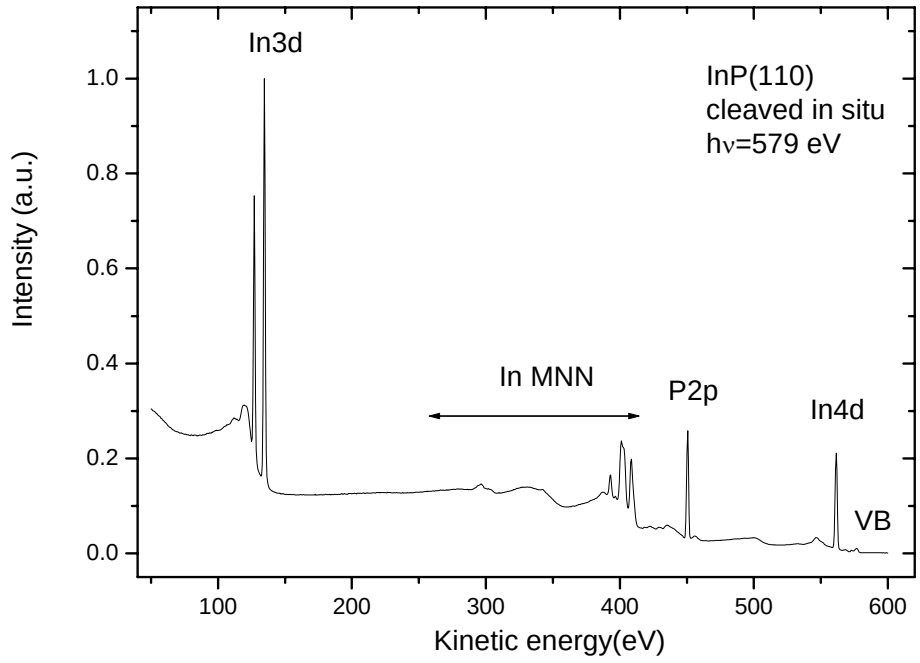

Figure 4.5. Survey spectra for InP(110). There is no indication of surface contamination (no O or C peaks can be seen).

In reality this ideal value of the branching ratio is effected by different values of photoionization cross section and different mean free path of the photoelectrons due to slightly different binding energies for the two lines with a total quantum number j=l-s and j=l+s.

The spectra were fitted with a minimum number of Voigt components followed by subtraction of the combined polynomial and Shirley-type background [72]. A Lorentzian broadening value of 0.23±0.03 eV and spin-orbit splitting value of 0.86 ± 0.01 eV held fixed for all components during fitting of **In 4d** spectra. The fixed parameters used here are in agreement with various studies for InP [69, 70].
The component labeled **s** is more pronounced at lower kinetic energy, i.e., when the surface sensitivity is higher (see chapter 3 - ***the mean free path curve***). These components are, therefore, identified with atoms having a distinct surface environment in the nanocrystal. The component **b** that increases in relative intensity once the excitation energy increases is due to In atoms in the interior of the nanocrystal volume (**figure 4.6 a**). The energy dependence for bulk to surface ratio is displayed in **figure 4.6 b)**.
The ***SCS*** is 0.317±0.003 eV. The Gaussian width increases from 0.34±0.01 eV (excitation energy, hν=292.5 eV) until 0.47±0.02 eV (hν=579 eV). The increase in the Gaussian width is due to decrease in the instrumental resolution at higher photon energies (see table 3.1)

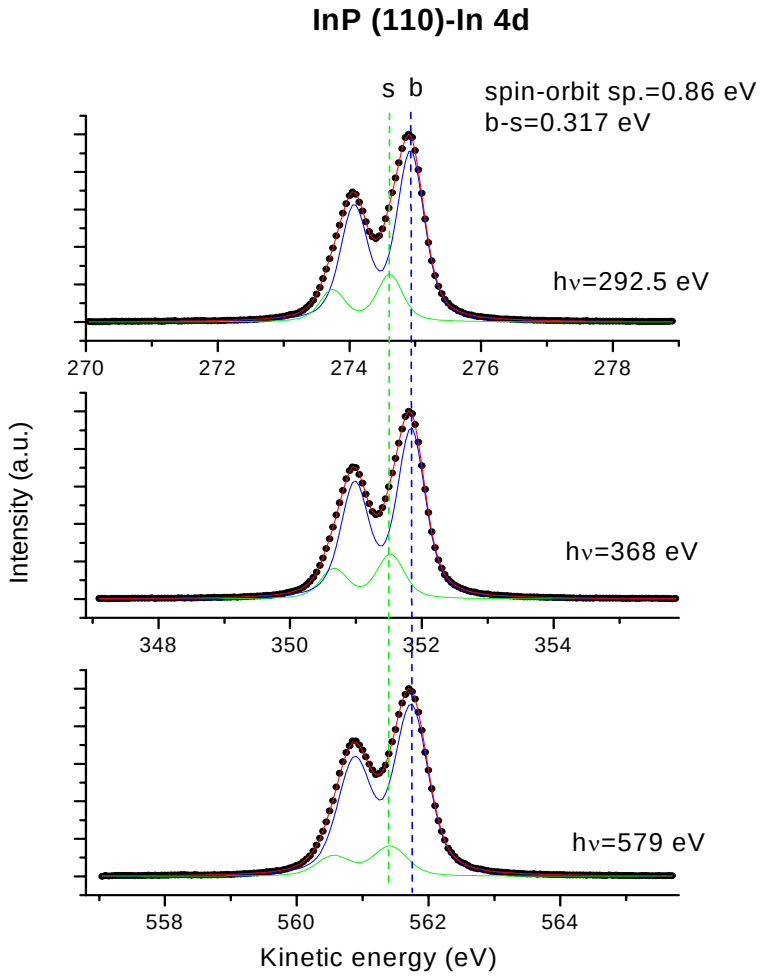

Figure 4.6 a). **In 4d** core-level photoemission spectra of InP (110) bulk surface. Component **b** is due to atoms in the volume of nanocrystals and **s** is a surface core-level shift.

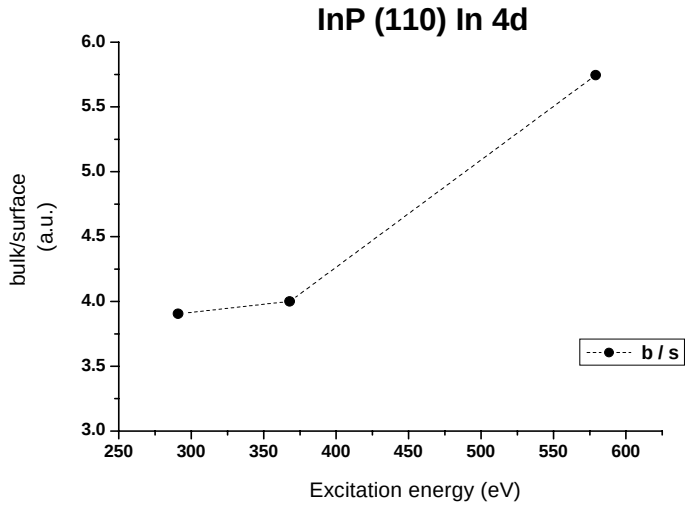

Figure 4.6 b). Bulk to surface ratio for In 4d core level spectra. The dots are guides to the eye.

The attempt of fitting the **In 4d** core level lines with only one component results in rather large mismatched between the experimental curve (*the measured spectrum*) and the fitting curve (*the Voigt doublet*)-see **figure 4.7 a)**. The excitation energy was 579 eV.

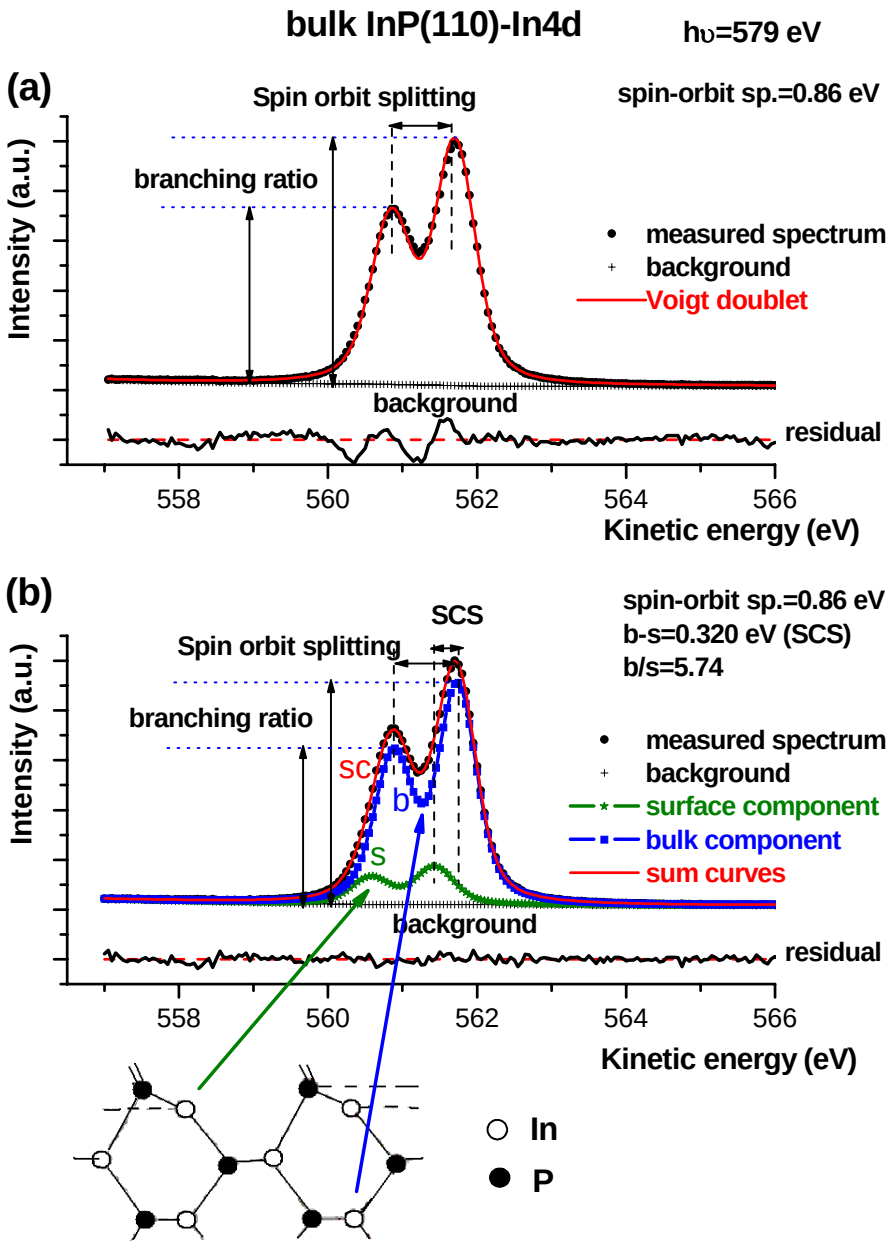

Figure 4.7 a). The **In 4d** core level lines recorded with an excitation energy hν=579eV. The quality of the fitting procedure is low if only one Voigt doublet is used. 4.7 b) The fitting quality improves considerably when two components are used. The bulk component **b** reflects the signal from the volume In atoms and the surface contribution **s** correspond to the In atoms located at the (110) surface. The values for the spin orbit splitting and the surface core level shift (***SCS***) are also given. The background and the residual curve are shown here; one can clearly see difference between the two ways of fitting: with one doublet and with two Voigt doublets.

Figure 4.7 b) shows the successful way of fitting the same **In 4d** lines with two Voigt doublets. The sum curve of bulk **b** and surface **s** contributions match very good with the *measured spectrum* and the *residual curve* is the right indicator for that. The surface core level shift (***SCS***), the branching ratio and the spin-orbit splitting are shown here. The contribution of different In atoms (surface or volume atoms) is also sketched.

The background, which is an active parameter of the fitting procedure is this time present. In order to avoid the load of the figures, the next spectra are shown without the residual curve and with subtracted background that is normally done at the end of the fitting procedure.

In case of **P 2p** core level spectra good data fits are also possible with two Voigt doublets.

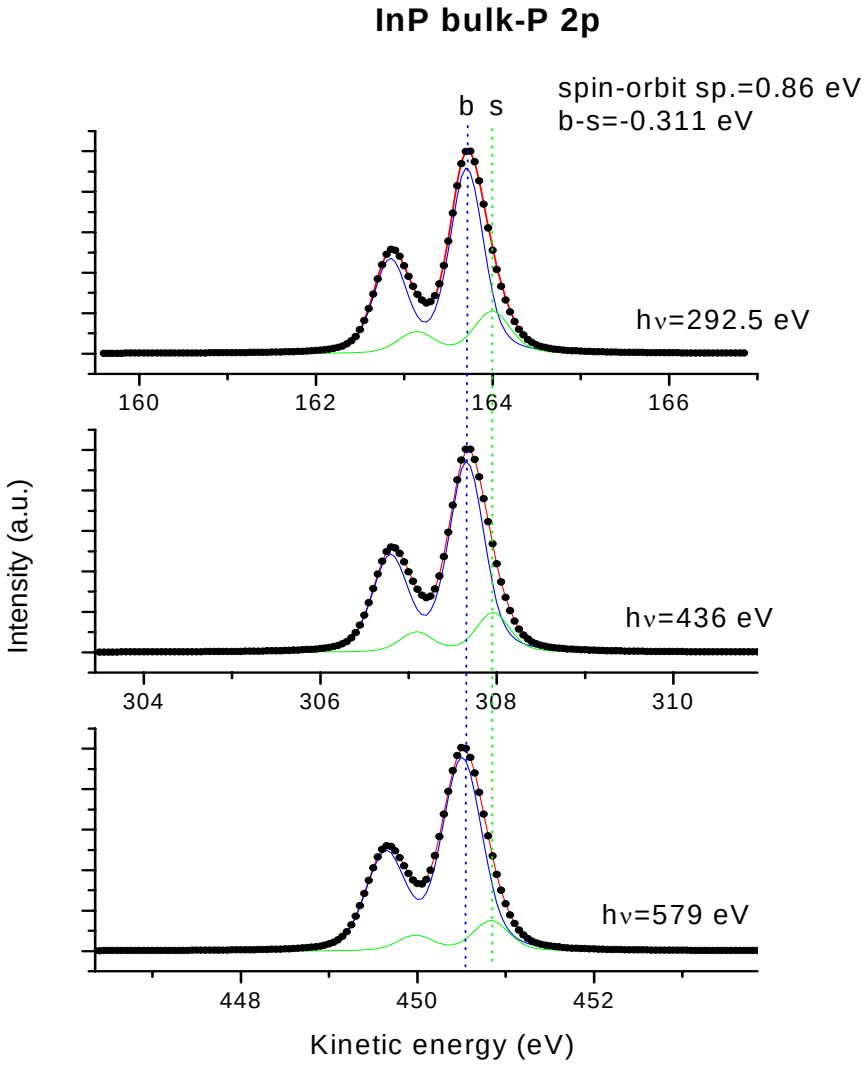

Figure 4.8 a). **P 2p** core-level photoemission spectra of InP (110) bulk surface. Component **b** is due to atoms in the volume of nanocrystals and **s** is a surface core-level shift.

Figure 4.8 a) indicate a fix spin-orbit splitting of 0.86 eV for a constant branching ratio of 1/2. The intensity of the component **b** increases with increasing incident photon energy or kinetic energy of the photoelectrons. Hence this component is assigned to the atoms in the interior of the nanocrystal. The contribution from the surface atoms, component **s** is shifted with an average value of 0.311 eV to the higher kinetic energy with respect to the volume component **b**. The SCS magnitude of 0.311±0.003 eV and the Lorentzian width value of 0.17±0.02 eV are consistent with the results of W. G. Wilke et al.; the theoretical prediction of the same authors indicates also a shift to higher kinetic energy for P 2p lines [70].
The Gaussian width increases from 0.36±0.01 eV (excitation energy, hν=292.5 eV) until 0.42±0.02 eV (hν=579 eV).

As expected the bulk to surface ratio strongly increases with the increasing excitation energy (see **figure 4.8 b**)

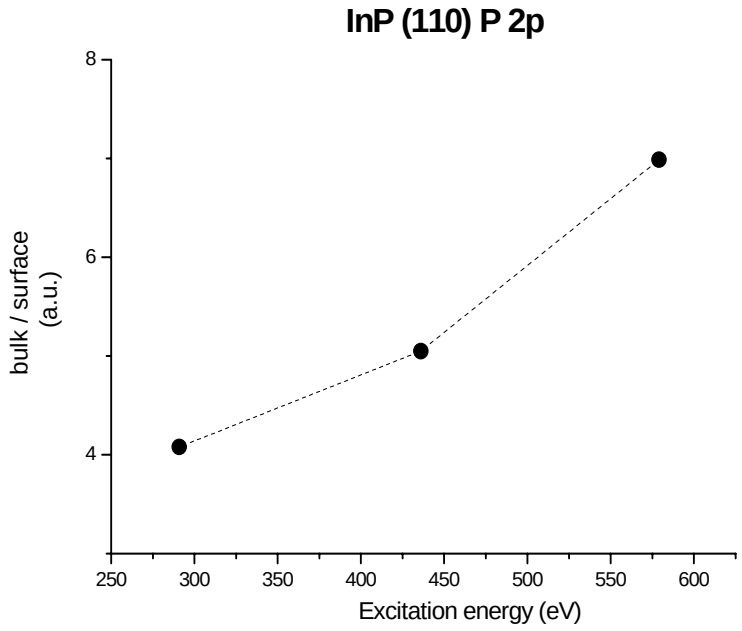

Figure 4.8 b). Bulk to surface ratio for P 2p core level spectra. The dashed line is to guide the eye.

4.2.2 Oxidation of InP(110) surface

Considerable interest was shown in the eighty's for the investigations of the oxide interfaces in case of III-V semiconductors and most of the work involved InP and GaAs surfaces. Particularly, InP was considered to be a promising candidate for MOSFET devices. The quality of the semiconductor-

insulator interface attracted considerable attention since the InP surface proves to be very active (favorable) for chemisorption of oxygen atoms, resulting in the formation of native oxide layers.

Procedures involving room temperature oxide growth on chemically cleaned surfaces as well as treatments involving thermal, plasma and anodic oxidation have been employed with the aim of understanding the oxidation mechanism. The XPS technique was widely used for investigating the native oxides (a few tens of angstroms thick) and thick oxides on InP surfaces.

The observed chemical shifts in case of **In 4d** lines, due to the oxidation of the surface, are found to be small (0.3-0.4 eV) and the overlapping of O 2s and O 2p lines with **In 4d** core level makes the fitting procedure rather complicated. But, the **P 2p** lines present considerable advantage, since the chemical shifts in case of P-O bonds are well resolved (4-6 eV).

Systematic work was done by G. Hollinger et al. [73, 74, 75, 76]. Full investigation of the oxidation process starting from clean InP (110) surface until a non-reactive, well passivated with native oxides structure indicated a step process with intermediate phases [76]. A 1.4 eV oxygen-induced shift towards lower kinetic energy was observed after exposing the clean semiconductor surface to molecular oxygen ranged from 10^3 to 10^5L (1L=10^{-6} Torr s). For the exposure range 10^5L to 10^{12}L a broad feature centered at 4.7eV lower KE appeared indicating structural and chemical disordered in the oxide layer. A description based on a mixture of well defined compounds (e.g., In_2O_3+P_2O_5 or In_2O_3+$InPO_4$) seemed to be inadequate [77]. There were several chemical formula detected (e.g., $InPO_4$, $In(PO_3)_3$, P_2O_5, or InP_xO_y) and non stoichiometric compounds might occur. Surface reconstruction and sites having In:P ratio different than 1 could not be excluded.

Bertness [48, 78] concluded that oxygen chemisorption destroys long-range order on the surface. High resolution core-level spectra indicates large binding energy shifts attributed to direct oxygen bonding but also peaks with smaller shifts. The explanation for the last ones is the structural relaxation in response to oxidation of nearby atoms.

InP oxide structure changing along the thickness was reported by Losurdo [79]. He considered that the topmost layer is composed of $InPO_4$ and P-rich oxides (P_2O_5), whereas the In_2O_3 is mainly present at the interface with the InP substrate. From the previous assumptions, one may conclude that the InP native oxide is not chemically homogeneous along the overlayer thickness and the oxidation process is a complex one. In case of **P 2p** core level lines of phosphorus oxides, it is not easy to discriminate the amount of various compounds, such as $InPO_4$ (BE=134.1±0.2 eV), $InPO_3$ (BE=133.5±0.2 eV), $In(PO_3)_3$ (BE=133,7±0.2 eV) and P_2O_5 (135.6±0.2 eV) whose different contributions are responsible of the change in the shape of the oxidized **P 2p** core-level spectra. The bulk InP has the binding energy of BE=128.8 eV.

The InP bulk sample used for the previous investigation on (110) ***SCS*** of **In 4d** and **P 2p** core levels was removed from the UHV chamber and exposed to air for more than 24 hours.

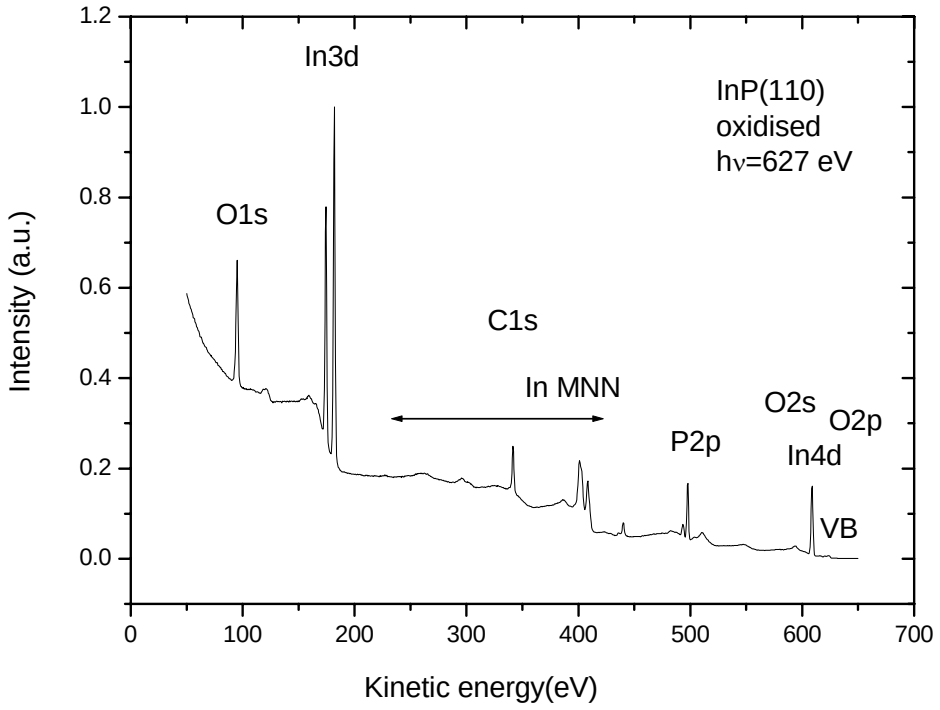

Figure 4.9. EDC spectrum for InP (110) surface after long term exposure to air. The presence of O 2s and O 2p lines make the fitting of In 4d lines difficult.

According to G. Hollinger [78] this exposure time is enough to obtain a well passivated, non-reactive surface. Now the EDC spectrum corresponding to an excitation energy of 627 eV reveals the presence of **C 1s** line and significant amount of oxygen (**O 1s).**

A detailed scan of **P 2p** core level spectrum recorded with excitation energy of 196 eV indicates significant contribution of the P-O bonds.

The value for the spin-orbit splitting 0.86 eV is similar with that one for clean InP (110) surface and the branching ratio 0.5 it is kept fix. The Lorentzian width value of 0.17±0.01 eV was used for all Voigt doublets. Good quality fits are possible with only 4 components. The $\mathbf{s_1}$ and **b** contributions with narrow width are assigned to P surface states (dangling bonds - DB) and P interior atoms respectively.

Important to notice is the positive shift of 0.730 eV for the ***SCS*** regarding the oxidized sample relative to the value of –0.307 eV obtained for clean InP (110) surface. And according to Bertness [78] this is more likely due to structural relaxation in response to oxidation of nearby atoms.

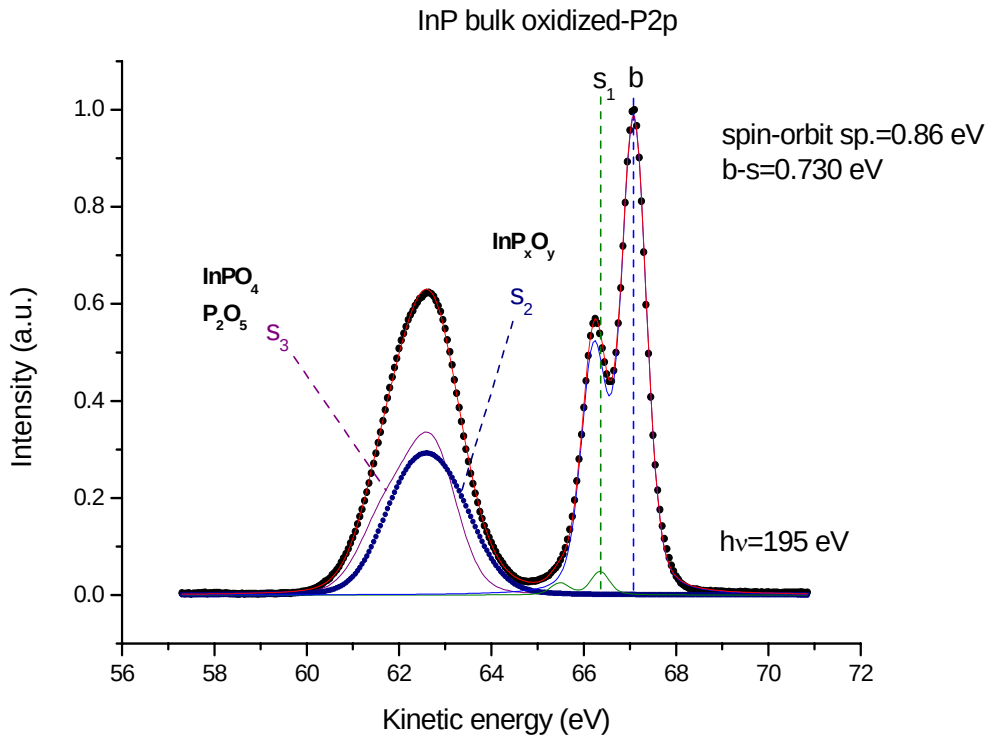

Figure 4.10. The **P 2p** core-level line for InP bulk oxidized (110) surface. The spin-orbit splitting is washed out for the $\mathbf{s_2}$ and $\mathbf{s_3}$ surface components reflecting the signal from native phosphorus oxides. The bulk **b** and the "clean" surface sites $\mathbf{s_1}$ contributions display a clearly resolved spin-orbit splitting

The peaks with large binding energy shifts relative to the bulk component **b** give the best correlation to a P-O bonding and both $\mathbf{s_2}$ and $\mathbf{s_3}$ contributions fill the required condition having chemical shifts in the 4-6 eV range. The oxidation process is a complex one. Conclusions on the degree of surface disorder may be drawn from the large broadening of the surface core-level components $\mathbf{s_2}$ and $\mathbf{s_3}$ (Gaussian width of 1.27 eV) relative to the core-level component associated with the bulk **b** atoms (Gaussian width of 0.52 eV). It is assigned that the $\mathbf{s_2}$ component represents InP_xO_y oxides that are rich in phosphorus (x>1) and have lower chemical shifts (see for example $In(PO_3)_3$ with a chemical shift of 4.9 eV). The chemical shift for the $\mathbf{s_3}$ surface component may indicate the presence of $InPO_4$ and P_2O_5 (chemical shifts of 5.3 and 6.8 eV, respectively) [79].

In spite of the large degree of structural disorder at the surface it is possible to give a general description of the chemical bonds that are present on the layer of native oxides for InP (110) surface.

4.3 Photoelectron spectra of InP nanocrystals

Most established surface science techniques are not able to spot the surface modification of the nanocrystals. This is either due to lack of long-range order for diffraction techniques or else due to the ligand coverage that would hinder probe microscopy in a surface investigation. Also the High Resolution TEM investigations do not reveal any clear surface detail.

A good choice for acquiring a qualitative understanding of the nanocrystal surface is the PES with synchrotron radiation and this technique was successful applied for previous nanostructure investigations [61, 80, 81].

Nanocrystals prepared by different treatments (eight samples) were investigated in order to understand the relationship between the photoluminescence (PL) quantum efficiency and the surface structure. All samples were deposited from toluene solution on Au films under N_2 atmosphere and transported to the experiment in sealed flasks. The samples were introduced via a fast entry lock into the UHV experimental chamber. Exposure to atmospheric pressure was less than 1 minute. The ligand shell provides sufficient protection against oxidation (see meth-wash sample) during the limited period of contact with air.

The kinetic energy recorded for **P 2p** and **In 3d** peaks is in the 40-650 eV range. Core-level spectra were fitted with the minimum number of Voigt doublet functions using a complex optimization routine follow by polynomial plus Shirley background subtraction [72]. The spin-orbit splitting value of 0.86±0.01 eV was used for all components in the **P 2p** spectra. This value is in agreement with similar data characterizing the spin-orbit spitting effect for InP bulk samples [70]. The Lorentzian broadening value of 0.17 eV provides good fits for all nanocrystals samples. A total instrumental resolution of 260 meV was used for recording high resolution photoelectron spectra of **P 2p** with 175 eV excitation energy. In the high excitation energy range the resolution was allowed to decrease slightly in order to ensure a high count rate in recording the **P 2p** and **In 3d** data.

It should be noted that during the measurements no radiation damage of the investigated nanoparticles has been observed.

4.3.1 InP as-prepared nanocrystals (“pure”samples)

The InP as-prepared nanoparticles are the samples resulting after the size selection procedure; no post-preparative treatments are done on them. The average size of the nanoparticles is assigned to be 3.4 nm with a particle size distribution of 8-10%. The PL efficiency is very low, <<1%. The EDC spectrum shown in **figure 4.11** is representative for all non-etched nanoparticles. Relative intensities

for **P** and **In** relevant peaks are significant reduced comparable with the similar contribution in case of InP(110) bulk surface. The most intense peaks originate from the TOP and TOPO ligands (**O 1s** and **C 1s**). There is also a significant signal from **silicon** and some traces of **chlorine**, due to the way of nanoparticle preparation. The presence of **Cl 3s** and **O 2s** peaks makes the **In 4d** peak difficult to fit. Therefore, the best choice for investigating InP nanocrystals is actually the **P 2p** core-level spectra.

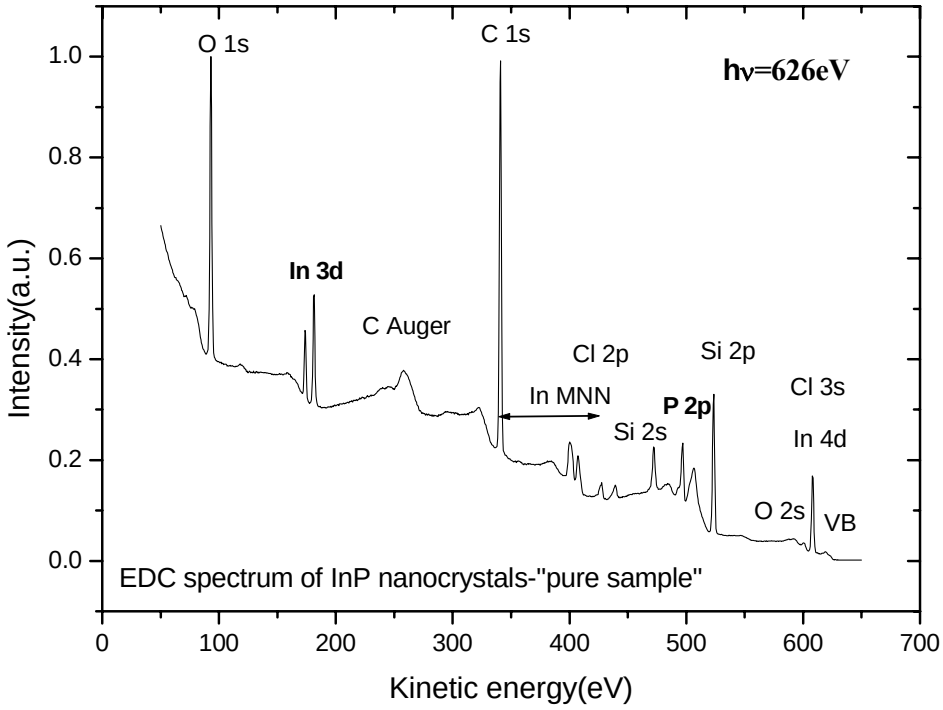

Figure 4.11. EDC spectra of as-prepared, size selected nanocrystals. The mean diameter for the nanocrystals is 3.4 nm. There is significant contribution of oxygen and carbon originating from the ligand shell.

From the way of preparing and manipulating the nanoparticles as well as by analyzing the previous survey spectrum (**figure 4.11**) one can imagine the possible chemical bonds at the nanocrystal surface - see **figure 4.12**.

Ligands like TOP molecules bound preferentially the indium atoms at the nanocrystal surface. Probability of TOP-phosphorous (P-P) bonds is negligible [65].

The TOPO ligands can bound (passivate) with high probability both In and P dangling bonds.

The nanoparticle surface might come in contact with *oxygen* during manipulation or transport to the experimental station. Oxygen is also expected to form bonds with In or P atoms at the nanoparticle surface.

The possibility of having unpassivated sites (In or P dangling bonds) at the nanocrystal surface cannot be excluded.

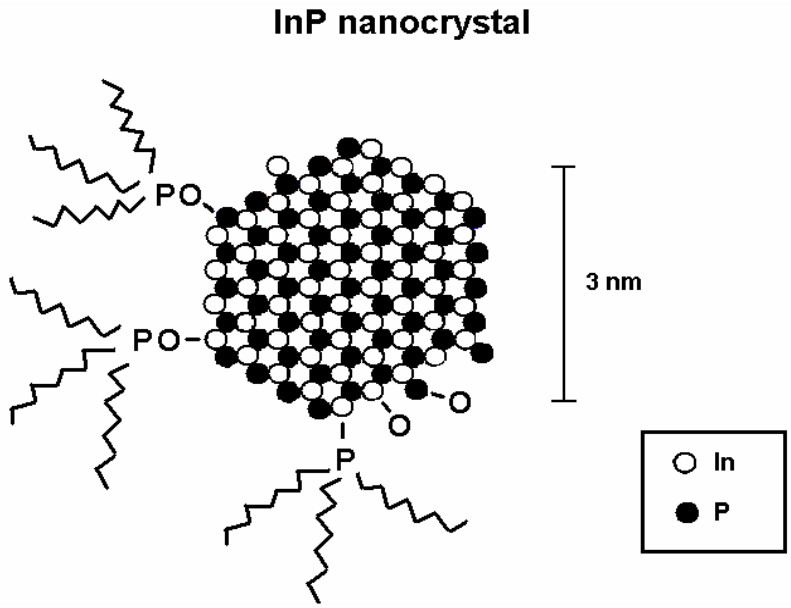

Figure 4.12. Representation of a 3nm diameter InP nanocrystal. Ligands like TOP-TOPO molecules or oxygen atoms may bind to the In or P atoms at the nanoparticle surface. There is also the probability of having dangling bonds (for both In and P atoms) at the nanocrystal surface.

Figure 4.13 a) shows **P 2p** core-level spectra recorded through a photon-energy range of 195.5-579.5 eV with normalized experimental intensities. Good data fits were possible only with *three* components for each spectrum with a Lorentzian broadening value of 0.17. Components $\mathbf{s_1}$ and $\mathbf{s_2}$ decrease in relative intensity as the excitation photon energy and subsequence the kinetic energy for photoelectrons increase. These components are, therefore, identified with atoms having a distinct surface environment in the nanocrystal and the component **b** is due to P atoms in the interior of the nanocrystal volume. Spin-orbit splitting is well resolved in the case of the bulk component **b**, indicating a high degree of crystallinity inside the nanoparticles and relatively broad surface core-level components $\mathbf{s_1}$ and $\mathbf{s_2}$ are evidence for a large degree of bond length and angle variation at the surface. In this size range up to 30% of the nanocrystal atoms are located on the surface.

Component $\mathbf{s_1}$ is shifted by an average value of 1.41 eV to lower kinetic energy with respect to the bulk component **b**; it reflects the signal from TOP phosphorus atoms bound to In atoms at the nanoparticle surface. P dangling bonds located at the nanocrystal surface can also contribute to the $\mathbf{s_1}$ signal.

The **P 2p** $\mathbf{s_2}$ component is assigned to come from P-O bonds, if one considers the way of preparing the sample and the large chemical shift relative to the volume component **b** [82]. An average shift of 3.72 eV relative to the bulk component originates from the phosphorus atoms in TOPO used during the preparation process.

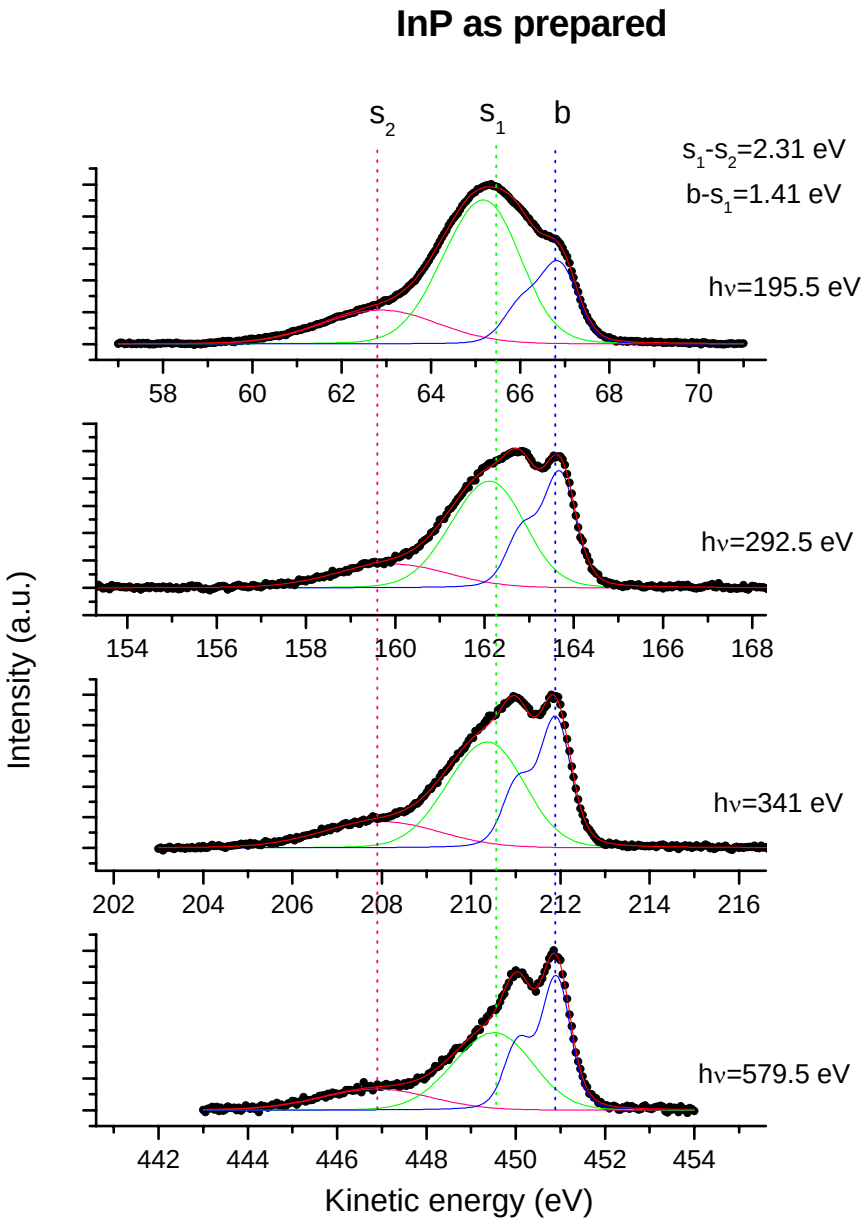

Figure 4.13 a). **P 2p** core-level photoemission spectra of as prepared nanoparticles. Component **b** is due to atoms in the volume of nanocrystals and $\mathbf{s_1}$ and $\mathbf{s_2}$ are due to surface sites.

Previous studies on bulk InP (110) surfaces showed a rather complicate oxidation process with different chemical structures for phosphorus oxides [73-79]. Signal from accidental oxidation of P dangling bonds during the sample manipulation and transfer in the UHV chamber (up to 2 min.) might also contribute to the $\mathbf{s_2}$ component [79].

The ratios of bulk **b** to surface component $\mathbf{s_1}$ and $\mathbf{s_2}$ for different excitation energies are presented in **figure 4.13 b**). The ratios increase with increasing excitation energy.

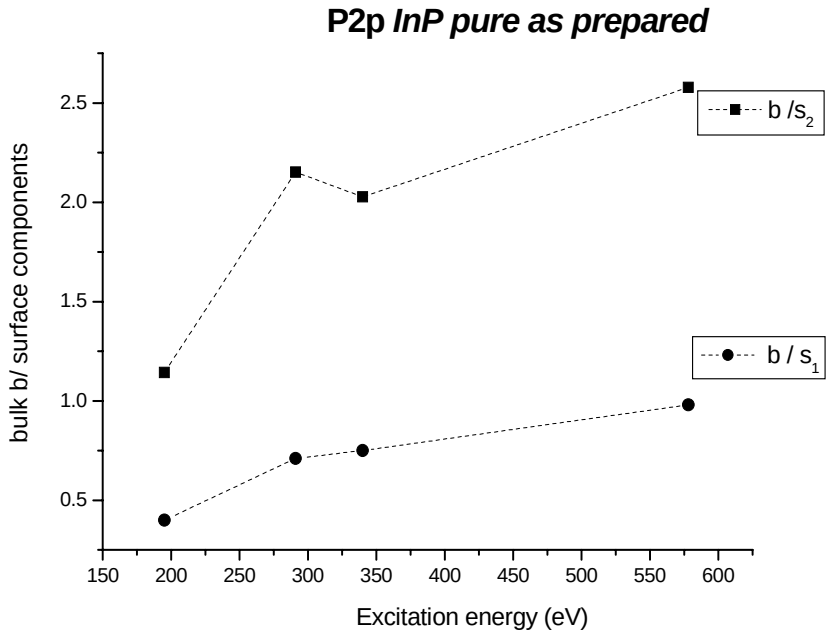

Figure 4.13 b). Energy dependent $\mathbf{b / s_1}$ and $\mathbf{b / s_1}$ ratios for the pure sample. Dashed lines are for eye guidance.

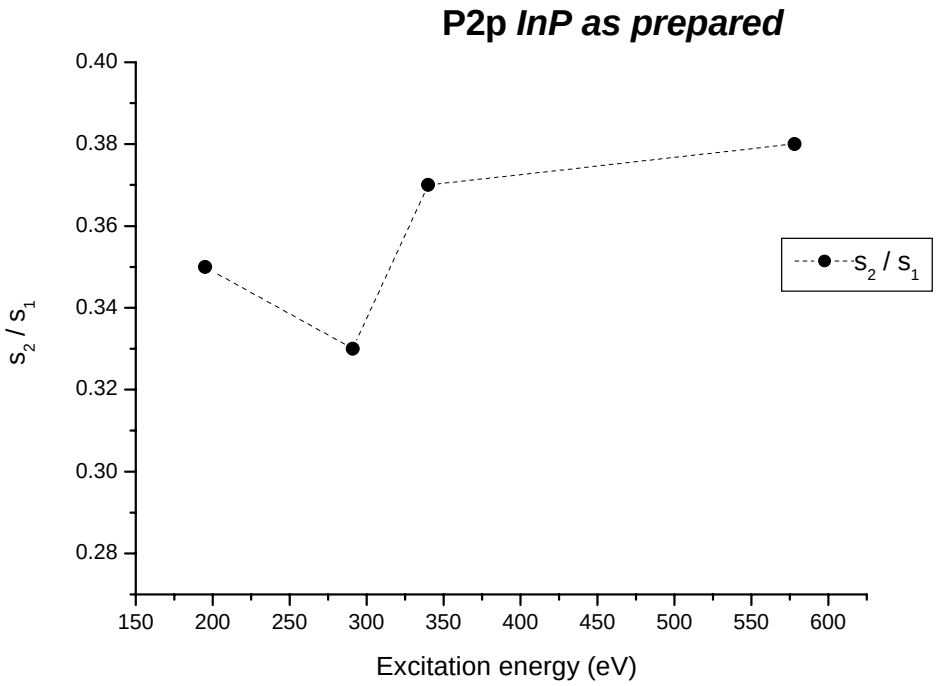

Figure 4.13 c). The $\mathbf{s_2 / s_1}$ ratios for the surface species are less sensitive on the excitation energies. The dashed line is for eye guidance.

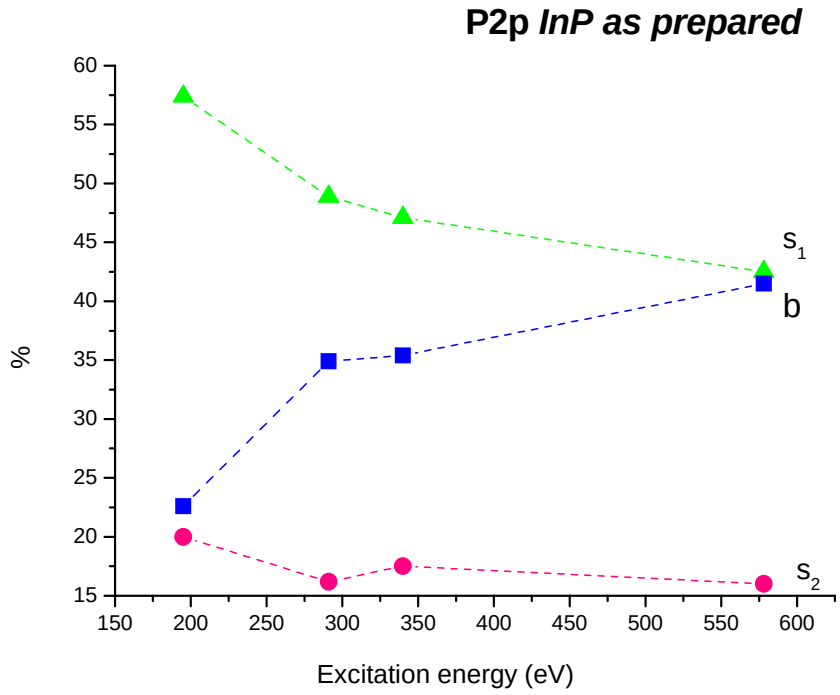

Figure 4.13 d). Contributions (%) for bulk **b** and surface species $\mathbf{s_1}$ and $\mathbf{s_2}$ are plotted. The dashed lines are for eye guidance.

The surface contribution $\mathbf{s_2}$ / $\mathbf{s_1}$ ratio is less sensitive when changes of the radiation energy occur. This means that the depth sensitivities for both species are very similar and two shells structure for the ligands is excluded (**figure 4.13 c**).

As we will see, the $\mathbf{s_2}$ / $\mathbf{s_1}$ ratio is directly linked to the PL quantum efficiency and it will be displayed for all samples.

Figure 4.13 d) displays the contribution from bulk and surface components. As mentioned before, the bulk **b** contribution has a direct response with the increase of the excitation energy.

The assumption that phosphorus from TOPO contributes to $\mathbf{s_2}$ surface component and phosphorous from TOP ligands contributes to $\mathbf{s_1}$ surface component and the 2.41 eV value for the chemical shift is strongly supported by the results of Borchert et al. [80]. Their investigation on CdSe/ZnS core-shell nanocrystals also capped with TOP-TOPO ligands revealed a chemical shift between the TOP and TOPO **P 2p** signal of about 2.62 eV-see **figure 4.14**. The only difference is that while in the present case the phosphorus atom of the TOP molecules bounds an In atom, for the core-shell system the TOP molecules bounds Zn dangling bonds.

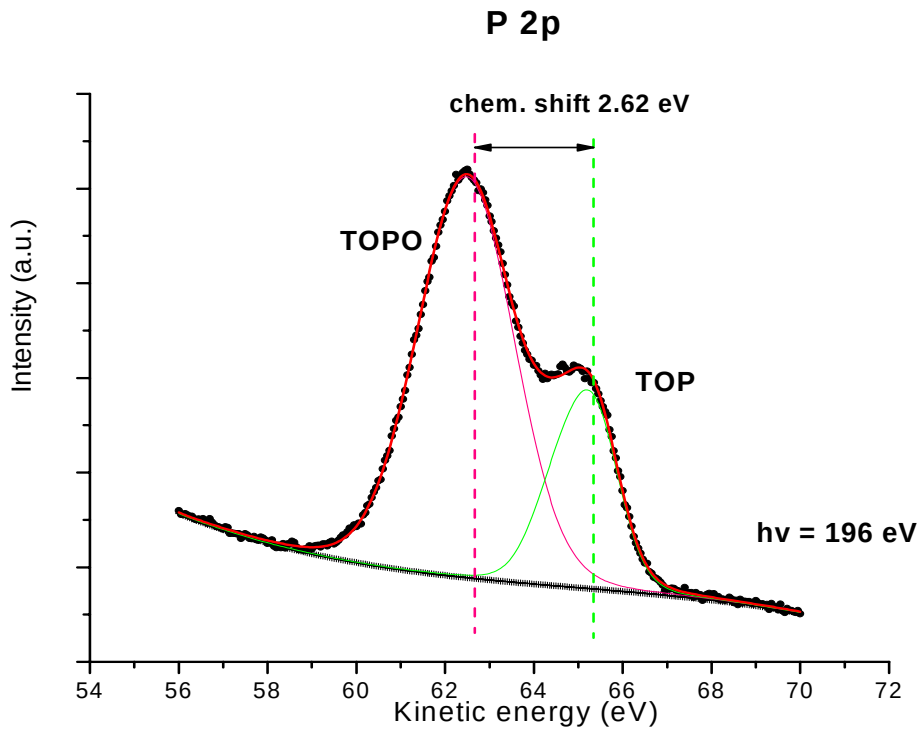

Figure 4.14. **P 2p** spectrum of the TOP-TOPO ligands at the CdSe/ZnS core-shell nanocrystal surface. The two components assigned to phosphorus atoms from TOP and TOPO molecules are separated by a chemical shift of ~2.62 eV. Modified from [80].

Size dependent spectra recorded with the same excitation energy, **hv=292.5 eV** are display in **figure 4.15**. Additional to the previous 3.40 nm average diameter nanocrystals smaller (2.75 nm) and larger (3.85 nm) ones are investigated. All *three* samples originate from the same crude solution and are the result of size selection technique previous described. As expected, the broadening of the bulk signal and the total contribution of the surface species increases with decreasing the particle size. Also the intensity of the surface components $\mathbf{s_2}$ and $\mathbf{s_1}$ for the smallest sample (2.75 nm) is significantly enhanced with respect to the volume component.

A natural question is why there is a large difference of $\mathbf{s_2}$ / $\mathbf{s_1}$ ratio for samples with average sizes distribution smaller or larger than 3.40 nm diameter sample. One answer could be different amount of ligands (TOP/TOPO) used during preparation of the nanocrystals. Strong signal for the $\mathbf{s_2}$ surface component could also originate from excess TOPO molecules. Significant oxidation could also occur during the transport of the flask to the experiment in case of accidental exposure of the samples to air and the result is significant enhancement of the $\mathbf{s_2}$ contribution.

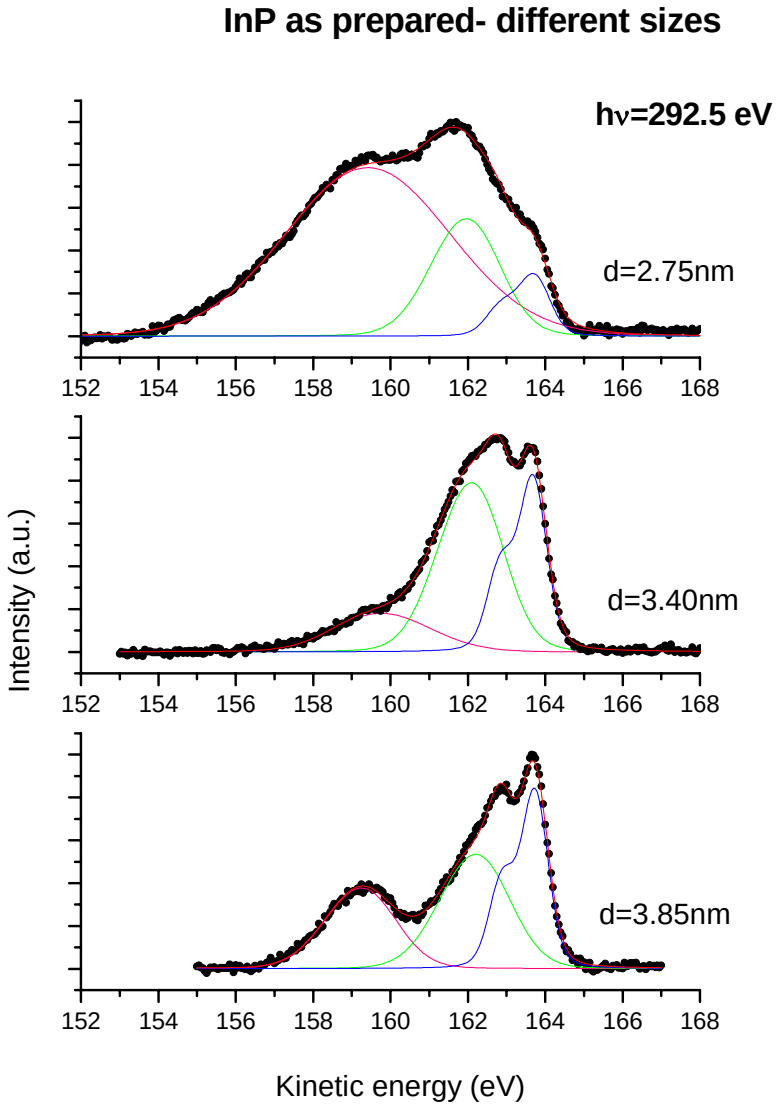

Figure 4.15. Size dependent photoemission spectra (**P 2p** line) of InP as prepared nanocrystals

4.3.2 InP methanol washed

In order to answer the previous questions a new 4.2 nm average diameter sample was prepared. So called InP methwash is the result of washing twice the ”pure” InP nanocrystals with a solution of toluene:methanol (1:5). The aim of this treatment was to remove the undesirable reaction products that can appear during the nanoparticle synthesis. This washing procedure was applied to all the samples investigated in this work except the as-prepared (previously discussed) and the under nitrogen etched samples (see section 4.3.5).

Fitting procedures reveal a picture similar to the previous investigations. There are two surface components **s_1** and **s_2** and a volume component **b**. The chemical shifts with respect to the bulk signal are 1.11 eV and 2.61 eV for surface component s_1 and s_2 respectively.

Now, the contribution of the surface species is significantly reduced and this result cannot be explained solely by the increase in diameter for our new sample (4.2 nm instead 3.4 nm in previous case). It seems that the washing procedure is very efficient in removing the excess of TOP-TOPO molecules (ligands); another direct conclusion is that previous samples had excess of TOP-TOPO ligands.

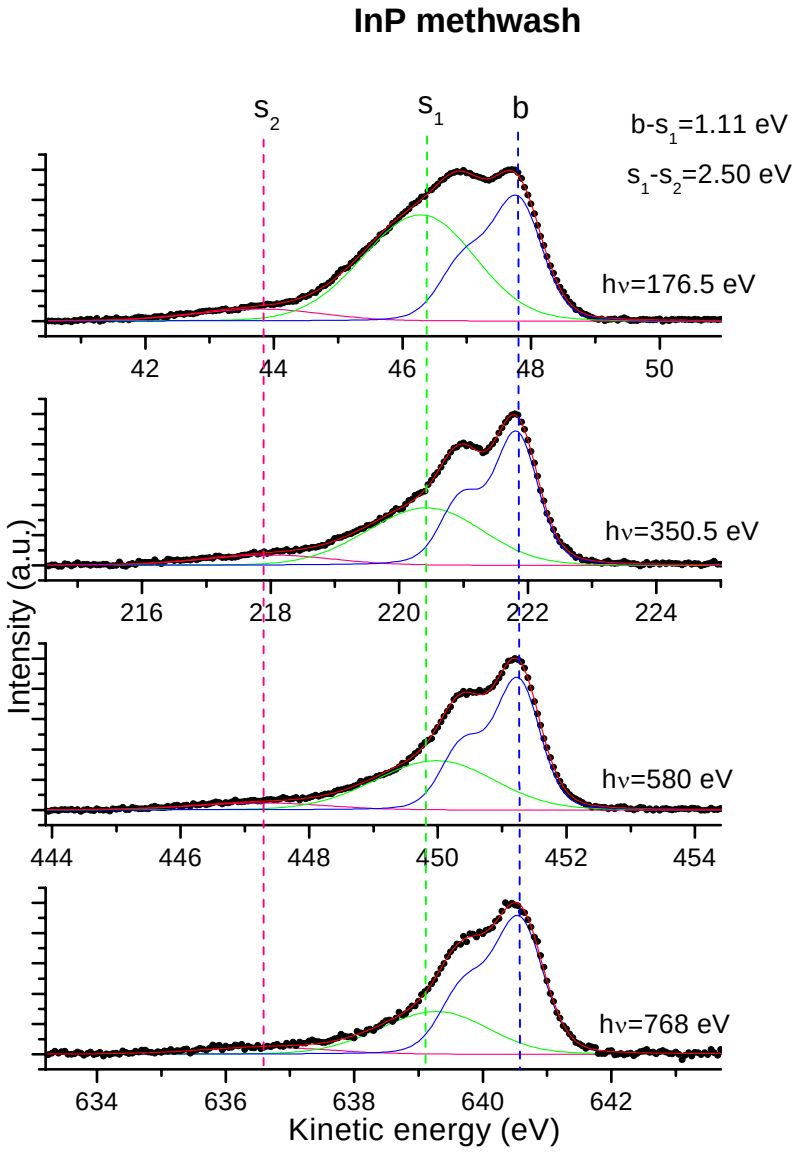

Fig. 4.16 a). **P 2p** core-level photoemission spectra of 4.2 nm mean diameter crystals. Component **b** is due to atoms in the volume of nanocrystals and **s_1** and **s_2** are due to surface sites. The methanol washing procedure significantly reduced the signal from surface atoms.

Another important aspect is the reduced intensity for the oxide s_2 signal, a clear sign that the surface oxidation during the sample transport and transfer in the UHV chamber is rather low (see **figure 4.16 b**).

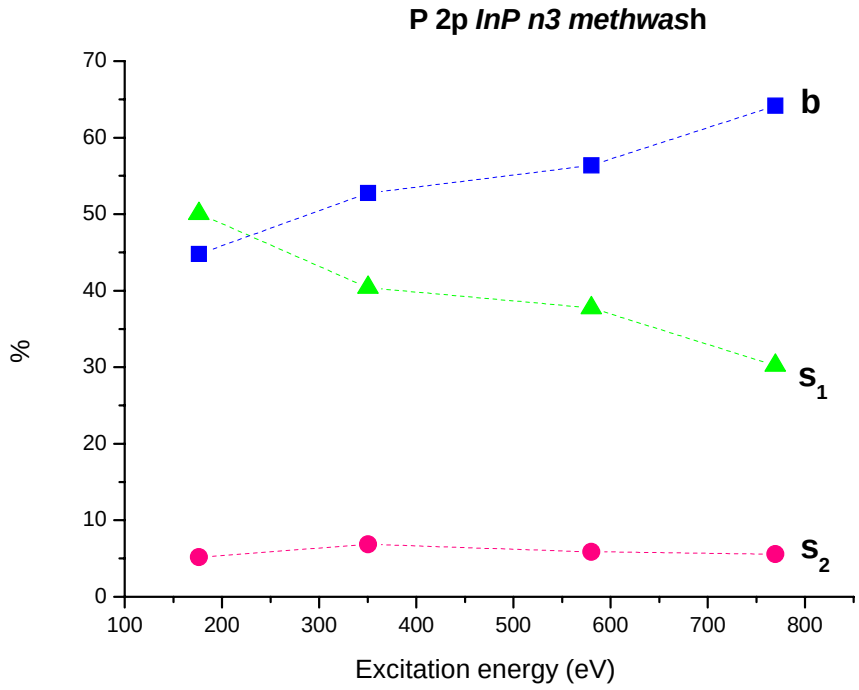

Figure 4.16 b). Energy dependent contributions (%) for bulk and surface components. The signal from surface species, particularly s_2, is significant reduced comparative to as prepared sample. The dashed lines are for eye guidance.

4.3.3 InP pyridine

Another important aspect that has to be cleared is the contribution of P dangling bonds at the **P 2p** core level lines. This can be done-as we will see below-by studying nanocrystals that are capped with pyridine.

Unfortunately, InP nanocrystals with no TOP-TOPO ligands bound to the surface are impossible to prepare because such molecules are needed as stabilizing agents during the preparation process. Also the nanoparticles have to be covered with ligands in order to prevent coagulation and one should find an appropriate post preparative treatment to avoid that.

The appropriate solution is washing with pyridine of the as prepared InP nanocrystals. Pyridine, an aromatic heterocyclic compound is analogous to benzene but with one of the C-H units replaced by a

nitrogen atom. In pyridine, the nitrogen atom has a lone pair of electrons in one of the sp^2 hybridized orbitals.

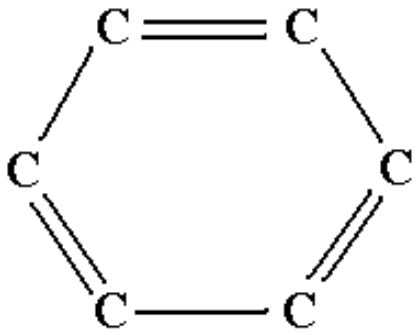

Figure 4.17. Schematic representation of a pyridine molecule. One carbon atom of a benzene cycle is replace by a nitrogen atom.

The pyridine has the capability to replace up to 90% of the TOP-TOPO ligands [65]. The surface of the nanocrystal is now passivated by shell of pyridine and the new ligand offers sufficient protection against coagulation or extensive oxidation. Then, the pyridine molecules are easily detached once the nanoparticles are placed under vacuum.

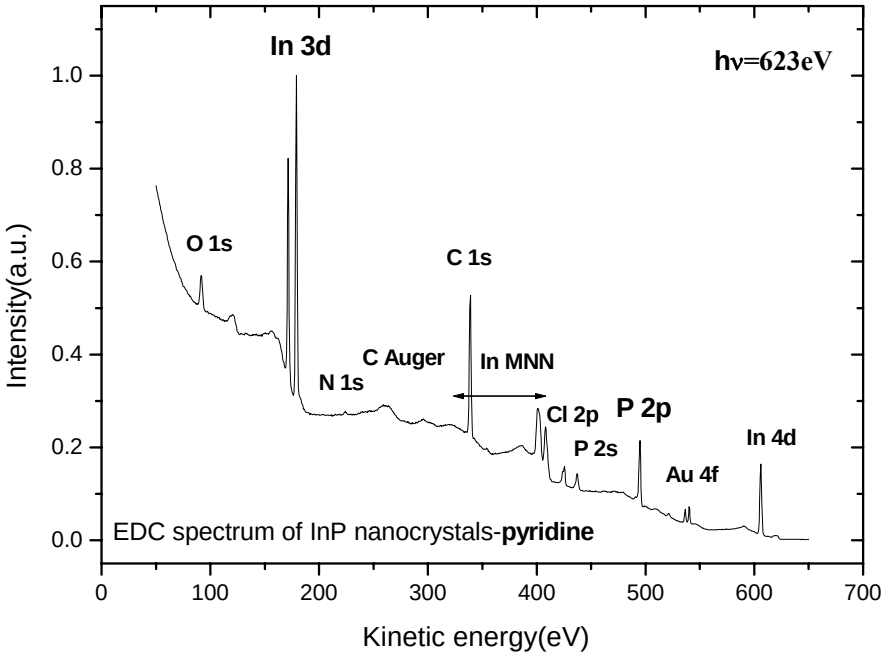

Figure 4.18. EDC spectra of pyridine capped nanocrystals with a mean diameter of 4.2 nm. The nitrogen signal from N 1s core-level line is very low.

The investigated sample consists of size selected nanocrystals with an average diameter of 4.2 nm that were capped with pyridine. As expected, there is no improvement of the photoluminescence efficiency (<<1%).

The EDC spectrum reveals enhanced signal for In and P core levels and reduced intensity for O 1s and C 1s peaks. The reason for this situation is the capability of the pyridine to remove large amount of TOP-TOPO ligands from the nanocrystals surface. Since the pyridine molecules evaporate once the sample is place under vacuum, low signal from the N 1s line can be expected. Indeed, the survey spectrum displays low signal from nitrogen atoms. This treatment also reduces efficiently the silicon contamination.

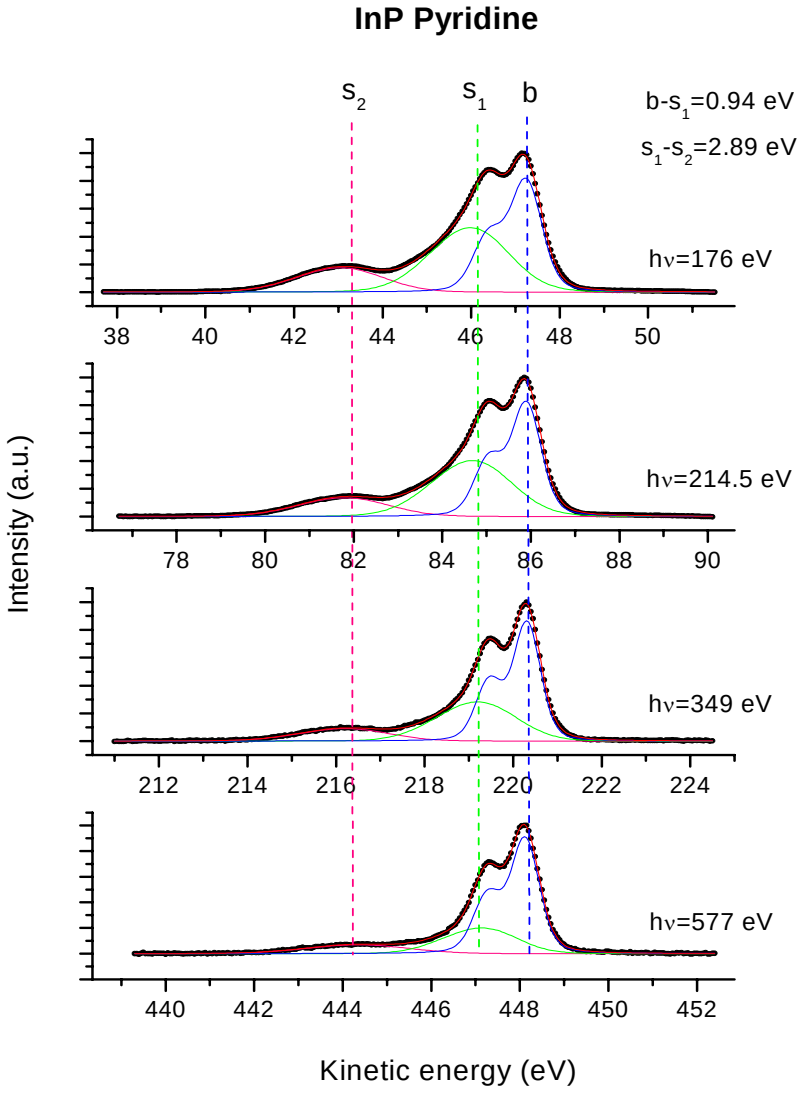

Figure 4.19 a). **P 2p** core-level photoemission spectra of 4.2 nm mean diameter crystals. Component **b** is due to atoms in the volume of nanocrystals and $\mathbf{s_1}$ and $\mathbf{s_2}$ are surface core-level shifts. The spin-orbit splitting is well resolved in case of volume component v that displays also an increase in intensity relative to the surface species.

All energy dependent spectra are well fitted with only three components. The explanations for **b** and $\mathbf{s_2}$ core level lines are similar with the previous investigation, i.e., volume atoms and P-O bonds, respectively. Now the surface $\mathbf{s_1}$ component reflects mainly the signal from P dangling bonds (DBs) resulting after the ligands extinction. The bulk component **b** has a clearly resolved spin orbit splitting due to the high crystalinity of the nanoparticles.

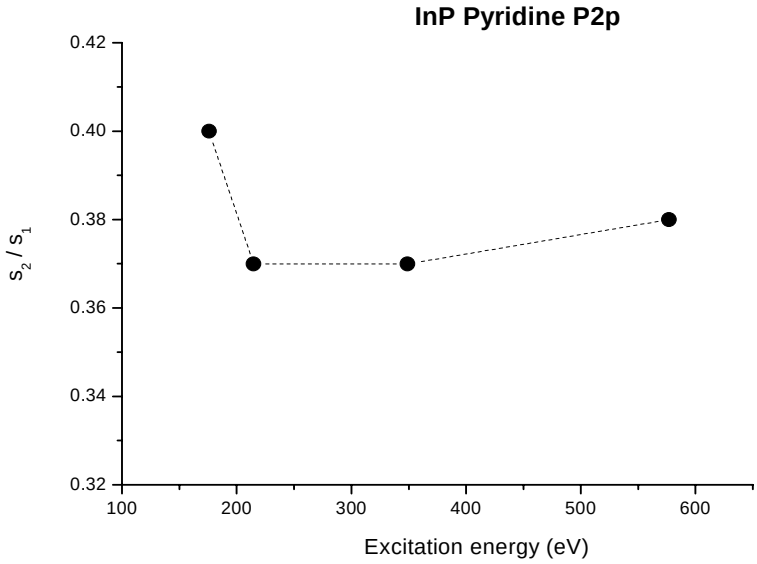

Figure 4.19 b). The $\mathbf{s_2}$ / $\mathbf{s_1}$ ratios for the pyridine sample. The dashed line is meant to guide the eye.

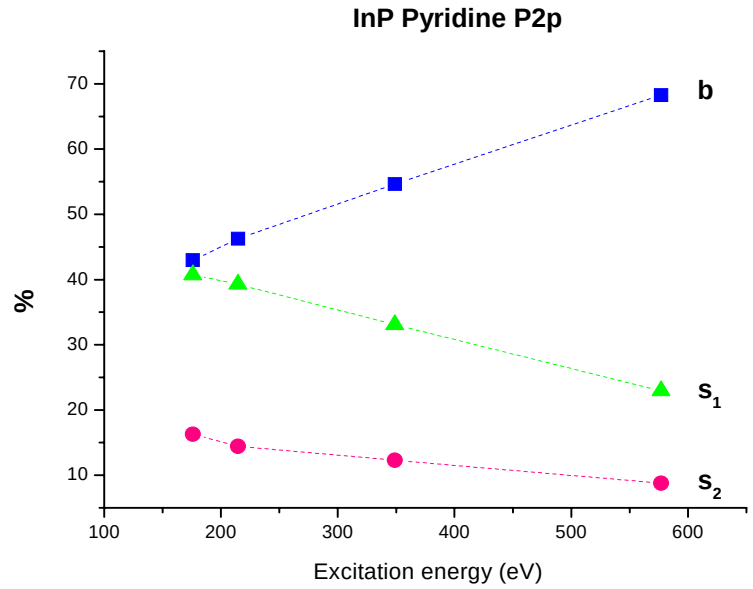

Figure 4.19 c). Energy dependent contributions (%) for bulk and surface components-pyridine capped sample. The dashed lines are for eye guidance.

The volume contribution (%) is slightly increasing (10-15%) with respect to the value of the methwash sample (**figure 4.19 c**) and also the $\mathbf{s_2}$ / $\mathbf{s_1}$ ratio is significantly enhanced (**figure 4.19 b**). The lack of ligands combined with exposure to oxygen during the sample transport and transfer in the UHV chamber favors the P-O bonds ($\mathbf{s_2}$ line is enhanced).

The conclusion of the InP pyridine sample investigation is that P DBs contributes to the $\mathbf{s_1}$ surface component of all InP nanocrystal samples.

4.3.4 InP oxidized sample

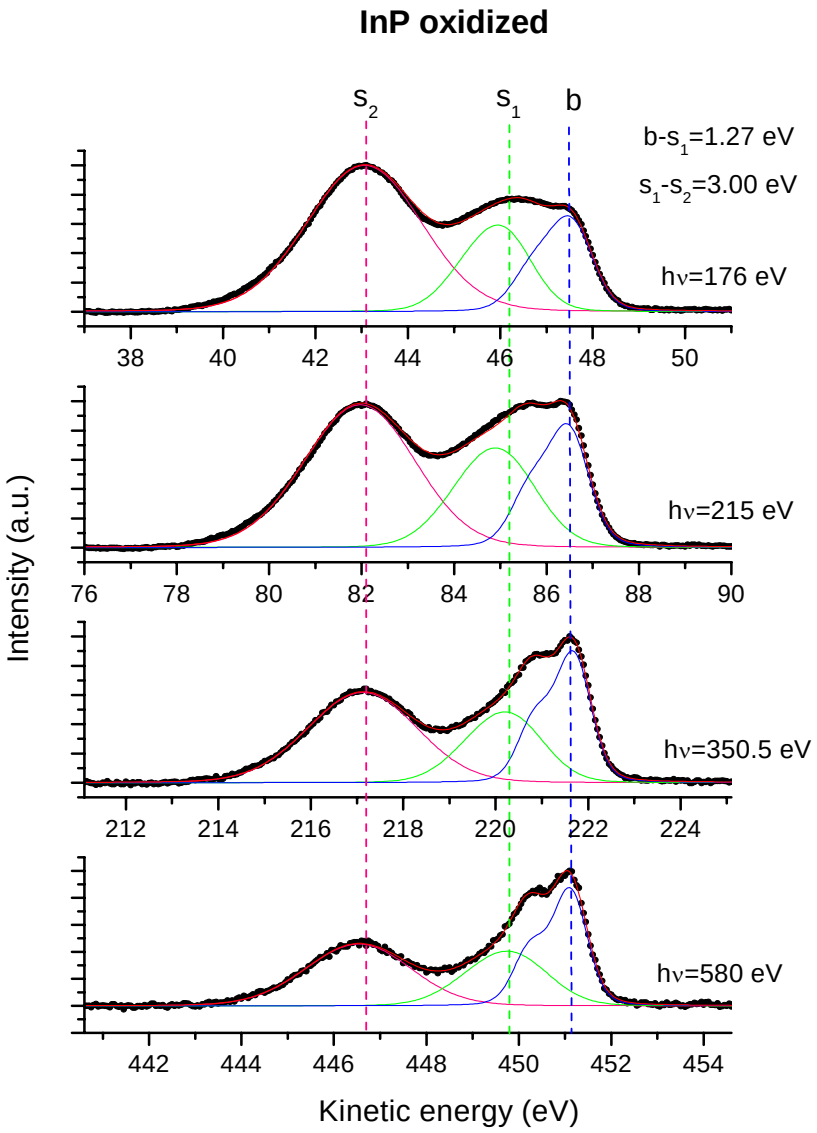

Figure 4.20 a). **P 2p** core-level lines of 4.2 nm oxidized sample. The surface s_2 component due to P-O bonds is now significantly enhanced due to long exposure to air.

Exposure to air and light for many hours leads to an oxidized InP sample. The PL efficiency was slightly increased but luminescence yield is still low, less than 0.1%.

The average size for the nanoparticles is about 4.2 nm. Dramatic changes of the nanocrystal surface occur after exposure to oxygen. **Figure 4.20 a)** presents a significant increase in intensity for the surface component $\mathbf{s_2}$ relative to $\mathbf{s_1}$.

There is also a slight increase of the chemical shifts for the surface species. An average of 1.27 eV and 4.27 eV chemical shift relative to the bulk component for the $\mathbf{s_1}$ and $\mathbf{s_2}$ peaks respectively resulted after the fitting procedure. One explanation for the higher shift in binding energy in case of the $\mathbf{s_2}$ contribution is the strong oxidation process resulting after long exposure to air and light (more than 24h). New P-O bonds with higher binding energy result after the surface reconstruction and P dangling bonds are reduced (passivated) causing also a shift towards lower kinetic energy for surface component $\mathbf{s_1}$. The main contribution to the $\mathbf{s_1}$ signal comes from the phosphorous atoms of TOP molecules that are bound the In surface atoms.

The values of the s_2/s_1 ratios are plotted in **figure 4.20 b)**. There is a weak energy dependence of the s_2/s_1 ratios.

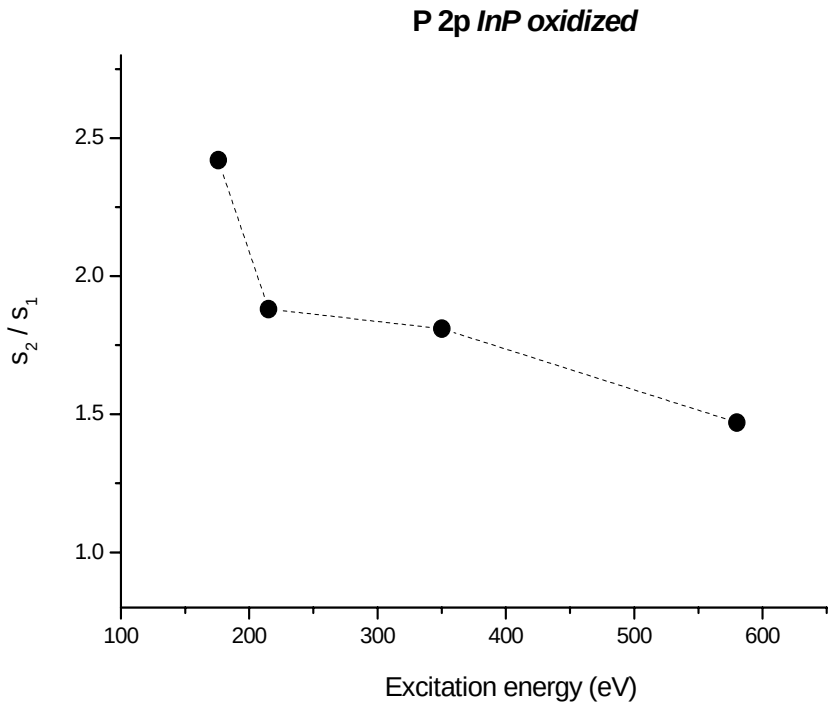

Figure 4.20 b). The $\mathbf{s_2}$ / $\mathbf{s_1}$ ratios for the oxidized sample. The dashed line is meant to guide the eye.

Figure 4.20 c) reveals a surface component $\mathbf{s_2}$ having the dominating contribution in the surface sensitive regime.

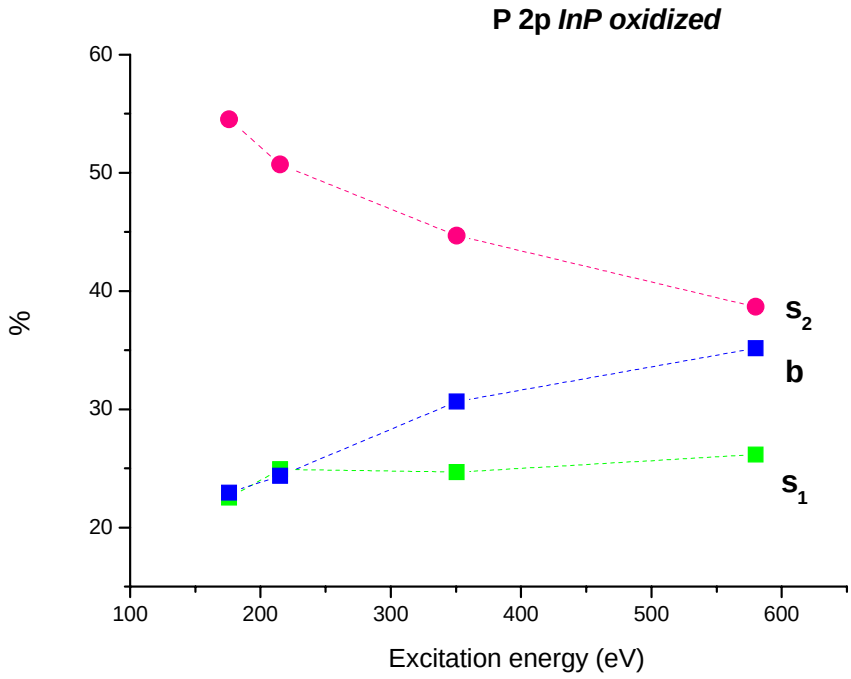

Figure 4.20 c). Energy dependent contributions (%) for bulk and surface components, 4.2 nm oxidized sample. The dashed lines are for eye guidance.

4.3.5 InP nanocrystals HF etched under nitrogen atmosphere

As part of the pioneering work on synthesis of InP nanocrystals, Micic et al. proposed also post-preparative treatments to improve the properties of the nanoscale particles. A successful way to improve the photoluminescence of the InP nanocrystals proved to be the treatment with HF solution of the nanoparticle surface [83]. However this procedure is rather not reproducible with respect to the resulting photoluminescence and there is no clear picture of the modifications of the nanocrystal surface due to the etching mechanism (which is not completely understood).

A systematic study of the HF etching mechanism is required and this is done in the present investigation. For all etched samples the exposure to HF is performed in presence of light and significant amount of TOPO molecules (excess).
Size selected nanoparticles (3.6 nm average diameter) were HF etched under light exposure (450 W xenon lamp passed through a long pass filter with the cut-off wavelength depending on the particle size-see ref. 65) and oxygen free atmosphere (**nitrogen**) and the result is the "InP HF-nitrogen light" sample. The photoluminescence quantum efficiency increases significantly (1-5%).

Figure 4.21 a) presents the **P 2p** core-level spectra after the etching procedure with HF solution. In addition to surface components $\mathbf{s_1}$ and $\mathbf{s_2}$ discussed before, a new feature, the $\mathbf{s_3}$ component appears. The $\mathbf{s_3}$ with its large chemical shift indicates the presence of F atoms on the nanocrystal surface [82]. The quality of the fitting procedure is significantly improved when the third surface component $\mathbf{s_3}$ is present. Also the EDC spectra display a clear F 1s line (not shown here).

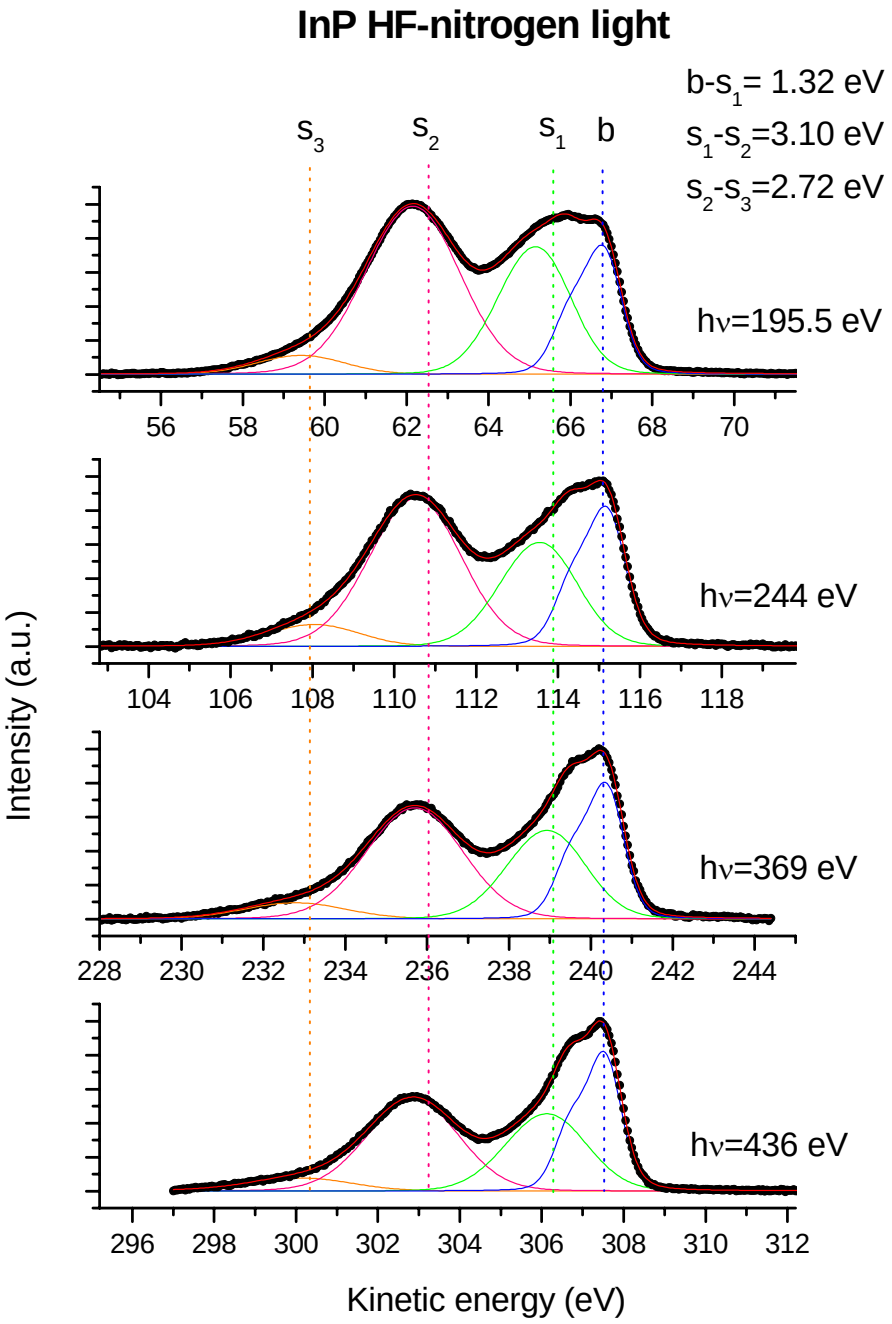

Figure 4.21 a). **P 2p** energy dependent spectra of 3.6 nm etched under nitrogen InP nanoparticles. In case of InP HF-nitrogen light sample. There is evidence for a third surface component $\mathbf{s_3}$ due to the etching treatment.

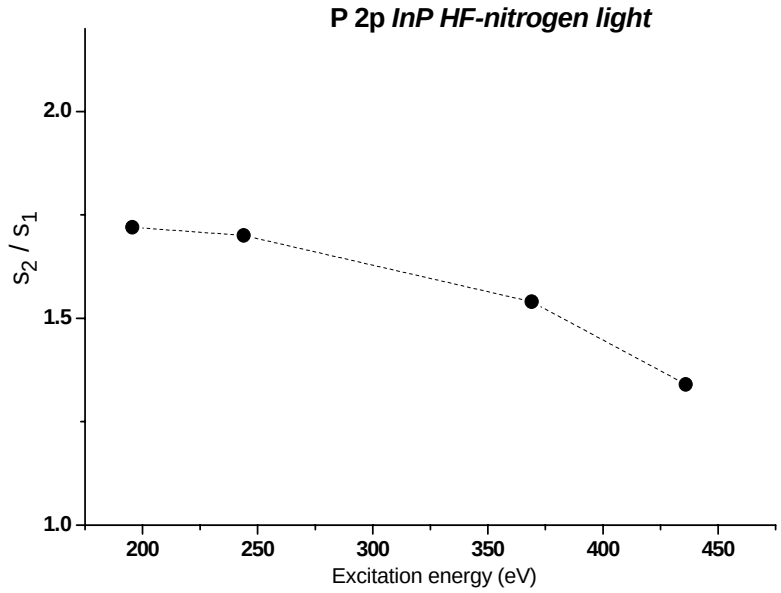

Figure 4.21 b). The s_2 / s_1 ratios for the oxidized sample. The dashed line is for eye guidance.

There are additional changes in relative intensity for the other two surface contributions, increasing and decreasing for s_2 and s_1 respectively (**figure 4.21 b**). It might be possible that HF removes P atoms with surface dangling bonds that are not well passivated with organic ligands. Once such atoms are removed, the remaining site, rich in In, can be capped with TOPO ligands and also with fluorine. Better surface passivation results in the observed increase of the photoluminescence quantum yield.

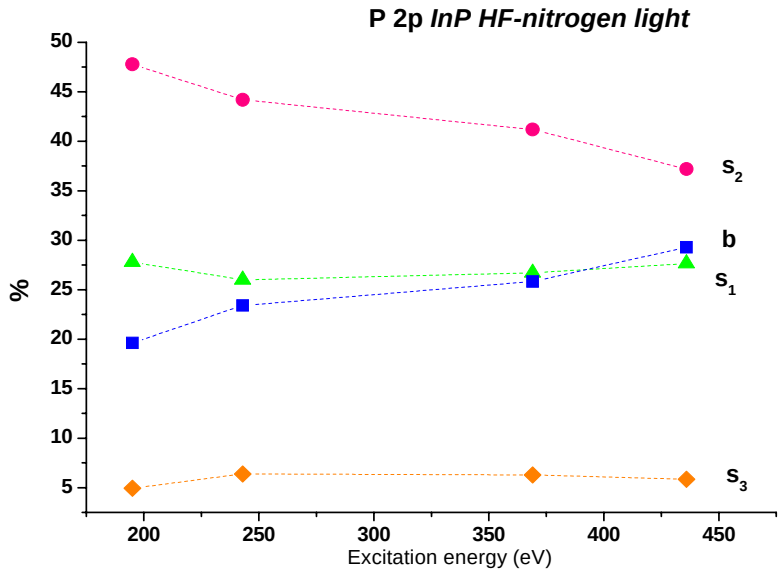

Figure 4.21 c). Energy dependent contributions (%) for bulk and surface components, 3.6 nm HF etched under nitrogen sample. The dashed lines are for eye guidance.

The **figure 4.21 c)** indicates that P-F bonds are present with a contribution of more than 5% at the measured spectra.

4.3.6 Highly luminescent InP etched nanocrystals

For all previous samples the room temperature quantum efficiency was very low, <<1% for the non-etched samples and up to 5% for the "InP HF-nitrogen light nanocrystals". This is presumably the result of non-adequate passivation of the nanocrystal surface. The dangling bonds may act as traps for the photogenerated carriers and can provide non-radiative recombination pathways.
Post-preparative modifications of the particle surface provide a way to eliminate those undesirable trap sites. A recent method implying the treatment of InP nanocrystals with HF solution in presence of **oxygen** and **light** results in a strong band edge luminescence (20% quantum efficiency). The EDC spectrum (**figure 4.22**) is representative of all etched samples and F 1s line is clearly visible.

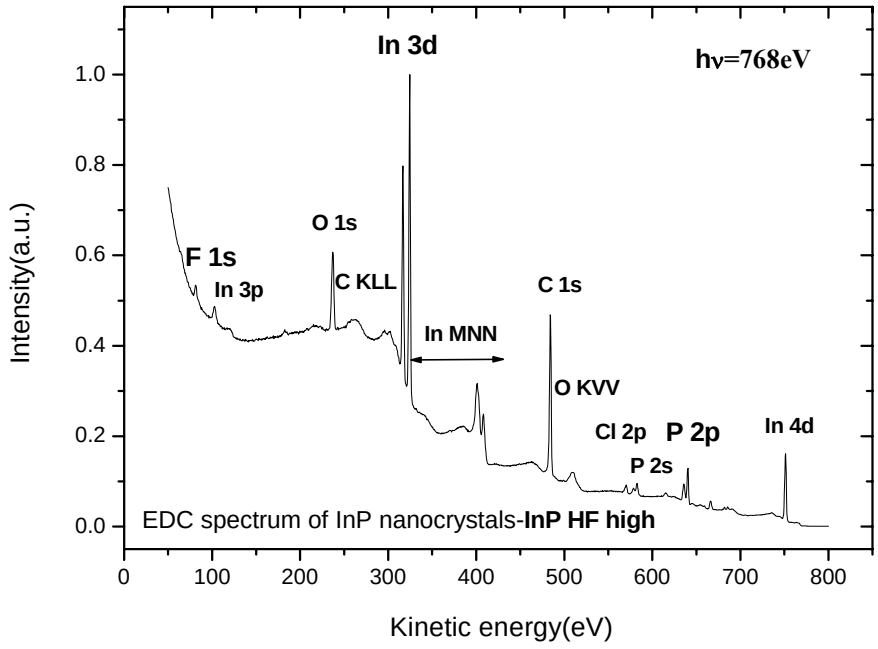

Figure 4.22. The EDC spectrum of InP etched under air nanocrystals recorded with an excitation energy hν=768 eV. The F 1s core level line due to HF treatment is clearly visible.

Figure 4.23 a) presents the **P 2p** core-level spectra after the etching procedure with solution of HF.

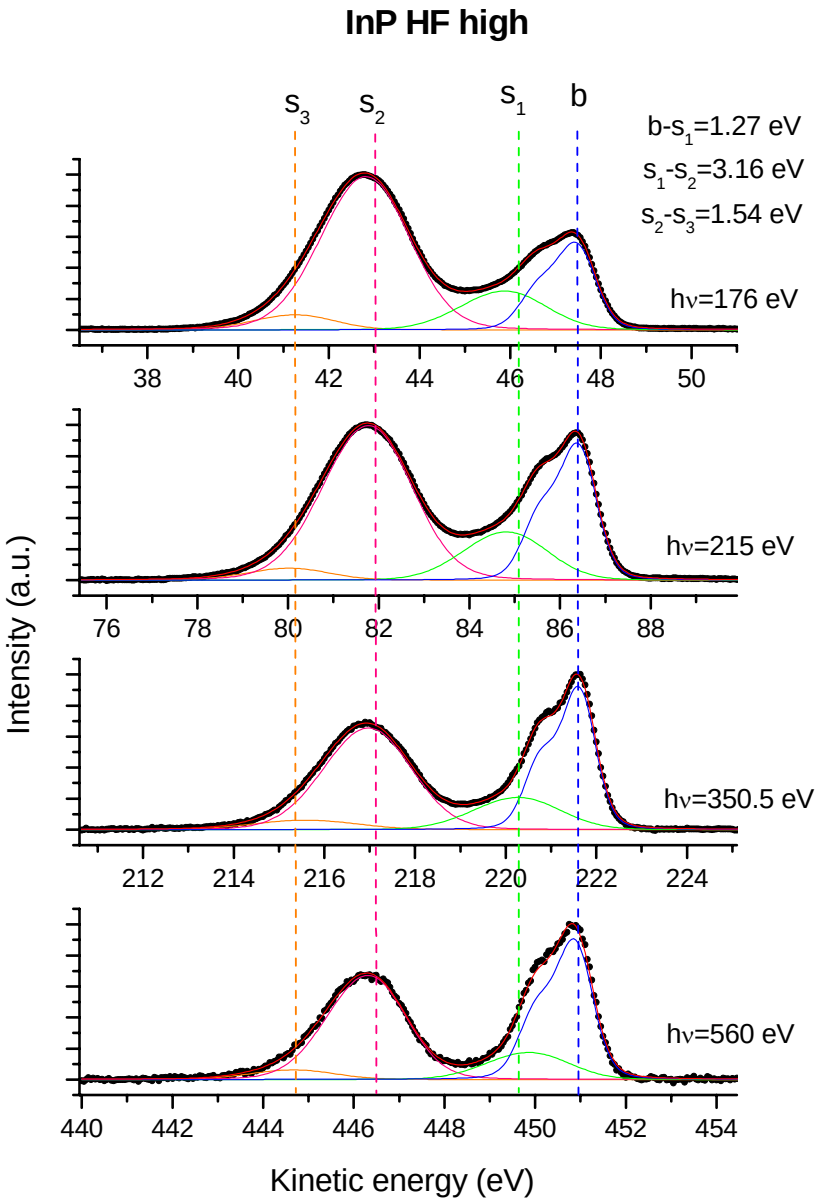

Figure 4.23 a). Energy dependent spectra for the highly luminescent sample, d=4.1 nm. The **P 2p** lines are well fitted with four components. The surface $\mathbf{s_1}$ contribution assigned to non-passivated sites has decreased in intensity.

All energy dependent spectra are well fit with four components, one volume **b** and three surface contributions. Surface $\mathbf{s_1}$ component representing signal from dangling bonds and possible phosphorus TOP molecules is now significant reduced with respect to the $\mathbf{s_2}$ signal that corresponds to phosphorus oxides (**figure 4.23 b**). Similar to InP etched under nitrogen sample, the $\mathbf{s_3}$ surface component originates from P-F bonds but the signal intensity (**figure 4.23 c**) and the chemical shift are significantly reduced now.

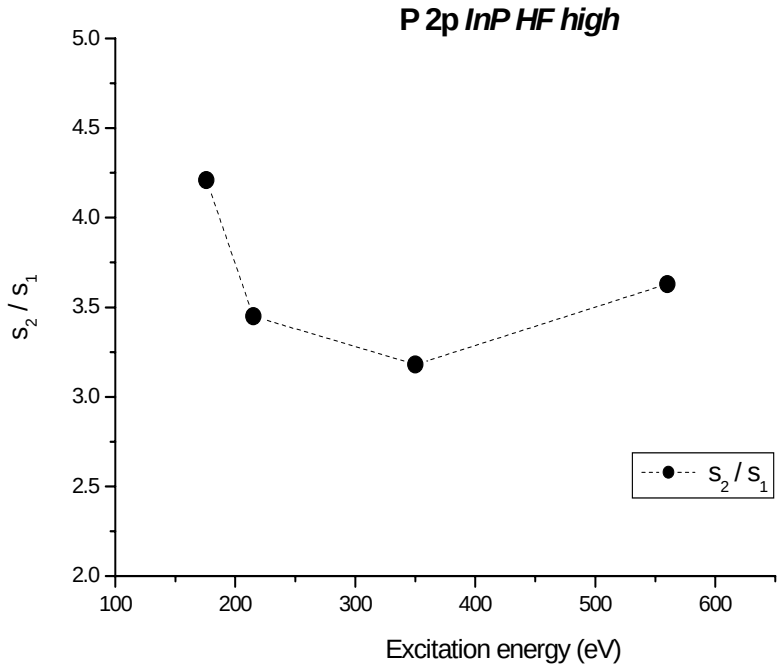

Figure 4.23 b). The s_2 / s_1 ratios for the highly luminescent sample. The dashed line is shown for eye guidance.

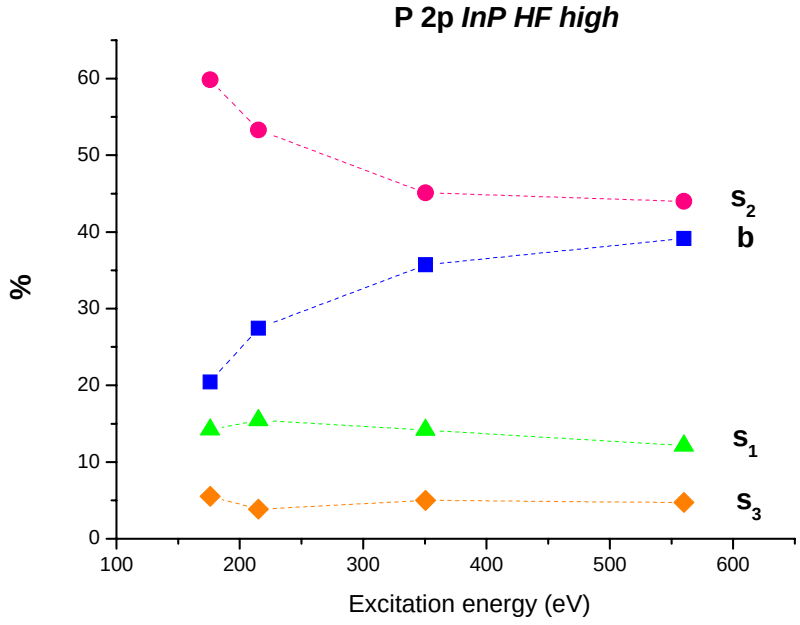

Figure 4.23 c). Energy dependent contributions (%) for bulk and surface components, 4.2 nm HF etched under air sample. The surface s_3 signal is reduced relative to the one of HF under nitrogen sample. The dashed lines are shown for eye guidance.

4.3.7 TOPO capped sample

An important question is if the InP nanocrystals capped with only one type of ligands (TOPO) might be a viable alternative to the TOP-TOPO passivated samples. Is it also possible to significantly improve the photoluminescence properties of the nanocrystals without the help of post preparative treatments (like HF etching)? Is the presence of TOP molecules at the particle surface really needed?

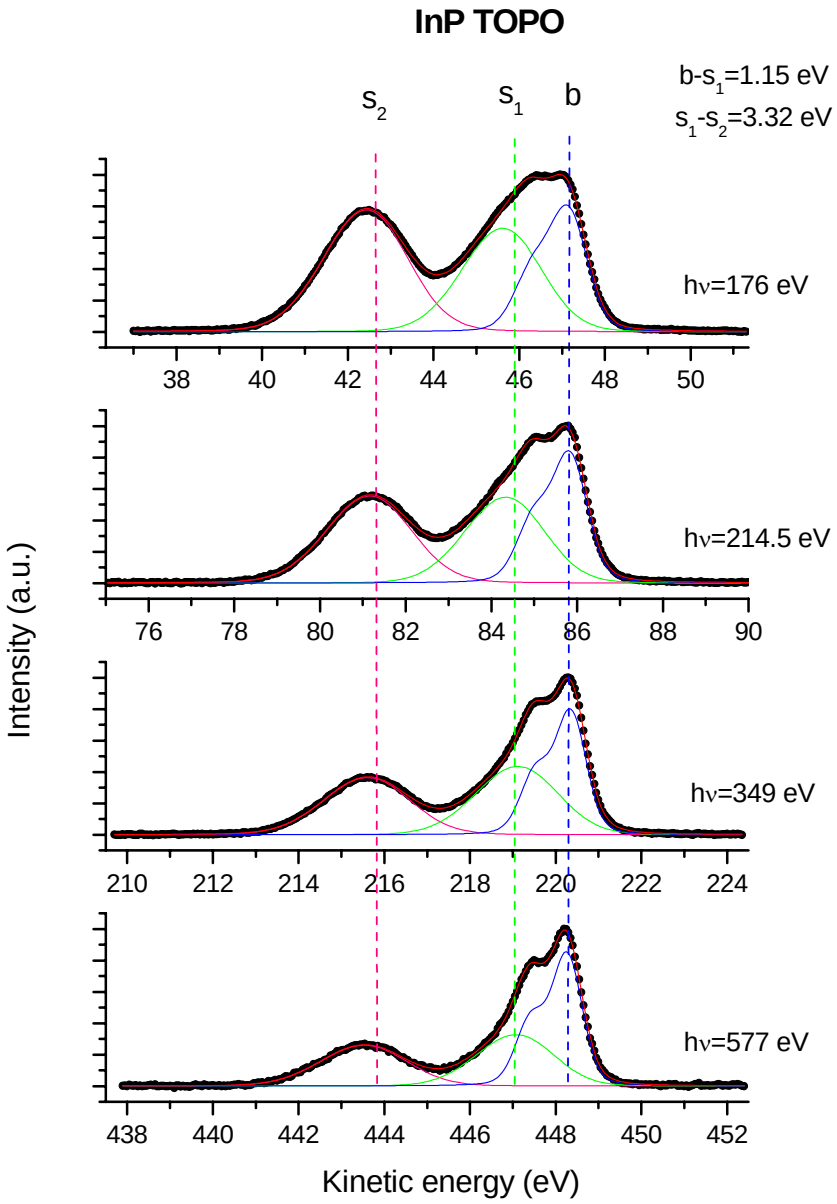

Figure 4.24 a). **P 2p** core-level photoemission spectra of 4.1 nm mean diameter crystals. Component **b** is due to atoms in the volume of nanocrystals, $\mathbf{s_1}$ and $\mathbf{s_2}$ are surface core-level shifts. The TOPO preparation path significantly reduces the signal from s_1 surface atoms (there are no phosphorous TOP atoms)

To answer previous questions, a new way of preparing InP nanocrystals, employing only TOPO molecules as stabilizing agents and ligands was developed and the results are TOP free nanoparticle:

$$InCl_3 \xrightarrow{\text{stabilising agent (TOPO)}} TOPO \cdot InCl_3\,(\text{soluble}) \xrightarrow{TMS_3S+\text{ligand (TOPO)}} InP \text{ nanocrystals} \qquad (4.4)$$

The internal structure of the resulting nanocrystals is very similar with the one of the nanoparticles prepared via TOP-TOPO pathway. The size selective precipitation process occurs with good efficiency. The XRD patterns of TOPO capped nanoparticles indicate the bulk phase of InP zinc-blende structure. The HRTEM images reveal well separated crystalline structure with clearly resolved lattice fringes and size distribution is rather narrow (10%) [65].

The PL efficiency is very low (<< 1%) for our nanoparticle with an average diameter of 4.1 nm.

From the way of preparing the TOPO capped nanocrystals one would expected a decreasing in intensity for the surface $\mathbf{s_1}$ component (due to dangling bonds) with respect to $\mathbf{s_1}$ component of methwash sample (due to dangling bonds and phosphorus signal from TOP molecule). The signal $\mathbf{s_2}$ from phosphorus TOPO molecules and native oxides should increase due to the significant presence of TOPO ligands.

The energy dependent spectra for P 2p core-level lines prove that the previous hypothesis is correct. The $\mathbf{s_2 / s_1}$ ratio has increased significantly relative to the case of methwash sample (see **figure 4.24 b**). The bulk component **b** has well resolved spin-orbit splitting (0.86 eV) indicating high degree of crystallinity for the volume atoms.

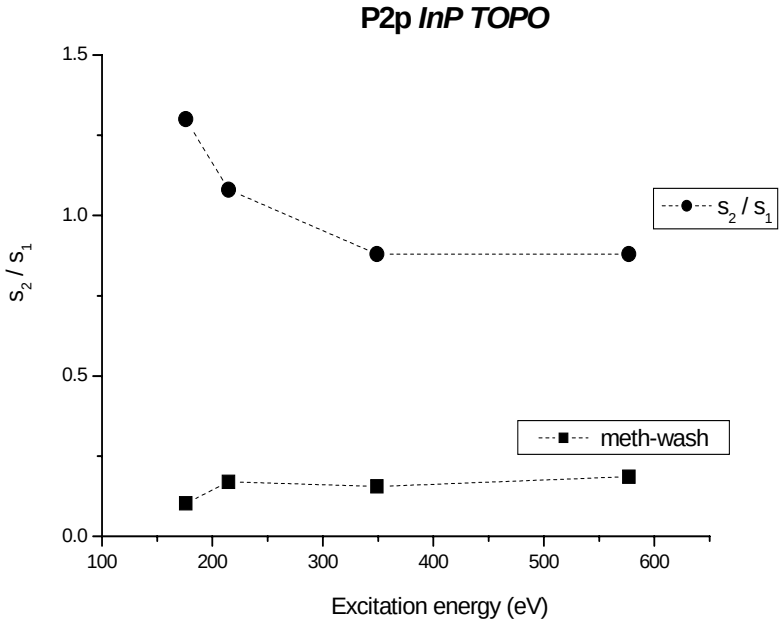

Figure 4.24 b). The $\mathbf{s_2 / s_1}$ ratios for the TOPO capped sample. For comparison, the $\mathbf{s_2 / s_1}$ ratios of the meth-wash sample are also displayed.

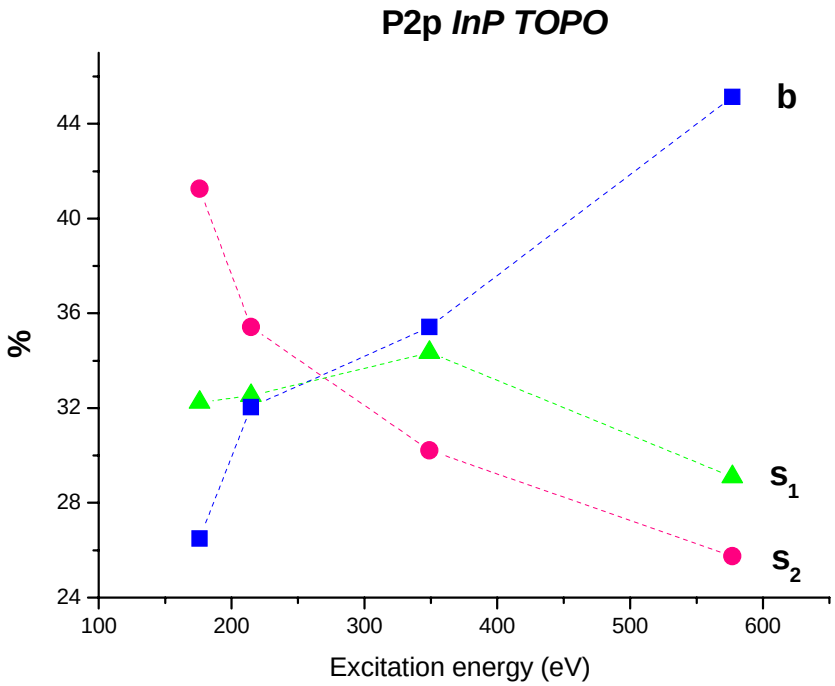

Figure 4.24 c). Energy dependent contributions (%) for bulk and surface components, TOPO capped sample. The dashed line is shown for eye guidance.

The energy dependent contribution for bulk and surface species are plotted in **figure 4. 24 c)**. As expected, the surface component $\mathbf{s_2}$ is dropping and volume component **b** is significantly increasing once the excitation energy is raised. However, the contribution curve of $\mathbf{s_1}$ component has a maximum at 349 eV. This might be the result of a larger broadening (gaussian) for the $\mathbf{s_1}$ surface component since the intensity of the $\mathbf{s_1}$ component drops with the increasing excitation energy. Also the fitting procedure contributes somehow to this feature.

4.3.8 TOPO capped sample – HF etched

The goal of the sample investigation was to spot the differences that occur at the nanocrystal surface after the HF etching treatment and to compare them with the results for the non-etched TOPO capped sample. It is also very important to see if there is a general trend in case of the HF etched samples.
The TOPO capped nanocrystals were etched according to the previously described method [65]. The PL quantum efficiency is significantly improved (up to 10%) when compare with the TOPO capped sample.

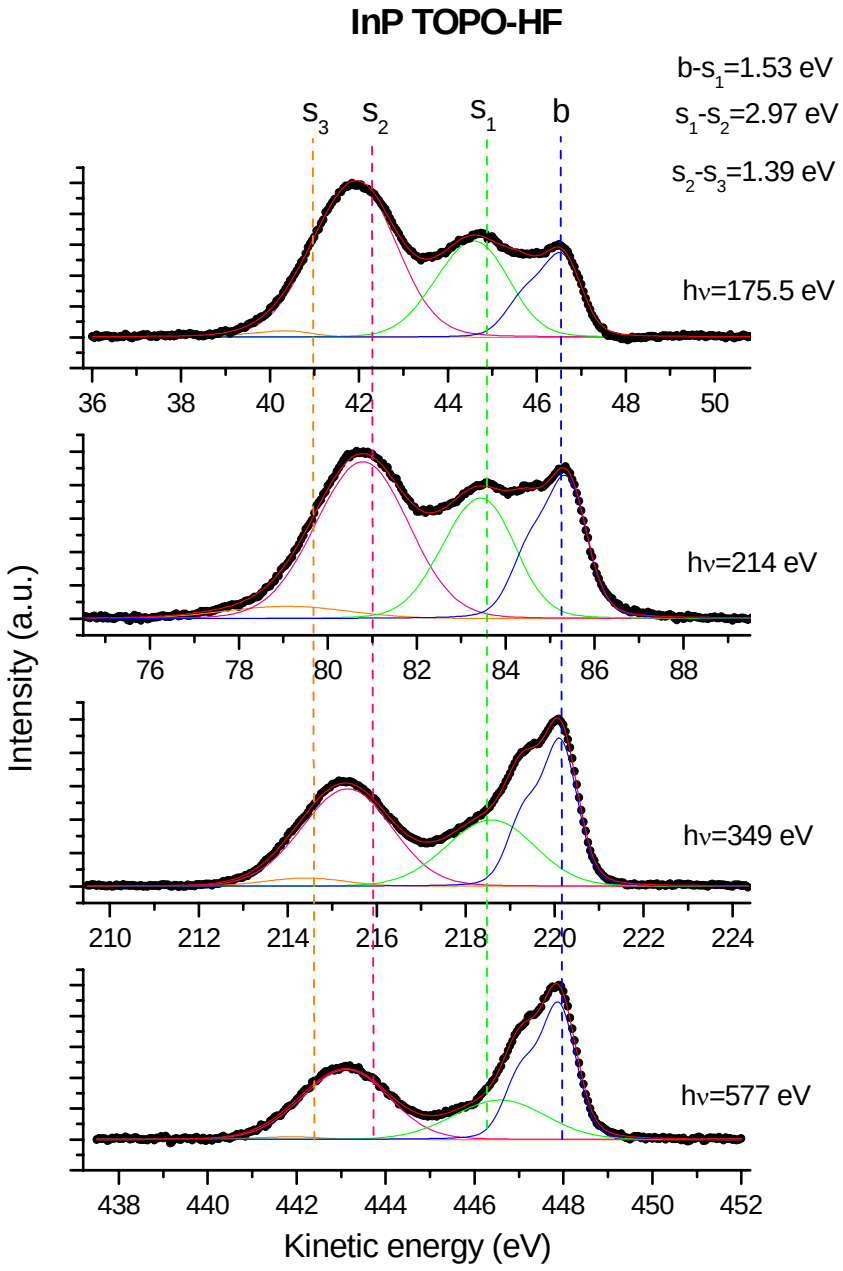

Figure 4.25 a). Energy dependent spectra (**P 2p** lines) of TOPO capped HF etched nanocrystals. The s_2/s_1 ratio and the PL significantly increase after the etching procedure.

Additional to the volume **b**, surface $\mathbf{s_1}$ and $\mathbf{s_2}$ components that are also present for the non-etched sample, another $\mathbf{s_3}$ surface component is required for a good fitting procedure. This $\mathbf{s_3}$ component reflects the signal from P-F bonds resulting after the etching treatment; its large chemical shift agrees with the values for P-F bonds reported in literature [82].

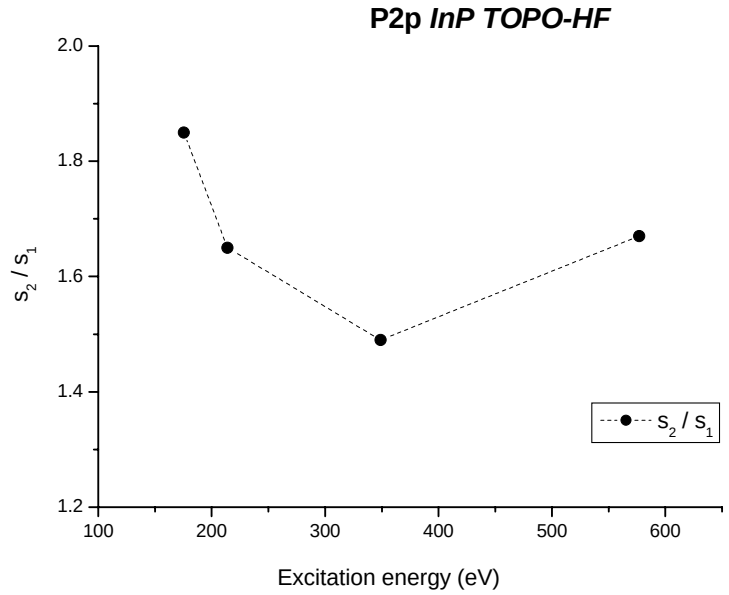

Figure 4.25 b). The s_2 / s_1 ratios for the TOPO capped HF etched sample

The s_2 / s_1 ratio is enhanced now comparable to the with the similar ratio for the non etched TOPO sample (**figure 4.25 b**). It follows the same trend like the corresponding TOP-TOPO capped samples. The surface components dominate the total signal in case of **P 2p** core level spectra (**figure 4.25 c**).

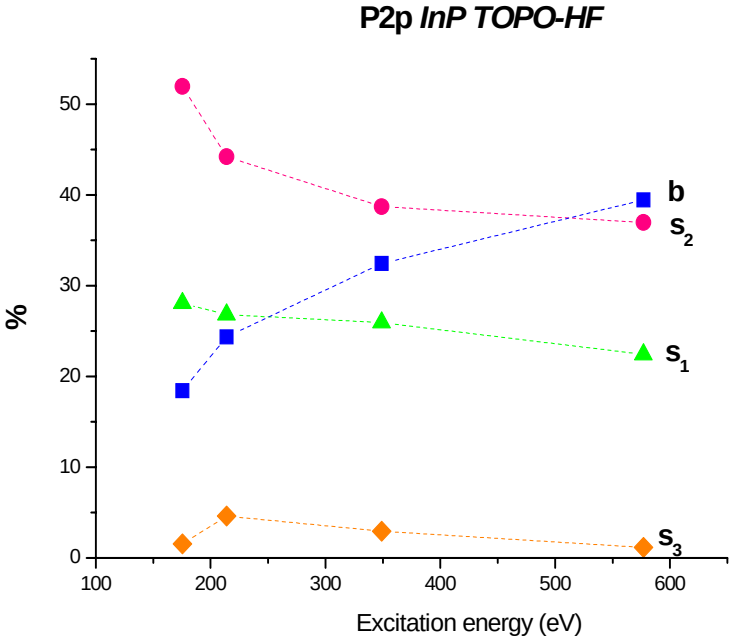

Figure 4.25 c). Energy dependent contributions (%) for bulk and surface components, TOPO capped HF etched sample.

General remarks on the P 2p core level investigation

In the following, an overview of the previous investigated nanocrystals is given. Phosphorous 2p spectra of all *eight* samples are shown in **figure 4.26**. Since the measurements were done during *three different* beamtime periods, there are no spectra recorded with exactly the same energy for all measured nanoparticles. However, all samples were investigated with excitation energies hν in the range of 341-369 eV and this means rather similar kinetic energies for the escaping electrons (212-240 eV for the volume component **b**). So, one can conclude that the spectra of all samples have the same surface sensitivity and shape difference are mainly due to various surface treatments.

For a more convenient and compact display of the spectra, the values on the *x axes* are given on binding energy and shown only for the last two samples.

The differences between **InP as prepared** and **InP methwash** sample are rather small, there is only a reduced contribution for the surface $\mathbf{s_1}$ (TOP and dangling bonds) and $\mathbf{s_2}$ (TOPO and native oxides) components in case of the washed sample. Since the average size of the two samples is comparable, one explanation for the observed trend is that the excess of TOP-TOPO ligands is successfully removed in case of **methwash** nanocrystals.

The **pyridine** capped InP nanoparticles represent a successful way of recapping the original TOP-TOPO passivated nanoscale crystals. The presence of TOP-TOPO molecules at the surface is drastically reduced and this has as direct effect the reduced intensity for the $\mathbf{s_1}$ surface component. The $\mathbf{s_2}$ component is slightly enhanced when compared with the **methwash** sample and one explanation might be the enhanced surface oxidation due to a less effective surface passivation.

The **InP oxidized** sample shows a drastically enhancement of the surface $\mathbf{s_2}$ component due to the extensive exposure to the oxygen atmosphere. Contributions to this component are expected to come from native oxides, rich in oxygen and TOPO ligands.

For all **HF etched** samples a new surface component $\mathbf{s_3}$ is required to reflect to P-F bonds that are present at the surface of nanoparticles. Since the etching treatment is done in presence of considerable amount of TOPO molecules, the $\mathbf{s_2}$ component (due to P-O bonds) is, as expected, enhanced with respect to the non-etched samples.

The **InP HF-nitrogen light** is the corresponding etched sample of the **as prepared** nanocrystals since both samples were not methanol washed. One can clearly see that the surface $\mathbf{s_1}$ component assigned to signal from phosphorous TOP atoms and dangling bonds is now reduced and there is a significant increase in intensity for the $\mathbf{s_2}$ component.

The same trend is spotted in case of **InP HF high** sample when compared with the corresponding non etched **InP methwash** one. The $\mathbf{s_2 / s_1}$ ratio higher for the etched particles when compare with the similar ratio of the non etched sample.

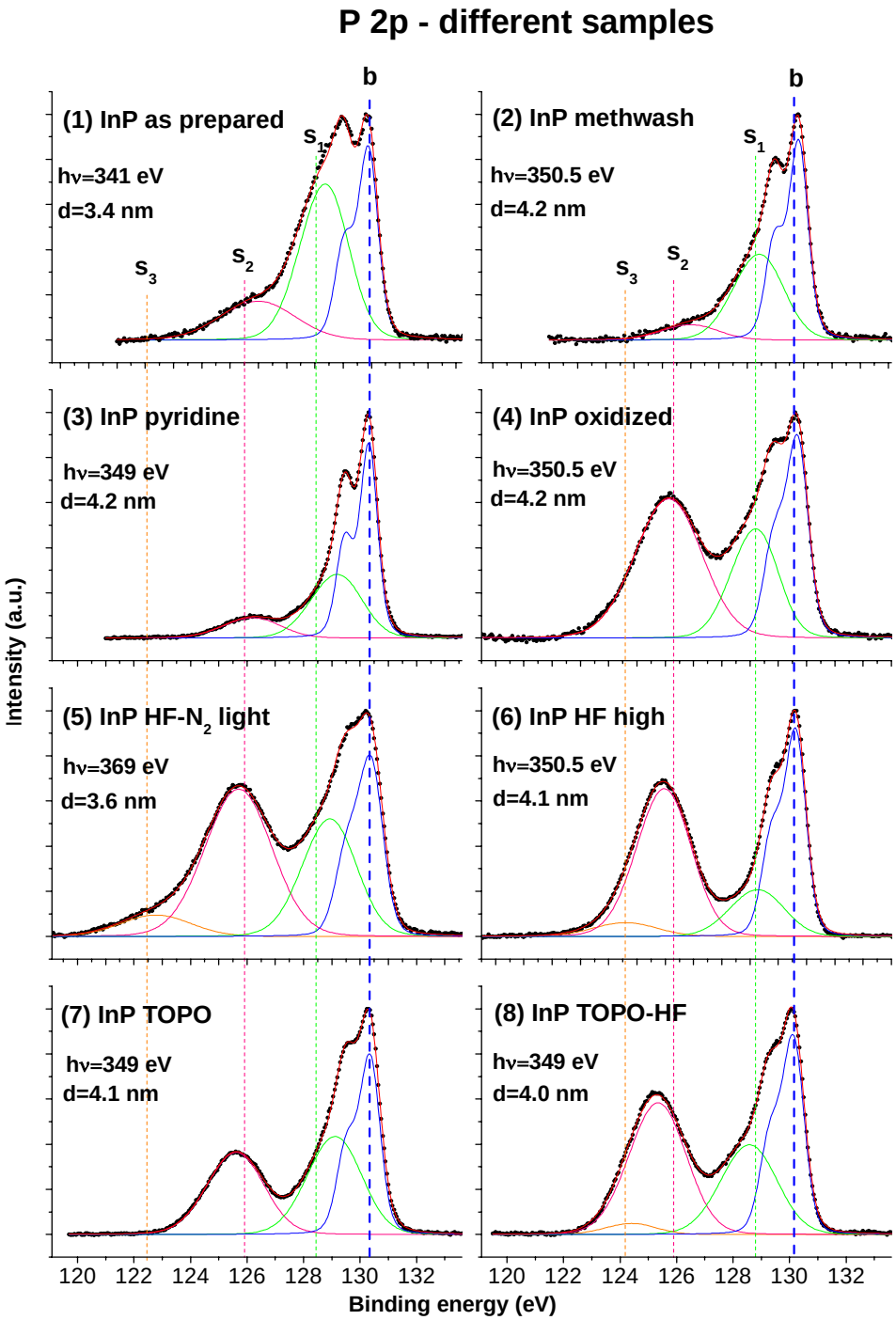

Figure 4.26. Summary of **P 2p** core level lines corresponding to the samples present in this study. The excitation energy is in the 341-369 eV range. The **b** line indicates the binding energy of the volume component. However, the $\mathbf{s_1}$, $\mathbf{s_2}$ and $\mathbf{s_3}$ lines are not supposed to give the exact position of the surface shift since the values for the chemical shifts are different for each samples; the eye is mainly guided by those lines. The exact chemical shifts for each sample are plotted in figure 4.27. The excitation energies for each sample and the average diameter are also given.

The s_2 / s_1 ratio is significant higher for the etched particles when compared with the corresponding ratio of the non-etched sample.

The last two samples, capped only with TOPO ligands do not make an exception from the previous trend. The **InP TOPO HF** sample has the s_2 / s_1 ratio with respect to the corresponding **InP TOPO** non etched sample.

The photoluminescence efficiency at room temperature is very low for all non-etched samples (<<1%) but significantly increases, up to 3-20% in case of etched nanocrystals.

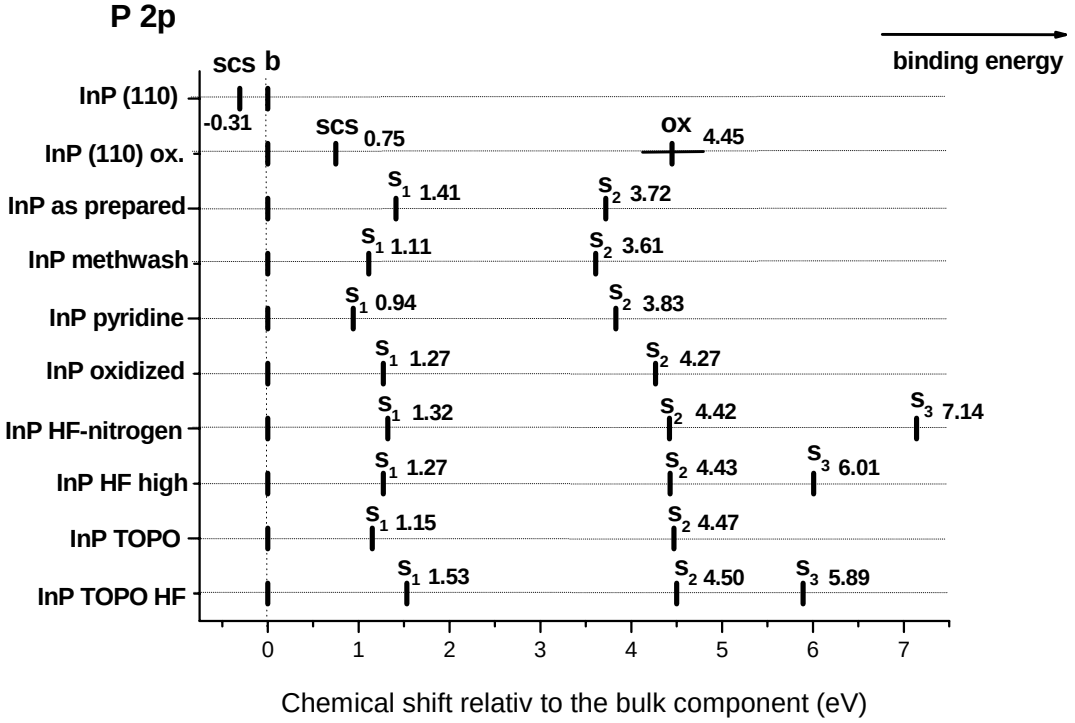

Figure 4.27. The **P 2p** chemical shifts relative to the volume **b** component in case of bulk and nanocrystals InP samples. There are two surface components in case of non etched InP nanocrystals and three surface components in case of HF etched nanoparticles. The surface core level shifts (**scs**) of the bulk samples are also displayed.

An overview picture regarding the **P 2p** chemical shifts of the investigated InP samples is presented in **figure 4.27**. All components are referred to the volume component **b**.

In the case of bulk InP(110) surface there are fitable surface core level shifts (**scs**) originating from the P dangling bonds at the surface for both clean and oxidized samples. The contribution of oxides with maximum signal at 4.45eV lower binding energy agrees with the previous investigations. The dangling bonds signal in case of InP nanocrystal samples cannot be separate from the TOP

phosphorous contribution. The combine contribution is reflected by the $\mathbf{s_1}$ surface shift. Different ways of preparation successful vary the $\mathbf{s_1}$ value and conclusion about the surface passivation can be drawn.

The $\mathbf{s_2}$ surface core level shift reflects the signal from P-O bonds: phosphorous from TOPO molecules and native oxides. The shifts are smaller in case of as prepared and pyridine capped samples.

In case of etched samples a third surface component $\mathbf{s_3}$ appears as signal from P-F contributions. The shifts are significantly large in case of HF etched under nitrogen sample.

4.3.9 In 3d core-level spectra

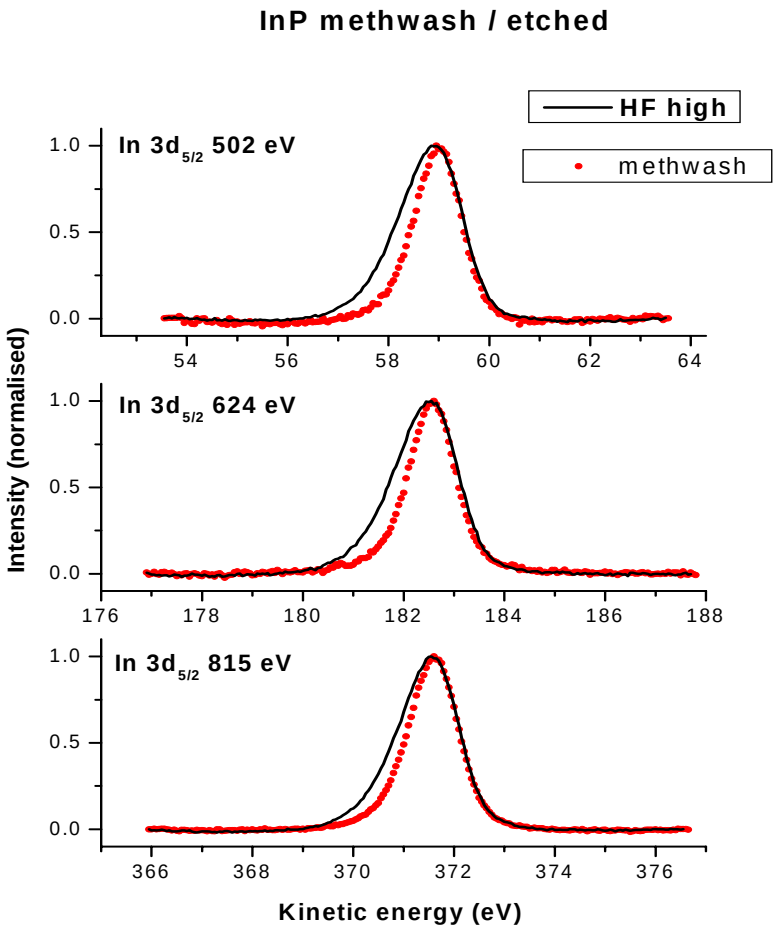

Figure 4.28. **In 3d $_{5/2}$** core level lines of methanol wash and highly luminescent etched samples. The detailed spectra recorded with the same excitation energy are overlap after a linear background subtraction

The **In 3d** and **In 4d** core level lines are supposed to provide useful information about the surface structure of the InP nanoparticles, similar to the investigation of the **P 2p** lines. Unfortunately, the

shape of **In 4d** core lines is affected by the vicinity of O 2s and O 2p lines. Also Cl 3s originating from the $InCl_3$ salt used for the preparation of the nanocrystals may overlap with the **In 4d** lines.
The only possibility that remains is to investigate the **In 3d** core-level lines.
However, the **In 3d $_{5/2}$** spectra are more difficult to fit using a standard procedure because of the decreasing instrumental resolution due to the necessity of using high excitation energy combined with the low count rate. There is also the "physical" aspect - small chemical shifts in case of surface oxidation or HF etching treatment for In sites. One approach in case of **In 3d** investigation might be simply to overlap intensity normalized spectra of two different samples (methwash and highly luminescent HF etched) irradiated with the same photon energy. **Figure 4.28** shows for the surface sensitive regime (50 to 60 eV kinetic energy) a much broader **In 3d $_{5/2}$** spectrum for the etched InP sample relative to the methanol-wash one. Sharper feature in case of the sample washed with methanol results from the significant presence of the TOP ligands at the nanocrystals surface and possible bonds with In surface atoms (In-P bonds) creating a bulk InP like signal in the spectrum. Only In-O bonds (mainly with TOPO ligands) and free In atoms at the surface might contribute to the experimental broadening but the number of those sites is limited as shown by the previous **P 2p** data. According to **In 3d** core-level studies on InP (110) oxidized surface the chemical shift values (In-O bonds) in those cases should be located to 0.3-1.3 eV lower kinetic energy [73, 79].
The same hypotheses can be applied in case of InP HF etched sample (InP HF high). Now, the bulk like signal is reduced due to decreasing presence of TOP molecule on the InP nanoparticle surface. On the other hand the surface oxidation is more intense and together with In-F bonds increase the broadening for **In 3d** peaks; the chemical shift for the In-F compound is located to 1.5 eV lower kinetic energy relative to the main line of a InP sample [82]. For a more bulk sensitive regime (365-380 eV KE) the broadening for the both sample decreases due to the enhanced contribution of bulk atoms at the photoelectron yield.

4.4 Discussion of the etching mechanism. Conclusions

Absorption and PL experiments on nanocrystals prepared in various ways have shown that high luminescence efficiency is reached only after HF photochemical treatment of the nanoparticle surface [65].
Theoretical calculation of H. Fu [66] predict in case of P dangling bonds (DBs) a state just above the valence band (0.64 eV for a dot diameter of 1.86 nm- the value is slightly reduced once the size of the particle increases) which will act as a trap for the photogenerated holes. The In dangling bond has a state just below the conduction band, 0.50 eV for a dot diameter of 1.84 nm - the value is significantly

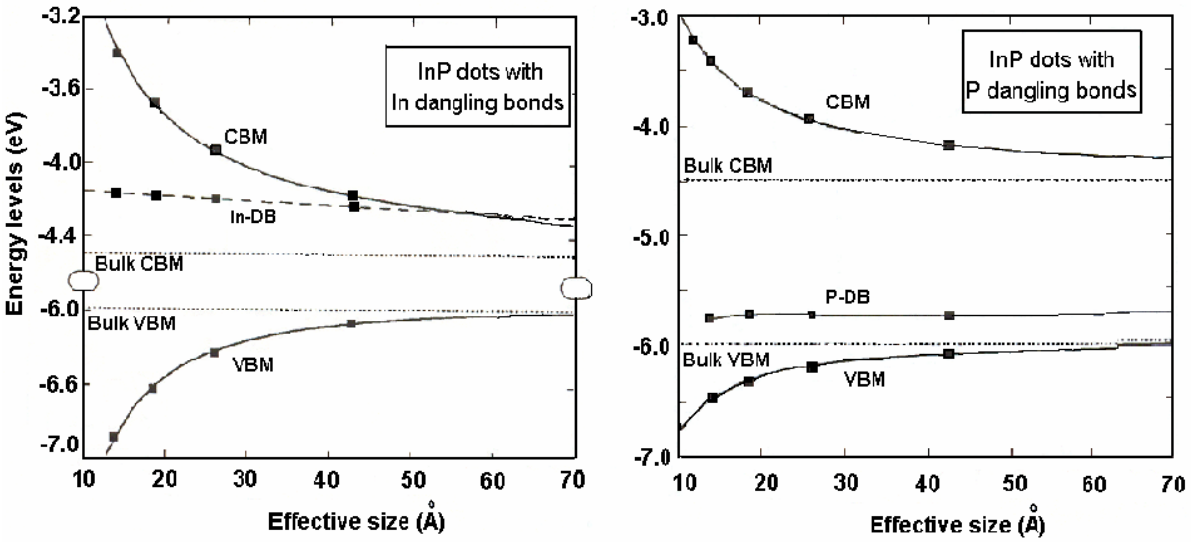

Figure 4.29. Variation of the In (*left*) and P (*right*) dangling bonds, the conduction band minimum (CBM) and the valence band maximum (VBM) with the size of InP dots. From [66]

reduced once the particle size increases and is no more in the band gap for dot sizes larger than 6 nm. The reduction of dangling bonds and the improved surface passivation that suppress non-radiative recombination pathways is a crucial point in designing nanocrystals with high photoluminescence efficiency.

In case of as-prepared nanocrystals the existence of In DB is questioned by the presence of significant amount of TOPO ligands that cap (reduce) the In surface non-passivated atoms. TOP molecules might also passivate the In DBs.

Responsible for the low PL might be the P DBs that are not passivated by the TOP-TOPO ligands. It is assumed that only one fast surface trap per nanocrystal can drastically affect the photoluminescence by providing non-radiative recombination pathways (PL efficiency <<1%).

Post-preparative modification of the particle surface provides a way to eliminate those undesirable trap sites. The most efficient method is etching with HF solution in presence of illumination, resulting in a strong band edge photoluminescence.

The etching model sketched in **figure 4.30** is based on the present investigation of the InP nanparticle and was proposed by Talapin [65]. The In DBs are supposed to be efficiently passivated by the TOP-TOPO ligands. Not the same thing is available for the P DBs that are present at the surface of the non-etched samples.

The first step of the HF etching treatment is the photon absorption and creation of hole-electron pairs. This initial step justifies the role of light in the photoetching treatment. The InP nanocrystals HF etched without exposure to light show no improvement of the photoluminescence relative to the non-

etched samples. It is known that bulk InP does not dissolve in dilute HF solution even under anodic bias [84-86]. The next step of the process is the capture of the photogenerated hole by a surface bond (P-dangling bond) and an intermediate decomposition state is formed [84, 85]. The efficiency of the etching process is determined by the capture rate.

The photochemical etching of bulk InP samples in acidic solution indicated that six elementary charges are required for the dissolution of one formula unit of InP. This value results by measuring the quantity of photodissolved In and the number of charges created during the photoetching process [86]:

$$InP + xh^{+} \rightarrow In^{3+} + P^{3+} + ye^{-} \qquad where\ (x+y)=6 \tag{4.5}$$

The P dangling bond is now activated for a nucleophilic attack (nucleophile means electron rich) with fluorine ions from acid solution. The intermediate state is unstable [84, 85] and the reaction reaches an end once the P atom is converted in PF_3 and is removed from the InP nanocrystal surface. The remaining site, rich in In, is passivated by the TOPO molecules present in the etching solution. The photogenerated electrons react with acceptors from solution, e.g., dissolved oxygen.

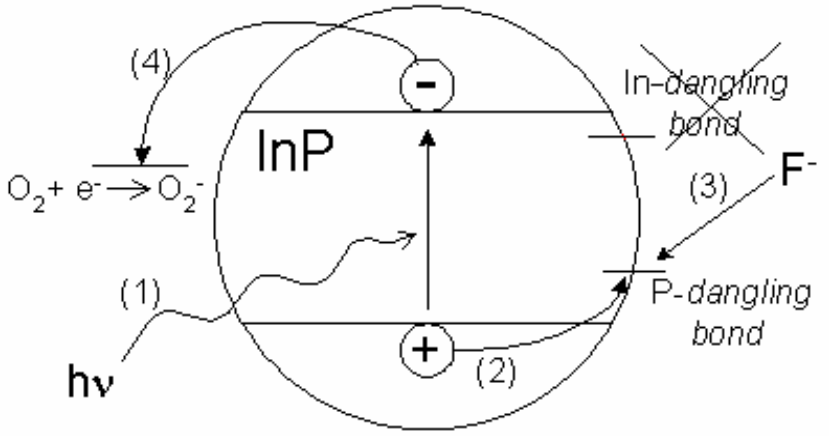

Figure 4.30. The 4 steps of the photoetching mechanism for InP nanocrystals:
(1)-photon absorption resulting a electron-hole pair
(2)-capture of the hole by a P surface bond
(3)-nucleophilic attack with fluorine ions
(4)-electron reacts with acceptors form solution

The presence of oxygen is required in order to obtain highly luminescence efficiency for our samples. The sample etched under nitrogen (**InP HF-nitrogen light**) has less than 5% PL efficiency and the lack of oxygen stops the etching process in an intermediate phase. It seems that the surface P atom

(dangling bond) is not removed from the surface and result is strong P-F signal (s_3 surface component for **P 2p** core-level spectra) relative to the similar sample that was etched in presence of oxygen.

The photochemical etching of the bulk InP samples showed that the relative stability of the InP faces is (111) > (110) >$(\bar{1}\bar{1}\bar{1})$ and this means that the dissolution of P rich face $(\bar{1}\bar{1}\bar{1})$ is enhanced comparable with the (111) face consisting of only In atoms. The TOPO capping of the In sites should increase the resistance against the HF etching. This assumption is also supported by the fact that some of the In oxides formed at the surface of bulk InP crystal are insoluble in solution of HF acid [86].

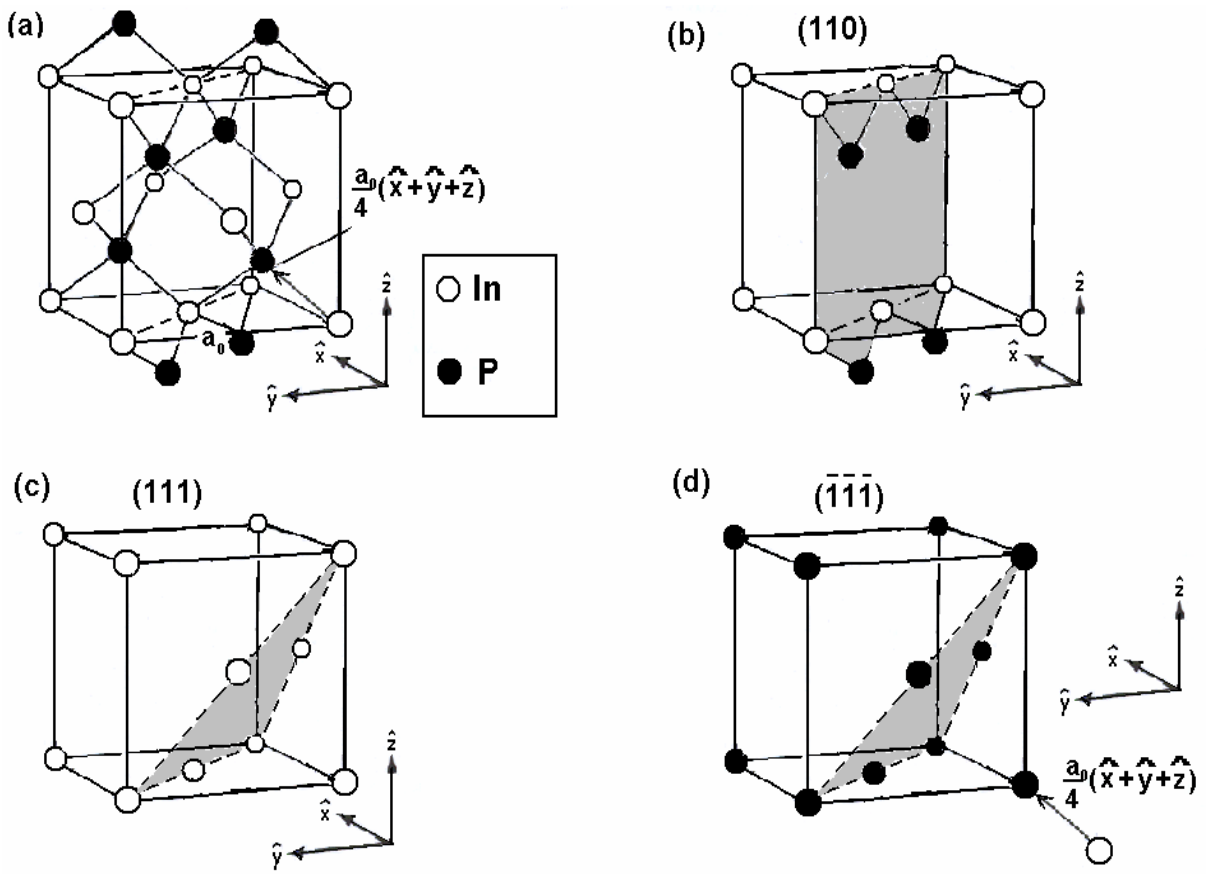

Figure 4.32. a) Atomic arrangement for the bulk InP (zincblende structure). Schematic view of the b) - (110) surface, c) - (111) surface and d) - $(\bar{1}\bar{1}\bar{1})$ surface of the InP crystal.

In fact, a very simple way to clear this aspect is to compare the **In 3d** lines for the oxidized and HF etched under air samples (**figure 4.31**). For the etched sample, one can notice the lower intensity for the surface species having high chemical shifts. This indicates that the possibility of having In-F bonds is low in case of etched sample in presence of air and light. The broadening of both samples is mainly the results of different In-O bonds.

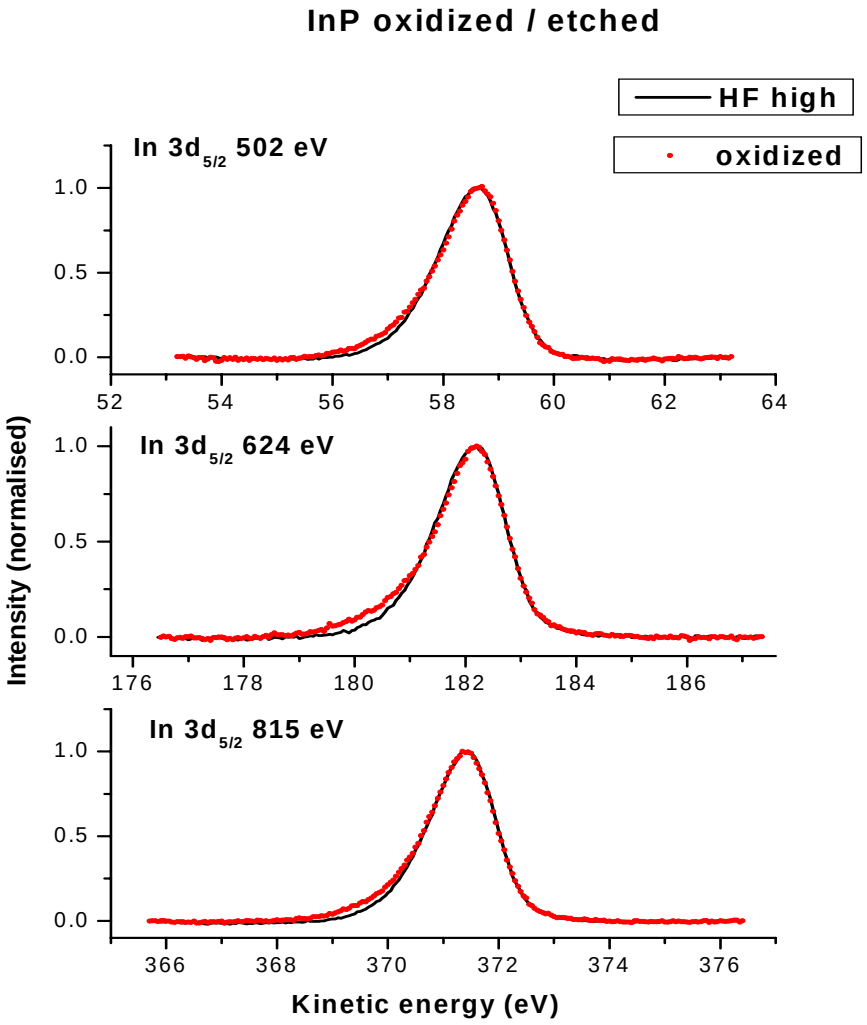

Figure 4.31. Experimental curves of **In $3d_{5/2}$** core level line, oxidized and etched samples. The oxidized sample has a broader shape than the etched sample due to significant amount of In-O bonds with high chemical shifts.

The most successful way of preparing highly luminescent InP nanocrystals proved to be the HF etching of TOP-TOPO capped nanoparticles in presence of oxygen and light. The resulting PL efficiency is strongly dependent on the amount of HF in the etching solution. Effective treatment of nanoparticles with average diameter of 4.5 nm requires $3 \cdot 10^3$ – 10^4 HF molecules per one InP nanocrystal (PL > 20%). Lower or higher amount of HF results in reduced PL efficiency.

By simply reducing the HF concentration at 10% relative to the value for **HF high (PL 20%)** sample (4.1 nm average diameter), a new etched sample, **HF high (PL 10%)**, was obtained (with the same 4.1 nm average diameter). The PL quantum efficiency is reduced now at a value of about 10%, this means half of the value corresponding to **HF high (PL 20%)**.
The diffraction and TEM images did not revealed significant differences between the two samples.

The photoelectron spectra (**P 2p** lines) are recorded under the same experimental condition for both samples. The fitting results indicate similar (almost identical) contributions for bulk and surface components (**figure 4.32**).

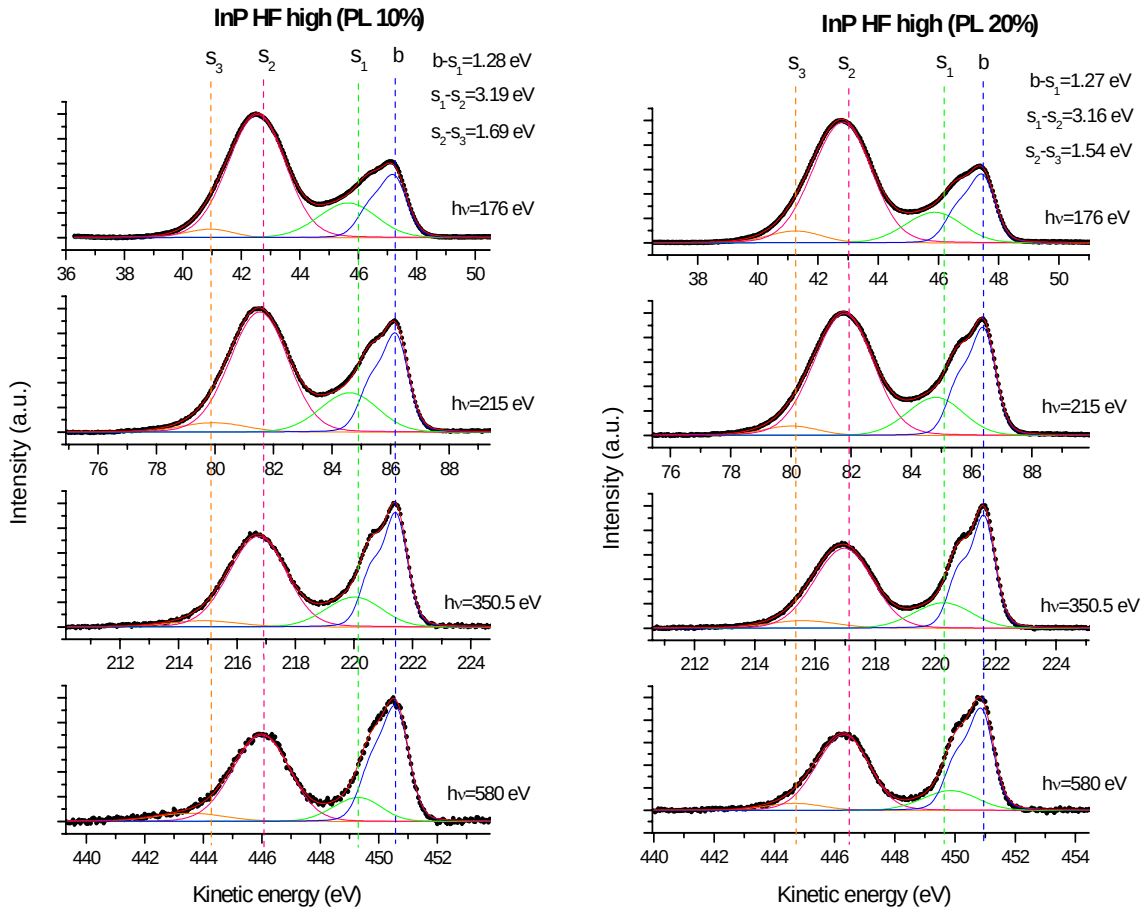

Figure 4.33. Energy dependent spectra for highly luminescent (PL 10%) and (PL 20%) etched samples. The bulk and surface component contributions for **P 2p** core level lines shifts are very similar for both HF etched under air samples.

The chemical shifts for the corresponding components of the two etched samples are also very similar.

The investigation of **In $3d_{5/2}$** core-level lines reveals no clear difference in shape for spectra recorded with the same excitation energy (see **figure 4.33**). The lines are obtain after a linear background subtraction and forced to have the maximum intensity at the same kinetic energy.

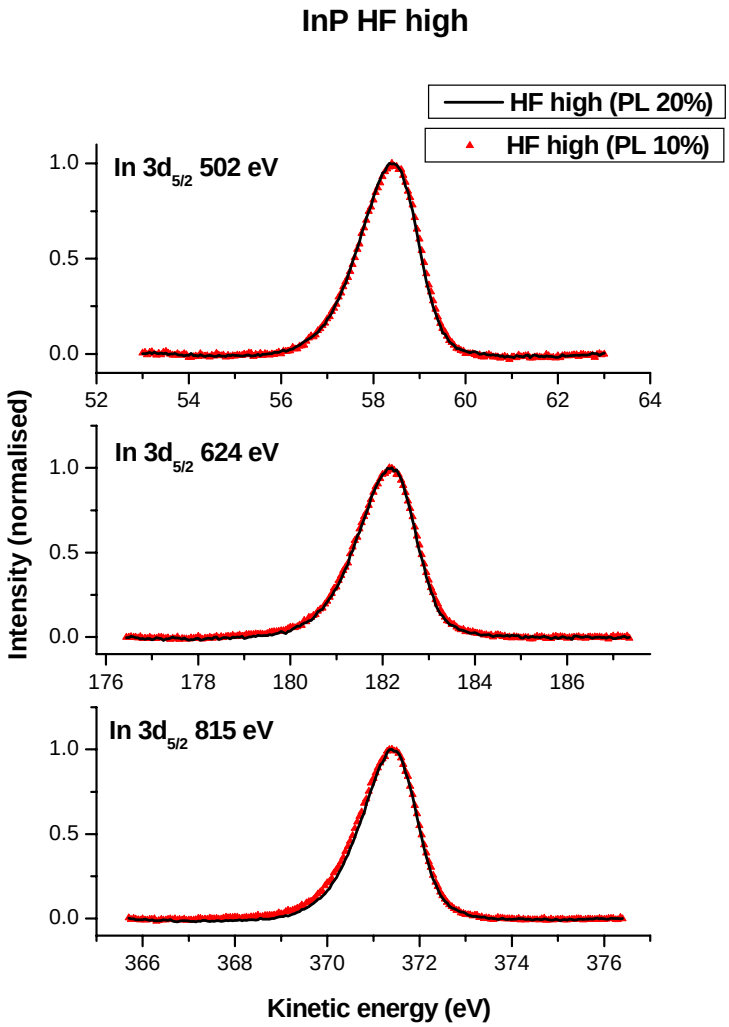

Figure 4.34. **In $3d_{5/2}$** core level lines of highly luminescent etched samples (10% and 20% PL quantum efficiency). Experimental curves of both samples are almost identical.

The small differences of core level lines that correspond to samples with rather different PL efficiencies are not surprising. This aspect is simply explained by the fact that already one or two unpassivated sites per nanocrystal result in a completely extinction of the PL.

The final conclusion of this investigation is that the post-preparative treatments like HF etching are required in order to improve the photoluminescence efficiency of InP nanocrystals. Under optimized conditions (light intensity, amount of HF, ligands, etc.) the PL quantum efficiency can reach more than 40% [65].

The evolution of the s_2 / s_1 ratios for all samples versus excitation energy are plotted in **figure 4.35 a)**. For all samples the s_2 / s_1 ratios show only small variation once the excitation energy takes different values. This result is in agreement with the assumption that components s_1 and s_2 represent signal

from genuine surface environments. Instead, there are strong ratio variations in case of different treatments and increasing in s_2/s_1 ratio has a direct but nonlinear response in the improving of PL efficiency. The nonlinear response in the PL yield could be explained by the fact that generally, already few unpassivated surface sites can lead to poor PL properties. There is only one exception from the rule, the oxidized sample. But the explanation for the high s_2/s_1 ratio is the significant amount of phosphorus oxides on the nanocrystal surface (component s_2). The s_1 contribution due to non passivated sites is not reduced relative to other non-etched samples resulting a very low PL efficiency, <1%.

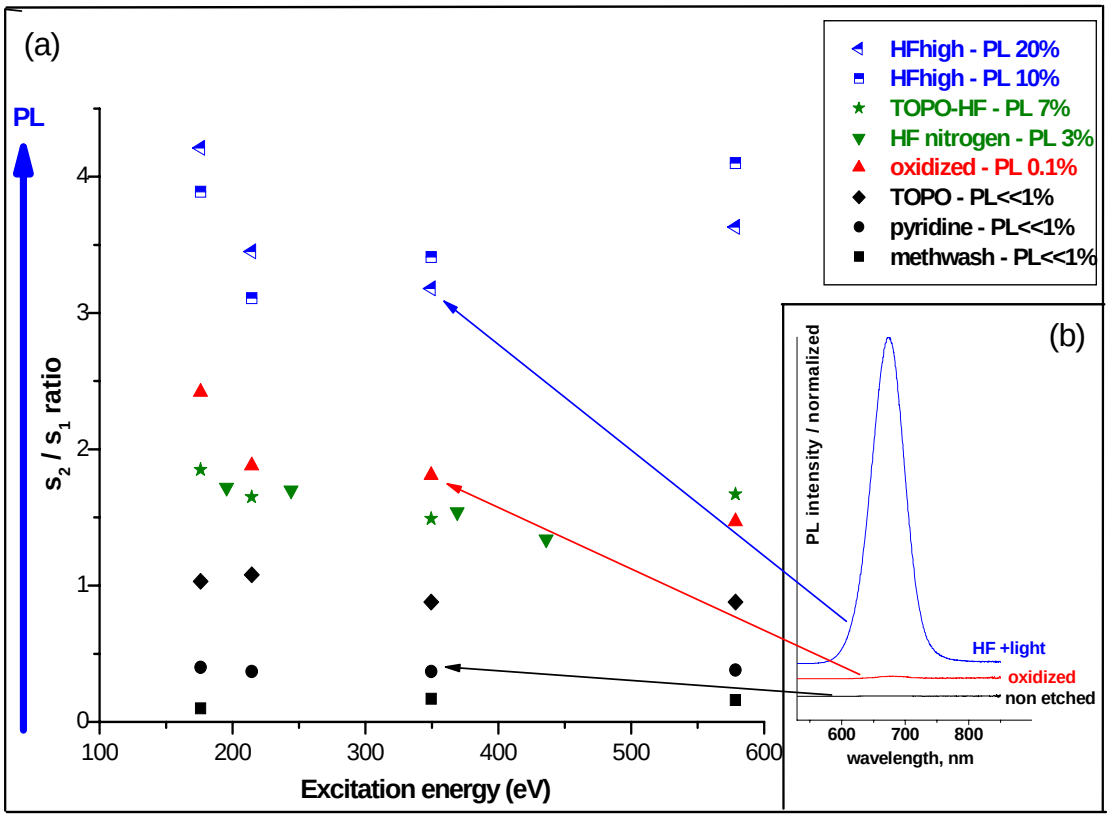

Figure 4.35 a). The s_2 / s_1 intensity ratios of InP nanocrystal samples at different excitation energies. There is a direct relation between the PL efficiency and surface component ratios. b). Representative PL spectra measured for InP nanocrystals before and after treatment with HF [65].

The etching process is a photochemical one and the best proof is the size selective photoetching of the present investigated nanocrystals [65].

The size of the nanocrystals usually decreases during the etching process. The smaller particles are etched faster than the larger ones and the result is large broadening of the nanocrystal size distribution. However, this unwanted situation may be avoided if one considers the strong quantum

confinement effect of the particles and the previous discussed mechanism of photoetching. The smaller nanoparticles have their absorption onset shifted towards blue with respect to larger particles. If the nanocrystals are illuminated through a filter cutting off the short-wavelength, the light excites only the largest particles and the smallest cannot absorb radiation. Once the particle size decreases upon etching below a certain value, the corresponding absorption onset shifts towards wavelength that are blocked by the filter and the etching mechanism terminates.

.

Chapter 5. Cu clusters

In this chapter the production and characterization of small Cu clusters is depicted.
Copper is one of the oldest metals ever used and has been one of the important materials in the development of human civilization. Because of its properties, Cu has become a major industrial material (metal) with broad applications like electrical power transmission and generation, telecommunication, electrical and electronic products. From this point of view, the scientific interest in Cu is obvious.
The geometrical structure of a Cu single crystal is known to be *fcc* like with a near neighbor distance of **a**=2.556 Å, but less information is available on small Cu clusters. Typically, the geometric structure changes significantly with each atom added to edifices that contain less than a few tens of atoms. This means that one can tailor the electronic, magnetic and optical properties of pure and compound clusters by simply tuning the nanoparticle size. Direct applications are in the field of catalytic processes [87] and magneto-electronic devices [88].
Small Cu clusters were successful prepared using various techniques: radiation induced from aqueous solutions [89], gas aggregation [90], laser vaporization [91], self assembling (Vollmer Weber) [92]. Depending on the production method, the clusters are studied on gas phase, on supports or embedded in rare gas matrices or polymers.

In the present investigation, with the help of the pick-up technique, Cu atoms are embedded inside host Ar clusters and form metallic clusters. The average sizes of the resulting clusters are then estimated with the help of a Reflectron Time of Flight Mass Spectrometer.
There is a significant number of articles investigating embedded clusters synthesized by means of the pick up technique but mainly free cluster (gas phase) studies [93, 94, 95, 96, 97, 98]. Deposited clusters that are isolated inside rare gas matrices are less represented in literature due to technical challenges (very low temperature for substrates, soft landing conditions, etc.). This gives a good reason for studying the electronic and geometric structure of nanoparticles that are deposited on substrates.
The spectroscopy investigations are performed on Cu clusters that are deposited inside an Ar matrix on a cold sample holder (10K). The qualitative analysis of the deposited samples (survey and detailed spectra) were done using PES, the photoelectrons being recorded with an Omicron EA125 hemispherical energy analyzer at normal emission mode (angle).
The main investigation method of the Cu cluster was the Absorption Spectroscopy in the XANES regime, this means information about the internal structure of the deposited samples. The acquisition of the absorption spectra for Cu $L_{3,2}$ edges is performed simultaneously in two different ways:

-with a Keithley multimeter that reads the sample current and the results are TEY spectra
-with the electron analyzer set in the CFS Mode in order to record Auger spectra
The XANES spectra of Ar K edge are also recorded for pure or Cu doped Ar matrix.
Finally, the experimental absorption spectra of the Cu clusters are compared with the corresponding theoretical curves.

5.1 Cluster production and deposition

The use of expanding nozzle flows proved to be a successful way of producing (rare) gas clusters and investigating the nucleation and growth of the clusters. Briefly, the Ar gas at temperature T_0, having a stagnation pressure p_0 expands though a small orifice with diameter d_0 into vacuum. Due to (adiabatic) expansion, the Ar beam is cooled very fast and efficiently. Below a specific temperature the Ar atoms are cold enough and dimers are formed due to the "three particle impact"; the energy resulting after the formation of the two atoms molecule is transfer as kinetic energy to the third atom. The size of the cluster can further increase due to the previous described mechanism, or the condensation heat is stored by the cluster itself as internal energy (for example vibrational energy).

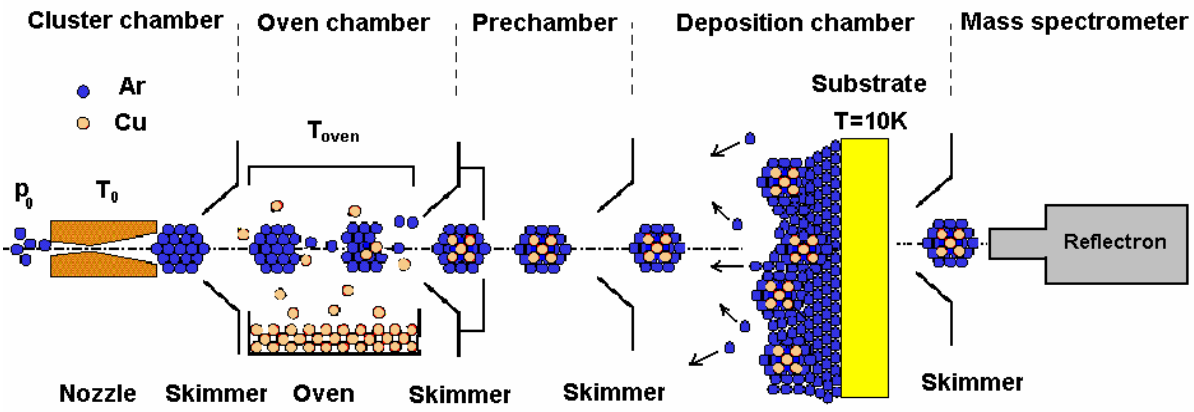

Figure 5.1. Schematic representation of the cluster experiment. The pick up process parameters are the stagnation pressure p_0, the nozzle temperature T_0 and the oven temperature T_{oven}. The oven crucible is filled with high purity bulk Cu. The size of pure Ar or embedded Cu clusters is measured with the Time of Flight Mass Spectrometer. The clusters are deposited on a cold substrate (Au coated Cu plate) and transfer in the analyzer chamber for further investigations.

The latest mechanism results in a gradual increase in temperature for the rare gas cluster and evaporation of some Ar atoms occur.

As Becker and co-workers observed in their pioneering experiment in year 1956 [12] that for a given d_0 diameter, the condensation efficiency is very dependent on the pressure p_0 and temperature T_0 parameters. Hagena [99] investigated further the cluster growth and proposed a new variable Γ^* for describing the degree of beam condensation:

$$\Gamma^* = k\frac{p_0[\text{mbar}](d_{eq}[\mu\text{m}])^{0.85}}{(T_0[\text{K}])^{2.2875}} \tag{5.1}$$

where *k* is a material constant, k=1646 for Ar [100], p_0 is the stagnation pressure, T_0 is the nozzle temperature and d_{eq} is the equivalent diameter [101]. In case of a conical nozzle (like that one used in this work) the value for the d_{eq} can be calculated in the following way:

$$d_{eq} = 0.719\frac{d_0}{\tan\theta} \tag{5.2}$$

where d_0 is the hole diameter and θ is the half of the opening angle.

In our case d_0=300μm and θ=8º. The value 0.719 is characteristic for monoatomic gases.

The d_{eq} is equal with the orifice diameter (d_{eq}=d_0) in case of a simple hole nozzle. The use of monoatomic gas and conical nozzle (θ=8º) has result an effective diameter d_{eq} that is 5.1 times larger than the orifice diameter. This means that the conical nozzle produces the same centerline flow with only 1/26 of the free jet mass flow for simple hole nozzle having identical orifice diameter d_0. The advantages of using conical nozzle with small opening angles are obvious.

The Ar stagnation pressure was in the range p_0=30-180 mbar for a constant nozzle temperature T_0=80K. This means that the Γ^* values for Ar are in the 1100-6600 range.

Buck and Krohne [102] indicated that the average cluster size $\langle N\rangle$ is given by:

$$\langle N\rangle = 38.4\left(\frac{\Gamma^*}{1000}\right)^{1.64} \quad \text{for } 350 \le \Gamma^* \le 1800 \tag{5.3}$$

For larger Γ^* values another equation has to be used:

$$\langle N\rangle = 33\left(\frac{\Gamma^*}{1000}\right)^{2.35} \tag{5.4}$$

Direct prediction of the size distribution for both pure and embedded clusters is done with the help of the Reflectron Time of Flight Mass Spectrometer. The measured size distribution in case of a logarithmic scale [103, 104] for the cluster intensity has the form:

$$f(N) = \frac{1}{N\sqrt{2\pi\sigma^2}}\cdot\exp\left(-\frac{(\ln N-\mu)^2}{2\sigma^2}\right) \tag{5.5}$$

$$\text{where } \mu = \ln\left(\frac{\langle N\rangle^2}{\sqrt{S^2+\langle N\rangle^2}}\right) \tag{5.6}$$

$$\sigma^2 = \ln\left(\frac{S^2}{\langle N\rangle}+1\right) \tag{5.7}$$

The average cluster size is marked with $\langle N\rangle$ and S is the corresponding standard error. The values μ and σ are the average and the corresponding standard error for $\ln\langle N\rangle$, respectively.

The maximum of the f(N) function is reached for N_{max}:

$$f'(N_{max}) = 0 \Leftrightarrow N_{max} = \exp(\mu - \sigma^2) \tag{5.8}$$

The relation between $\langle N\rangle$ and N_{max} results after μ and σ are replace with the corresponding values (see equations 5.6 and 5.7):

$$\frac{\langle N\rangle}{N_{max}} = \left(\frac{S^2}{\langle N\rangle^2}+1\right)^{\frac{3}{2}} \tag{5.9}$$

The standard deviation S was kept fix, $S = \frac{1}{2}\langle N\rangle$

In case of pure Ar clusters produced with a conical nozzle cooled at 77K and a stagnation pressure p_0=45 mbar the mass spectrum indicates an average size of $\langle N\rangle_{experiment} \approx 140$ atoms/cluster -see **figure 5.2 a**.

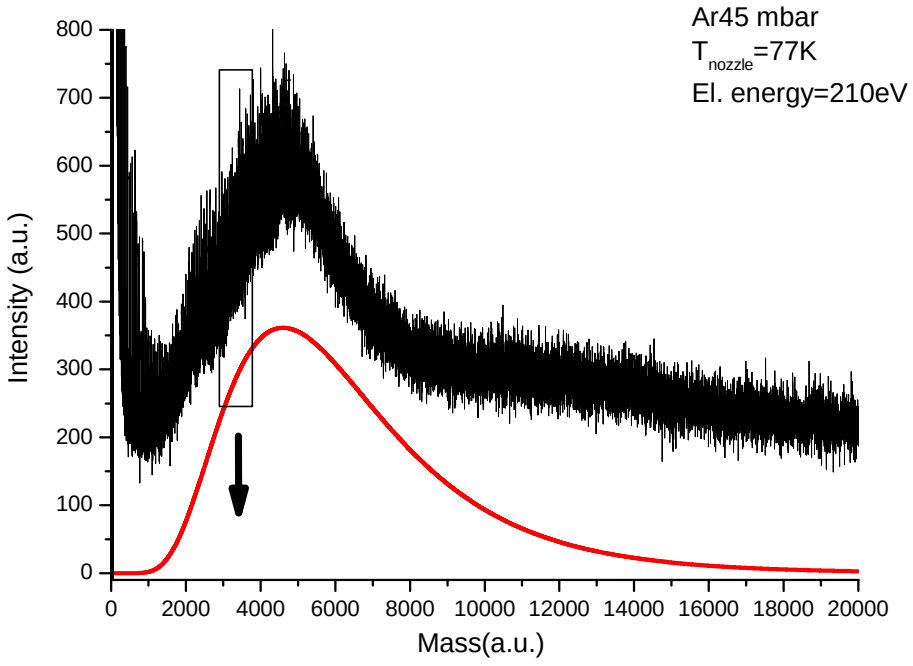

Figure 5.2 a). Mass spectrum of pure Ar clusters with an average size of $\langle N\rangle$ =140. The electron impact energy of the reflectron mass spectrometer is 210 eV.

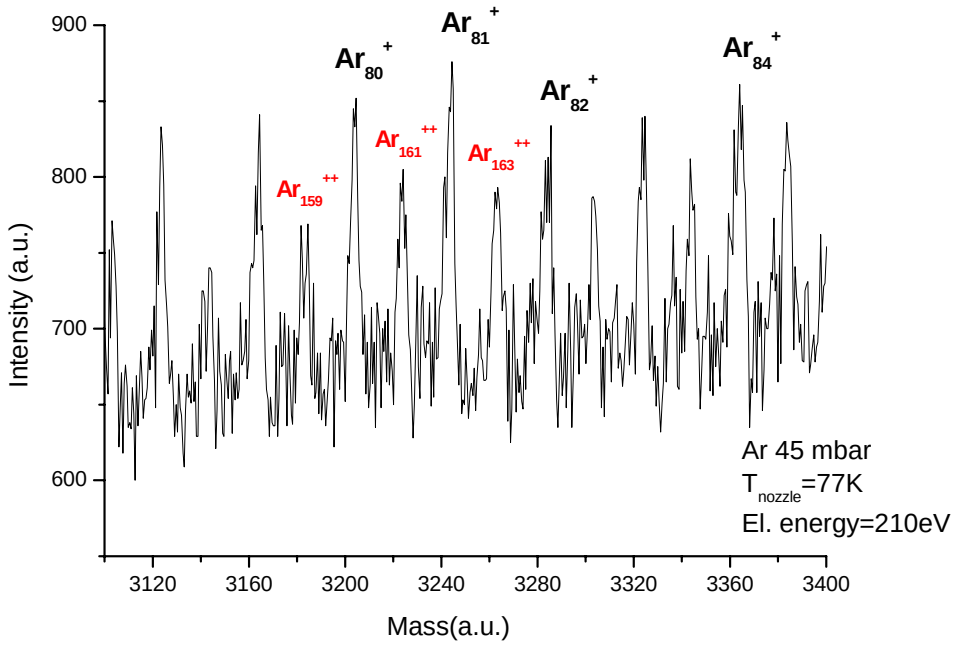

Fig. 5.2 b). A detailed view of the mass spectrum. Single and doubly charge Ar clusters are clearly visible.

Due to a rather large energy of the reflectron electron gun (210eV) also doubly charged Ar clusters are detected – **figure 5. 2 b**). The doubly charged Ar clusters with *odd* N are to be found between single charge cluster lines. In case of *even* N, the Ar_N^{++} clusters overlap with the $Ar_{N/2}^{+}$ cluster lines. The theoretical prediction for the previous parameters is done with the help of equation (4) and the result is $\langle N \rangle_{theory} \approx 140$ atoms/clusters. This means that there is a very good agreement between experiment and theory. Due to a relatively low pressure in the experimental setup, the rare gas clusters travel the whole distance between nozzle and mass detector (about 70 cm) suffering only neglectable fragmentation (see **Mach Disc** discussion – [105]). The electron impact ionization that occurs in the mass detector has also a limited effect in case of clusters consisting of more than 80-100 atoms and the mass distribution of neutral and ionized cluster beams are rather similar.
The mass estimation for the Cu clusters is done only experimentally with help of the Reflectron TOF.

The Cu clusters are produced by means of a pick-up technique. The primary Ar cluster beam pass through a skimmer into the oven chamber. The general purpose of the skimmers is to maintain a differential pumping stage. Our experimental setup has 4 skimmers and the results are different pressure for each section of the experimental setup (see **figure 5.1**) during a cluster experiment: cluster source chamber pressure - 10^{-2}-10^{-3} mbar, oven chamber pressure 10^{-4} mbar, prechamber pressure 10^{-7} mbar, main chamber pressure 10^{-7}-10^{-8} mbar and the Reflectron pressure 10^{-7} mbar.

In case of the first skimmer, it is possible to ”select” mainly the condensed, unscattered part of the beam, this means Ar clusters. The crucible is filled with high purity Cu, which is vaporized and then very efficiently captured by the rare gas clusters. First the Cu atoms are stored on the Ar cluster surface. The kinetic energy of the guest atom and the binding energy (E_{ArCu}) is transferred to the host rare gas cluster. The excess of energy is then dissipated by evaporation of an appropriate number of Ar atoms. More detailed discussion on the pick up process and quantitative predictions are given elsewhere [106].

The following condition *(energetic requirement*) has to be filled in order to obtain condensation of the Cu atoms inside the Ar clusters:

$$BE_{ArAr} < BE_{ArCu} < BE_{CuCu} \tag{5.10}$$

where BE_{ArAr} , BE_{ArCu} and BE_{CuCu} are the binding energies between Ar-Ar, Ar-Cu and Cu-Cu atoms respectively. According to Radzig and Smirnov [107] the dissociation energies for Ar and Cu free dimers are DE_{ArAr}=0.010 eV and DE_{CuCu}=2.0 eV, respectively. The dissociation energy for Ar-Cu^+ was found to be $DE_{ArCu}{}^+$=0.49 eV [108].

Since in the real case the guest Cu atoms have to be loaded inside Ar clusters, one would expect that the binding energy per rare gas atom inside cluster is different from the dimer value of 0.005 eV.

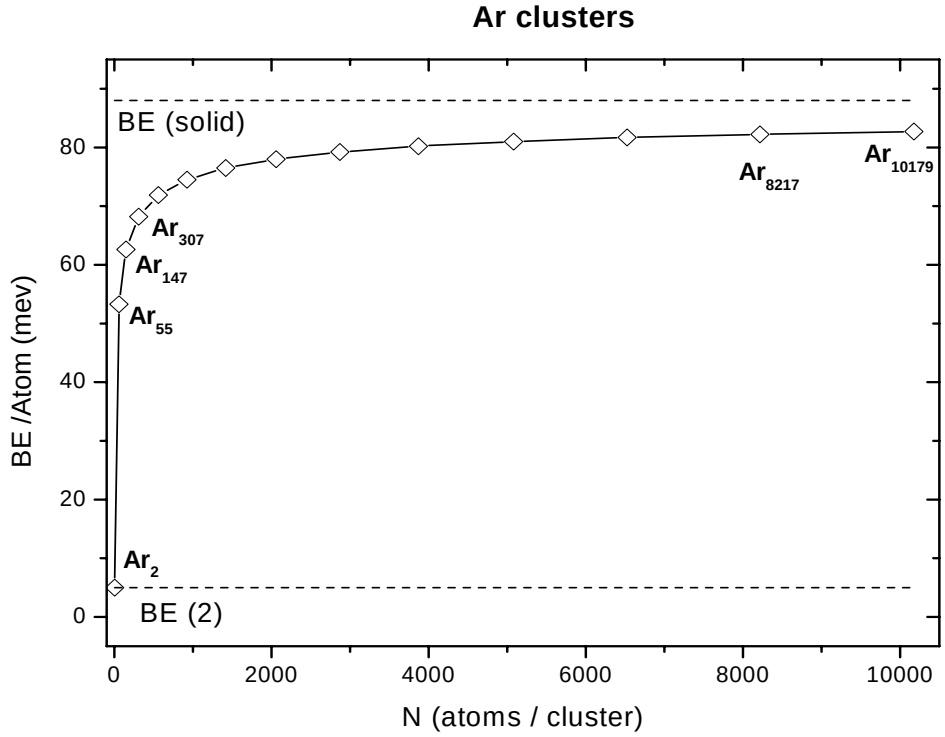

Figure 5.3. Binding energy per atom in case Ar clusters; the values are given as function of rage gas cluster size considering the calculation of Xie [110]. For comparison, the values for solid Ar, BE(solid)=88.8 meV [109] and Ar dimer, BE(2)=5meV [107] are also plotted.

Xie et al investigated the structure and the total binding energy of Ar clusters [110]. Comparative calculation of the of the binding energy per Ar atom inside the rare gas clusters for closed shell ic (icosahedral) and fcc (face centered cube) structures were done assuming Lennard-Jones and Aziz-Chen interaction potentials. Ar clusters up to 13 shells (8217atoms) are more stable in IC geometric configuration and the corresponding values of the binding energies per atom are plotted in **figure 5.3**.

One can see that for cluster containing around 250 Ar atoms (size that is representative for the present investigation), the requirements of the **5.10** relation, are filled.
Another important aspect is also the *geometric requirement*. The "diameter" of the guest atom should be smaller that the one of the host rare gas atom. Typically, the bulk near neighbor distance of the element of interest is taken into account, but it may result in a slightly different size values than for atoms, molecules and clusters. The bond length for bulk Ar is $d_{Ar\ bulk}$=3.75 Å while the dimmer Ar_2 value is slightly smaller $d_{Ar\ dimer}$=3.65 Å. The "diameter" of the Cu atom derived from the bulk consideration is $d_{Cu\ bulk}$=2.56 Å [111]. Bond length value for the Cu dimmer embedded inside Ar matrix $d_{Cu\ dimer}$=2.23 Å is given by Montano [90]. Considering the previous displayed values one may assume that also the geometric factors are in the right relation.
The conclusion is that from theoretical point of view the Cu atoms should be efficiently picked up by the Ar clusters.

5.2 Mass spectra and deposition of Cu clusters

Let's consider that the cluster source parameters for having Ar clusters are filled.
With the help of the time of flight mass spectrometer, Cu clusters are measured for oven temperatures in the range of 1190-1310 C°. For this temperature regime, due to the presence of Ar clusters one might conclude that Cu clusters are protected with an Ar shell. If the oven temperature is lower than 1190 C° only pure Ar clusters are detected. For temperature slightly higher that 1310 C°, only Cu clusters are measured while for higher regimes the Ar clusters are completely destroyed due to the high vapor pressure of Cu atoms inside the oven.
This means that by simply tuning the cluster source parameters (p_0 and T_0) and the oven temperature T_{oven} , one can prepare different sizes of pure rare gas clusters, Cu/Ar core/shell structures or free Cu clusters.

The mass spectra from **figure 5.4** reveal ionized $Cu_{<N>}^{+}$ with different size distributions. The measured spectra indicate higher stability for Cu clusters with <N> number 7 and 9.

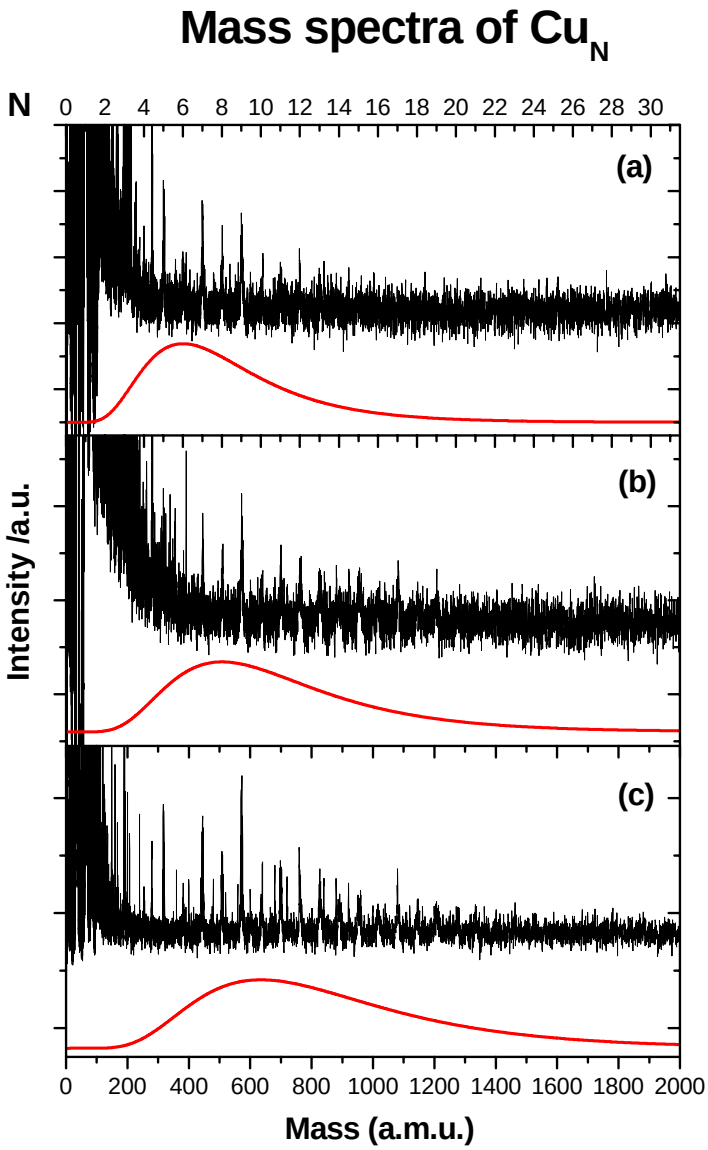

Figure 5.4. Mass spectra of three different Cu cluster size distributions. The cluster source parameters (p_0 and T_0), oven temperature (T_{oven}) and average size ‹N› are display in table 5.1.

Mass spectra	P_0 [mbar]	T_0 [K]	T_{oven} [°C]	‹N› $Cu_{‹N›}$
(a)	66	77	1250	6±3
(b)	66	77	1300	8±4
(c)	99	77	1310	10±5

Table 5.1. Pick up process parameters and average size distribution in case of gas phase Cu clusters.

The lines corresponding to the ionized Ar^+ clusters are also visible. The origin of pure Ar clusters lines might be explained in two different ways: there are Ar clusters of the primary beam that do not pick up Cu atoms when traveling through the oven or the rare gas shell of a Cu /Ar core/shell cluster suffers fragmentation after double (multiple) ionization of the original structure (Coulomb explosion) and the resulting Ar fragments (clusters) are detected.
There are no experimental evidences for doubly charge Cu_N^{++}, Ar_M^{++} or simply charge $(Cu_N /Ar_M)^+$ lines in the mass spectra, but that might be the result of low count rate.
For the further investigations (XPS and XANES) only the average size values will be used (see table 5.1) to make distinction between different cluster size distributions.

The embedded Cu clusters are deposited on a high purity gold foil. The substrate is kept cold (T≈10K) with the help of a liquid He cryostat. The XPS and XANES investigations (see next sections) reveal that in case of pure Ar atoms or clusters deposition, a solid rare gas matrix with *fcc* structure is obtain on the cold substrate (temperature should be less than 25K).

A very important question is what happens with the Cu clusters that have an approximate speed of 300 m/s at the deposition time.
A simple estimation is done for a $Cu_{<10>}$ cluster embedded in a shell of Ar (80 rare gas atoms). The kinetic energy of the cluster was found to be ~3.6 eV. Considering that the original Ar cluster consisted of ~200 atoms and with the help of Xie calculation [110] one can predict the binding energy for the Ar shell of Cu_{10} embedded cluster to be around 65 meV/Ar atom. The impact energy of 3.6 eV is converted in vaporization energy and up to 55 Ar atoms from the protective shell dissociate. If "hot" atoms are evaporated, then the previous estimated number is reduced.
One can conclude that the Ar shell provides protection against fragmentation. The deposited Cu clusters isolated inside the Ar matrix (temperature T=10K) are well protected against diffusion or aggregation.

5.3 X-ray photoelectron spectroscopy investigation

The aim of the XPS measurements was to give a qualitative description for the chemical structure of thin films deposited on the sample surface. The excitation energy was tuned in the range of 215.5-1047.5 eV and that correspond to rather bulk sensitive regime (few tens of Å)-if consider Cu 3p and Ar 3p core level lines.

Since the copper clusters are deposited on gold coated copper sample holders a natural question is if the sample holder coating (Au coating) is thick enough to screen the signal from the Cu core.
From all sample holders measured prior the cluster deposition only one displayed low intensity Cu signal and was considered as not suitable for deposition.

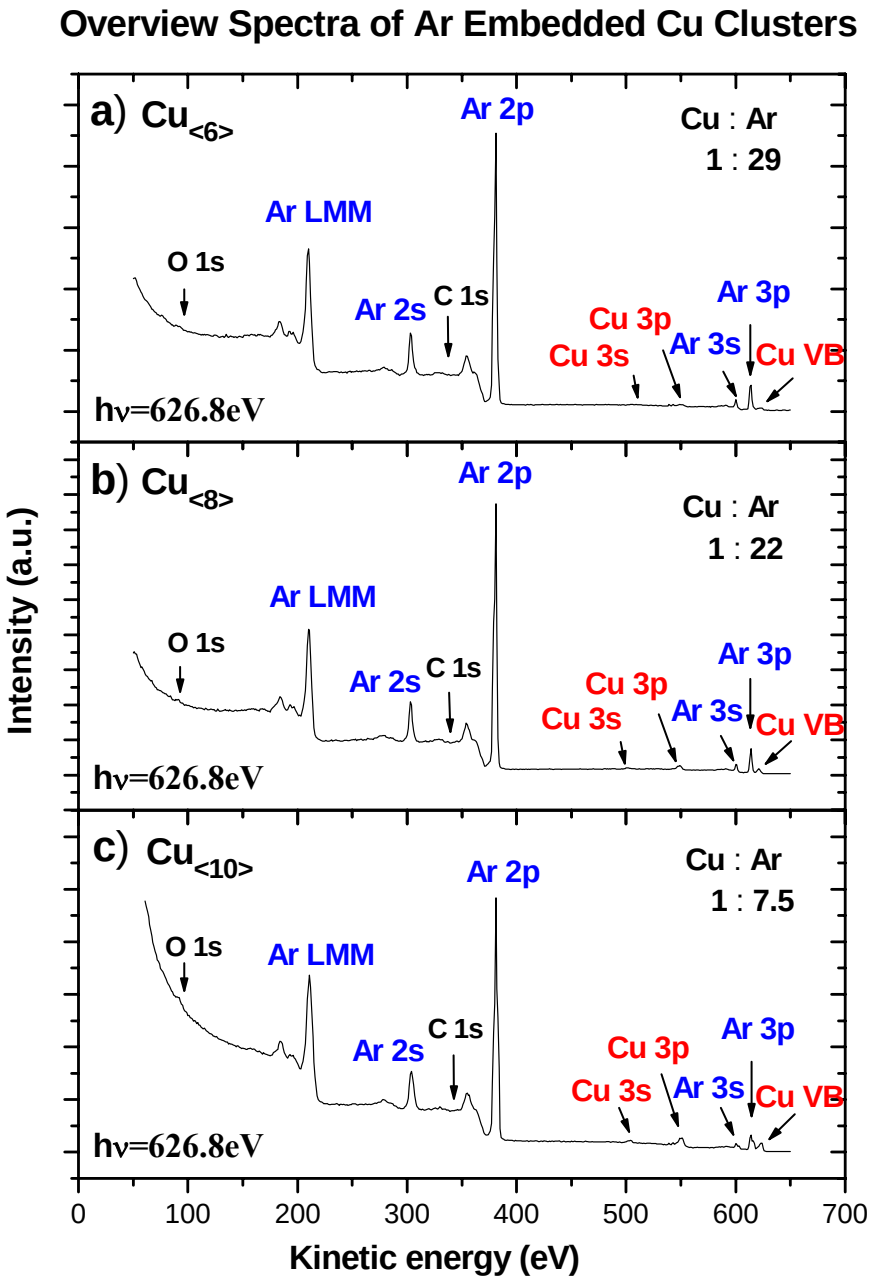

Figure 5.5. EDC spectra of size selected Cu clusters recorded with the same excitation energy, hν = 626.8 eV. There is no significant oxygen or carbon contamination. The graph a) corresponds to $Cu_{<6>}$ embedded clusters, b) and c) characterized $Cu_{<8>}$ and $Cu_{<10>}$ metallic clusters, respectively. The Cu : Ar atomic ratios for all three samples are also displayed.

The overview spectra for different Cu cluster sizes embedded in Ar were recorded few minutes after the deposition on the substrate cooled down at 10K (**figure 5.5**). There is no indication of sample contamination the only contributions come from the Cu and Ar core level lines. The excitation energy was 626.8 eV for all three samples.

The Cu : Ar atomic ratios were determined by considering the Ar 2p and Cu 3p core level line intensities and the corresponding photoionization cross sections. The $Cu_{<6>}$ sample has Cu : Ar a ratio of 1 : 29 (see **figure 5.5 a**), for the $Cu_{<8>}$ clusters the atomic ratio is 1 : 22 (**figure 5.5 b**) and the lowest ratio Cu : Ar with a value of 1 : 7.5 corresponds to the $Cu_{<10>}$ sample (**figure 5.5 c**).

The stability and homogeneity of the $Cu_{<8>}$ cold deposited clusters (the same sample) are monitored in **figure 5.6**.

Comparison between fresh deposited sample (**5.6 a**) and two hours latter investigation (**5.6 b**) with the same excitation energy hν = 626.8 eV indicated that there are negligible differences of the sample structure upon time (see O 1s line).

The depth homogeneity of the $Cu_{<8>}$ sample is confirmed by the overview spectrum recorded with the excitation energy of hν = 1047.5 eV (**5.6 c**). The estimated Cu : Ar atomic ratio of 1 : 21 is in agreement with the value of 1 : 22 derived from the 626.8 eV survey spectrum.

It is important to clear one aspect: both EDC spectra are recorded with excitation energies that correspond to a rather bulk sensitive regime (see 3.1 section). According to the "universal curve" for the escape depth of the photoelectrons the mean free path is in the range of 15 and 50 Å for photoelectron kinetic energies of 550 and 950 eV, respectively. For the topmost layers one might expect a rather different Cu : Ar ratio, with enhancement of the Ar contribution. The explanation: the pressure in the main (deposition) chamber before deposition was typically 10^{-9} – 10^{-10} mbar, but during the cluster deposition the pressure in the main chamber raises up to a value of 2×10^{-8} mbar. The increase in pressure is obviously due to the incoming Ar atoms (and clusters) that do not stick to the cold substrate and are scattered in the deposition chamber, increasing the background pressure. The pumping power of the main chamber is capable to drop the pressure in the original 10^{-9} – 10^{-10} mbar regime few seconds after the deposition finishes and one can admitted that a reduce amount of Ar atoms sticks to the sample surface after cluster deposition.

All Ar embedded Cu clusters samples that are deposited on the cold sample holder (T<10K) were carefully monitored each moment of the spectroscopic investigation. Modifications of the sample holder temperature and main chamber pressure are rather low during the exposure to the synchrotron radiation.

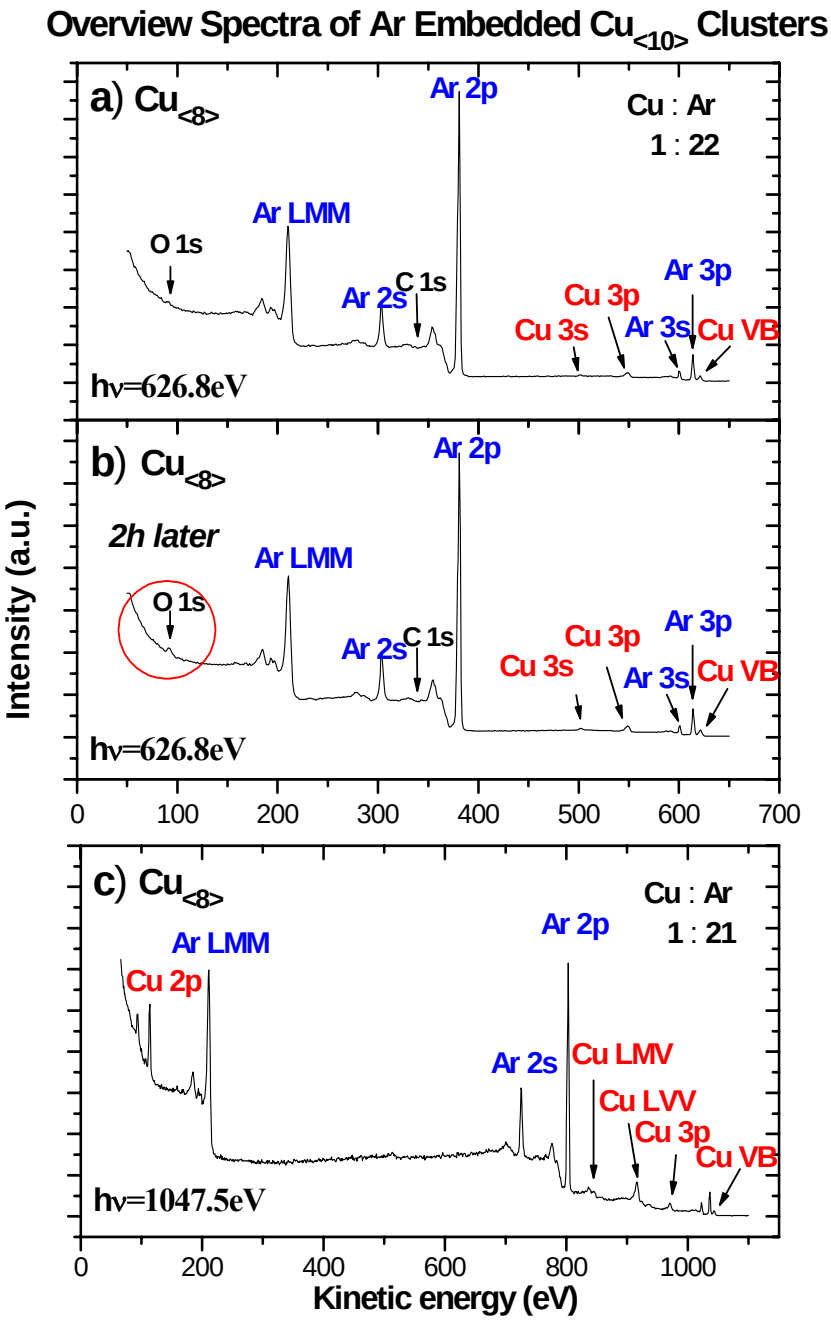

Figure 5.6. Survey spectra of the $Cu_{<8>}$ sample. a) few minutes and b) 2 hours after the cluster deposition, the excitation energy being the same hν=626,8. c) few minutes after cluster deposition, the excitation energy being hν=1047.5

If the sample holder temperature is raised rapidly at values higher than T=40K, the main chamber background pressure increases dramatically to values in the 10^{-4} mbar range. The Ar atoms evaporate and a thin Cu film results on the gold coated sample holder (see **figure 5.7**). In case the sample holder

is rapidly cooled down again from T=40K to a temperature T<10K the thin Cu film is rapidly covered by a thick (more than 60 Å) layer of Ar. The XPS and absorption (Auger spectra) measurements correspond to a Cu free Ar matrix [112]. For more information about the absorption measurements on pure Ar matrix, see next section.

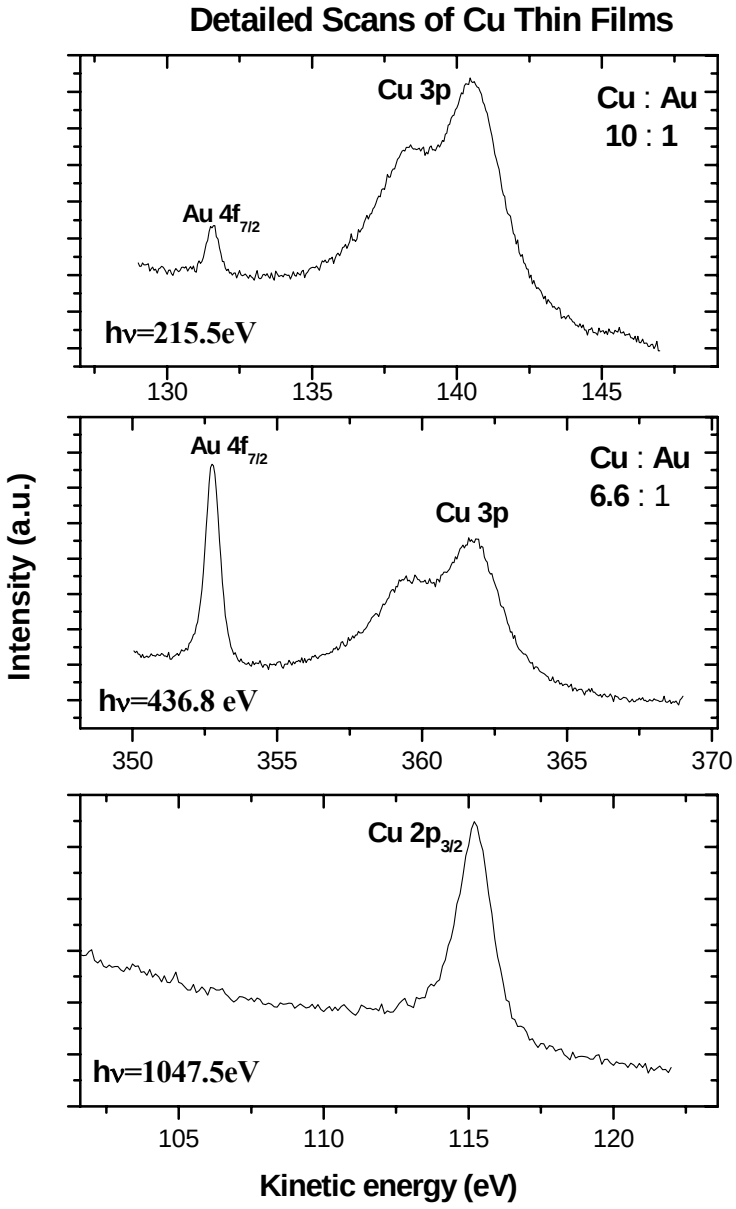

Figure 5.7. Detailed scans of the Cu 2p and 3p core levels corresponding to the Cu thin film at room temperature.

The photoelectron spectra displayed in **figure 5.7** correspond to Cu thin films that result after the sample holder has reached the room temperature. As expected, the Cu : Au ratio decreases with the

increase of the excitation energy – **figure 5.7 a)** and **5.7 b)**. The photoelectrons with higher kinetic energy are able to escape from large depths (see *photoelectron escape curve*) and the signal corresponds mainly to the sample holder Au atoms.

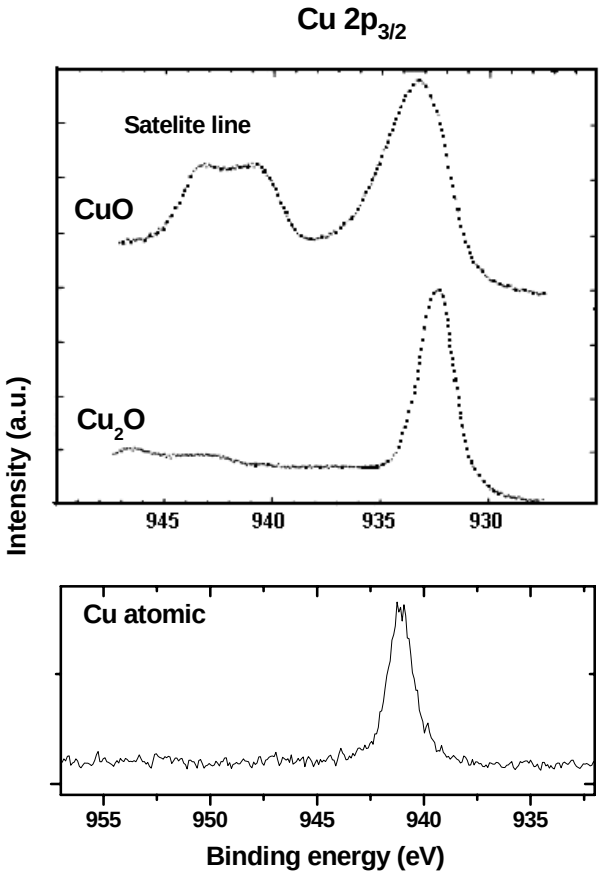

Figure 5.8. The experimental Cu $_{2p\ 3/2}$ photoelectron spectra of CuO, Cu_2O and Cu atomic samples. The data for copper oxides are taken from [113] and for atomic copper from [114]. The CuO spectrum poses a strong multiplet splitting feature at about 9 eV-higher binding energy.

For comparison, the Cu 2p $_{3/2}$ spectra of copper oxides and atomic copper are displayed in **figure 5.8**. The large satellite (multiplet splitting) of the CuO sample and the broadening of the main peak give a clear and direct indication of oxidation level for any copper sample. Also the chemical shift is significant large, 0.9 eV lower binding energy [113].

The conclusion is that even without a rare gas protective shell, the amount of oxidation in case of "warm" samples is still a low one. There are no traces of CuO oxides [113, 115], but the amount of Cu_2O oxides cannot be precisely predicted due to a very low value, 0.1 eV, for the chemical shift [113, 116]. The broadening of the Cu 2p and 3p core level lines is mostly the result of the thin Cu film roughness and the interaction with the Au substrate. The absorption spectra of the warm samples are

very similar with previous investigation on disordered Cu-Au alloys - for more information see section 5.6.

5.4 Absorption spectra

The technique of matrix isolation spectroscopy has made possible the low temperature investigation of atoms [117, 118], molecules and small clusters [18]. Considering the space needed to accommodate the atoms, one can compare the estimated atomic diameters of the guest atoms with the nearest neighbor distances of several sites in the host lattices. It looks like atomic Cu substitutes only one Ar atom from the fcc rare gas matrix (corner atom). Investigation on $Cu^{+}Rg_n$ (Rg=Ne, Ar) indicates high probability of $CuAr_6$ with octahedral structure [108].

5.4.1. The Ar XANES

As part of the preparative measurements Ar clusters are deposited on the gold painted sample holder cooled down at 8K. The deposited Ar clusters form Ar multilayers on the sample holder surface. The recorded absorption spectra, bulk sensitive TEY and the surface sensitive Auger yield displayed in **figure 5.9** agree with the published data on Ar multilayers (fcc structure) [112].

There are remarkable changes of the $L_{3,2}$ edge XANES shape from Ar gas phase to free clusters or solid Ar [119, 120, 121, 122]. The relationship between the atomic and solid Ar is discussed in detailed by Menzel et al. [112]; the complex *ns* and *nd* Rydberg structure of the Ar atom absorption spectrum [119] transforms into two excitonic lines, which lie 0.9 eV to higher energy than the corresponding *4s* and *3d* Rydberg transitions in the atom.

The surface specific transitions are found to be shifted 0.4 - 0.5 eV to lower energy with respect to the corresponding bulk features [121, 122]. A forbidden transition to the *4p* level is also enhanced in the more surface sensitive Auger spectrum –see **figure 5.9 a**).

As expected, the surface sensitivity is higher for the Auger absorption spectra. In **figure 5.9 b**), one can distinguish a low intensity surface contribution at the peak (feature) corresponding to the $2p_{3/2} \rightarrow 4s$ transition.

If the Ar atom spectra are dominated by $2p_{3/2,1/2} \rightarrow ns$, *nd* Rydberg transitions below the ionization potential and obviously with no shape resonance in the continuum, the small Ar clusters show excitonic features below the continuum threshold and shape resonance structures in the continuum [121, 122]. The evolution of the absorption features from Ar atoms to large cluster has been carefully investigated; the Ar_{750} clusters or larger display a solid like XANES curve [121].

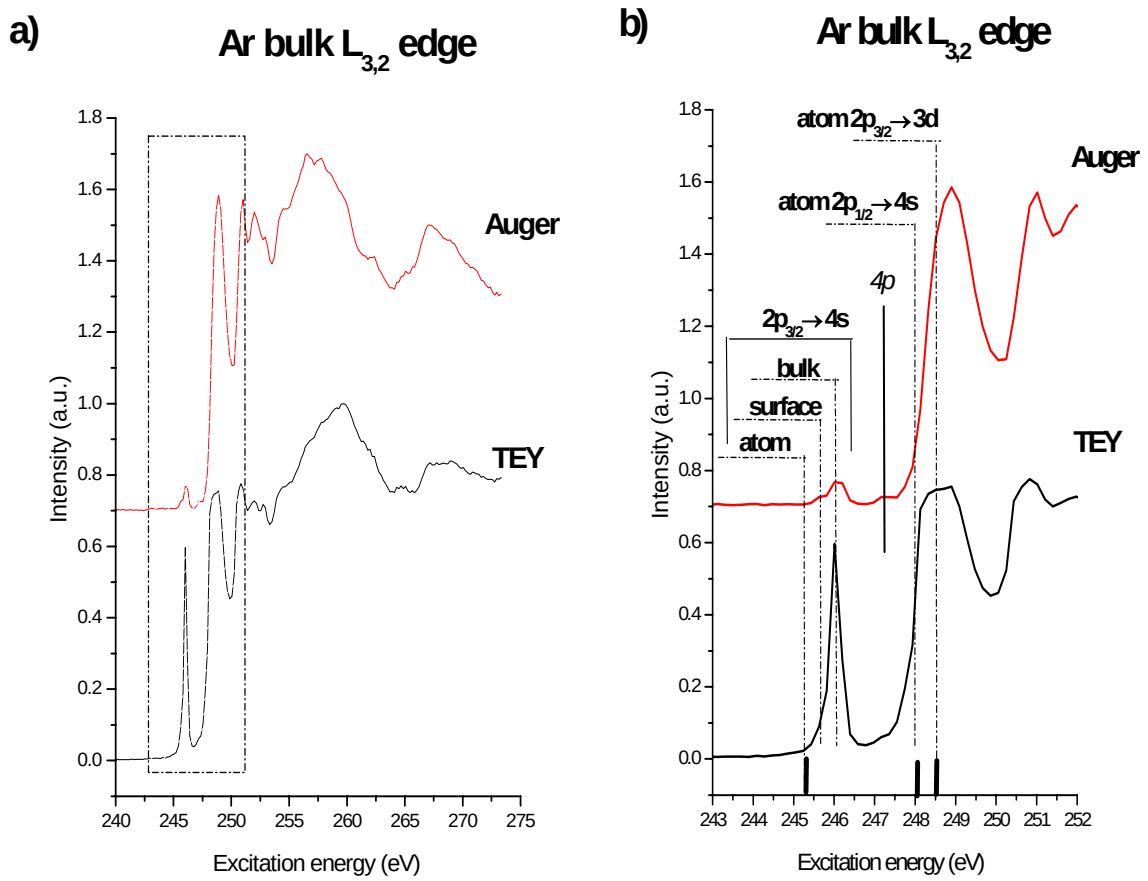

Figure 5.9. a) Comparison of the Auger and TEY XANES curves corresponding to Ar $L_{3,2}$ edge of a bulk Ar matrix (fcc structure). b) Detailed view of the absorption spectra indicating the position of the atomic, surface and bulk contribution.

The absorption spectra of pure Ar matrices (TEY and Auger) are compared with the ones doped with small Cu clusters-**figure 5.10**. The Cu cluster average sizes are obtained by means of mass spectroscopy and the Cu/Ar ratios by the photoemission spectroscopy following the previous described judgments.

The excitonic part of the spectra shows low influence of the small Cu cluster guest. Instead there is notable difference between the pure Ar matrix and the Cu_{10} doped matrix regarding the geometric structure. The shape resonance (multi scattering structure MRS) peaks clearly indicate a strong influence of the Cu_{10} guest on the local order of the host rare gas multi-layers.
The XANES structure of Ar $L_{3,2}$ edge is a complex one and the attempts of simulating the Ar absorption spectra (pure ore doped rare gas matrices) by means of multiple scattering techniques were not successful [131].

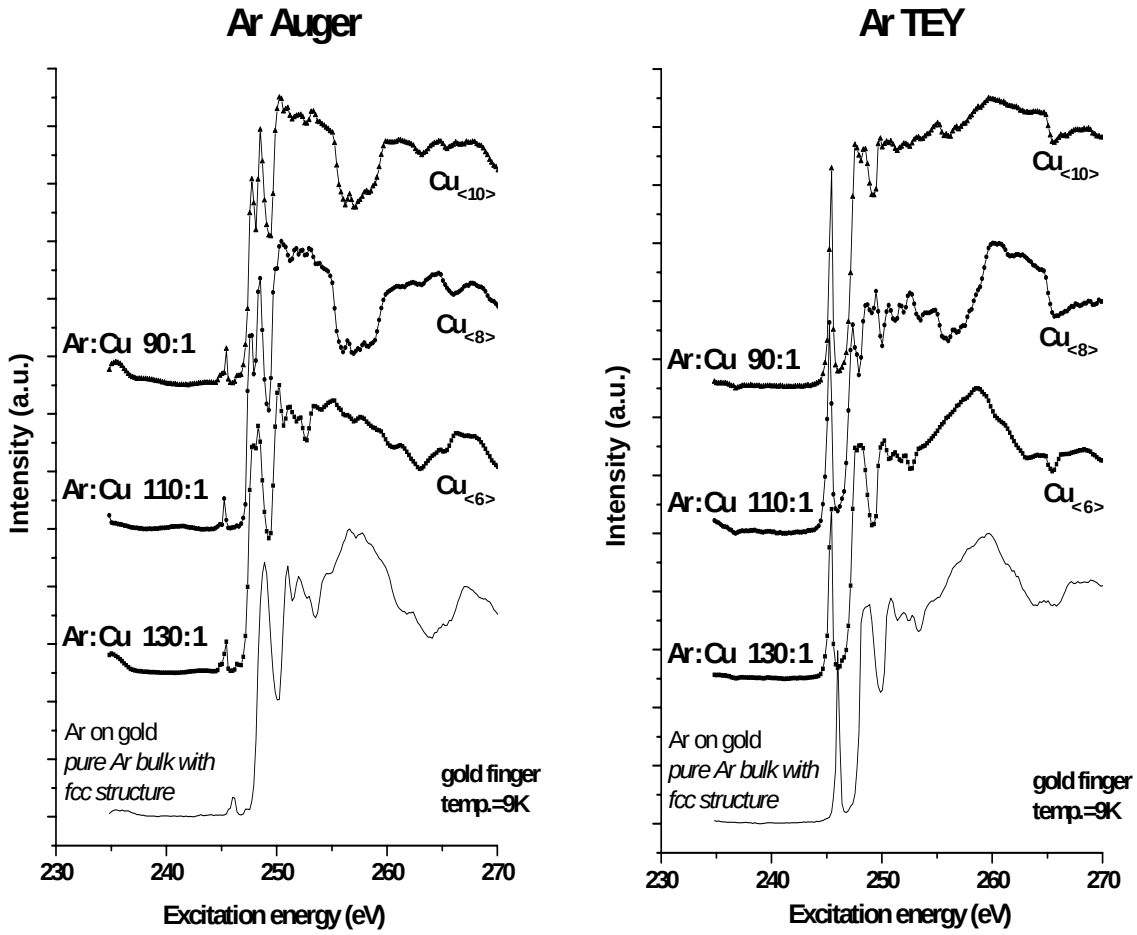

Figure 5.10. Ar $L_{3,2}$ edge XANES spectra, Auger (left) and TEY (right) contributions for pure and Cu cluster doped Ar matrices (substrate temperature-9 K). The average size of the small Cu clusters is also given. The corresponding Ar:Cu ratios are deducted from photoelectron spectra. The doped matrices display no significant modification of the excitonic features relative to the pure one, but there are dramatic changes in case of shape resonance structure.

5.4.2 The Cu XANES

Cu atoms and Cu solid

Techniques like photoemission and X-ray absorption spectroscopy revealed significant changes in the electronic structure of bulk Cu with respect to the atomic Cu. The general accepted electronic configuration of Cu atoms is $[Ar]3d^{10}4s^{1}$, but the same electronic structure could not be applied for Cu metal.

Williams and Lang [123] proposed a simple model of the core-level binding energy shifts in metals relative to the free atom. The measured core-level energies by means of photoelectron spectroscopy agree with the theoretical values that are the sum of relaxation, chemical and configuration shifts. Particularly in case of Cu, the configuration shift reflecting the changes in the electron distributions among s and d states is a dominant contribution. The electronic configuration for solid Cu is $[Ar]3d^{10-x}4s^{1+x}$ like with x=0.4 and this phenomenon is called "*valence change*".

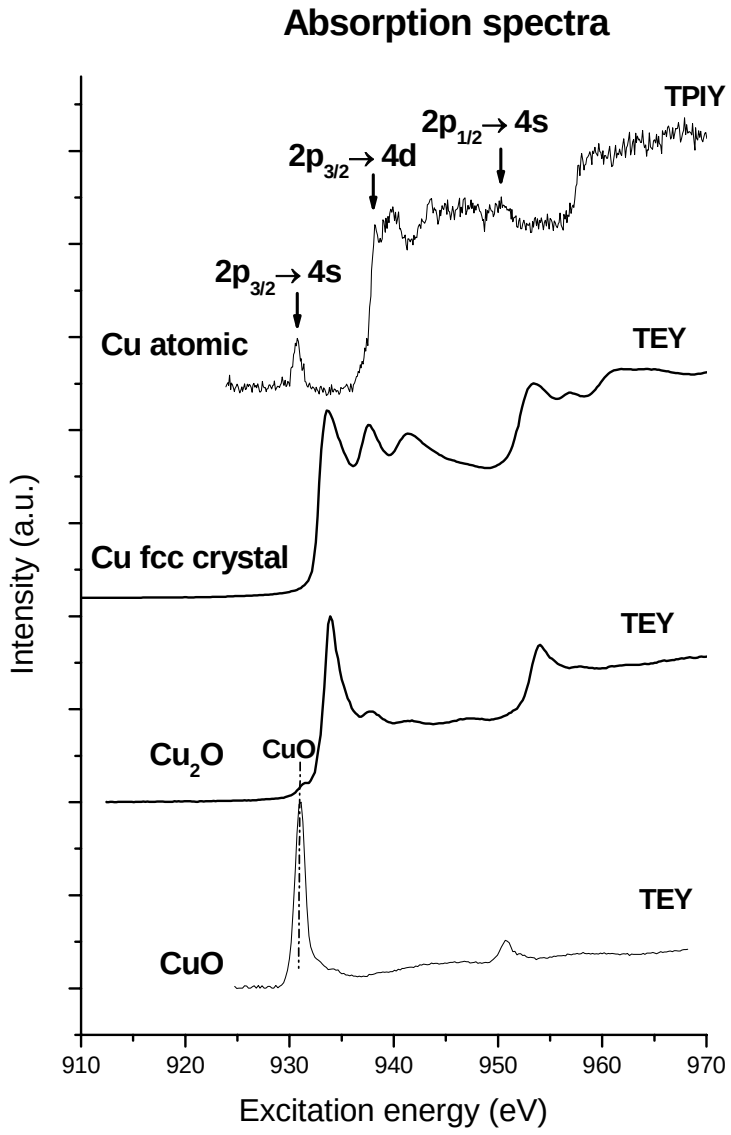

Figure 5.11. XANES data of Cu atomic (TPIY), fcc single crystal (TEY) and Cu oxide (Cu_2O-CuO TEY). The atomic Cu displays a $[Ar]3d^{10}4s^{1}$ electronic structure while the solid samples (Cu single crystal and oxides) have a $[Ar]3d^{10-x}4s^{1+x}$ configuration, with x ~0.4.

Systematic investigation of the Cu electronic configuration (both atom and solid) was performed by Arp et al. [124]. The absorption spectroscopy at the Cu $L_{3,2}$ edge is very sensitive to the number of d- or s-like states and valence modification are easy spotted. This aspect will be explained below.

The **figure 5.11** shows the total photoion yield (TPIY) of the Cu atoms reproduced from the work of Arp [124].

The atomic Cu spectrum display clear features corresponding to $2p_{3/2,\,1/2} \rightarrow$ 4s and 4d transitions, with a spin-orbit splitting of about 20eV. There is no experimental evidence of $2p_{3/2} \rightarrow$ 3d transition, which, according to Cheshnovsky [91] should be visible around 1.5 eV lower excitation energy than the $2p_{3/2} \rightarrow$ 4s absorption feature. The $2p_{3/2,\,1/2} \rightarrow$ 3d excitations would dramatically change the spectrum due to higher probability relative to the $2p_{3/2,\,1/2} \rightarrow$ 4s ones since the radial matrix elements are typically in the following relation: $\langle 2p \,|\, r \,|\, 3d \rangle^2 / \langle 2p \,|\, r \,|\, 4s \rangle^2 \sim 10^2$.

The absence of transitions to 3d states clearly indicates an $[Ar]3d^{10}4s^1$ like electronic configuration for the Cu atoms the ground state (there are no thermal excitations that would display a $[Ar]3d^9 4s^2$ structure).

The other features in the absorption curve are assigned to $2p_{3/2,\,1/2} \rightarrow$ 5s, 4d, 5d transitions or to discrete doubly excited states [124].

The XANES spectrum of the Cu fcc single crystal is plotted in **figure 5.11**. The shape of the spectrum agree with the publish data [124, 125, 126].

Arp et al. [124] concluded that Cu metal has an electronic configuration closer to $[Ar]3d^9 4s^2$, while the other authors, Grioni [125] and Ebert [126], admitted a depopulation of the 3d level and an $[Ar]3d^{10-x}4s^{1+x}$ like electronic structure with x=0.4 and 0.45, respectively. The experimental absorption curve is mainly the result of $2p \rightarrow 3d$ transitions; the s-absorption channel contributes only 5% to the total absorption; this is predominately due to the radial matrix elements that are low for the $2p \rightarrow ns$ transitions. Density of states calculations reveal that L_2 edge spectrum is dominated by the $2p_{1/2} \rightarrow 3d_{3/2}$ (up to 95%) transition while the L_3 edge spectrum is mainly due to the $3d_{5/2}$ (up 90%) absorption channel –see **figure 5.12**; furthermore, the energy dependence of the radial matrix elements strongly enhances the so called "*white*" line at the absorption edge.

The term of "*white*" line originates from the early days of the XAS technique; at that time the X-rays were detected with photographic film and the large absorption peak at the transitions metal L_3 edge appeared as an unexposed "*white*" line on the negative.

Because the overlap of the L_3 with the L_2 edge, the relative peak heights for the later can be read only with some uncertainty from the total spectrum.

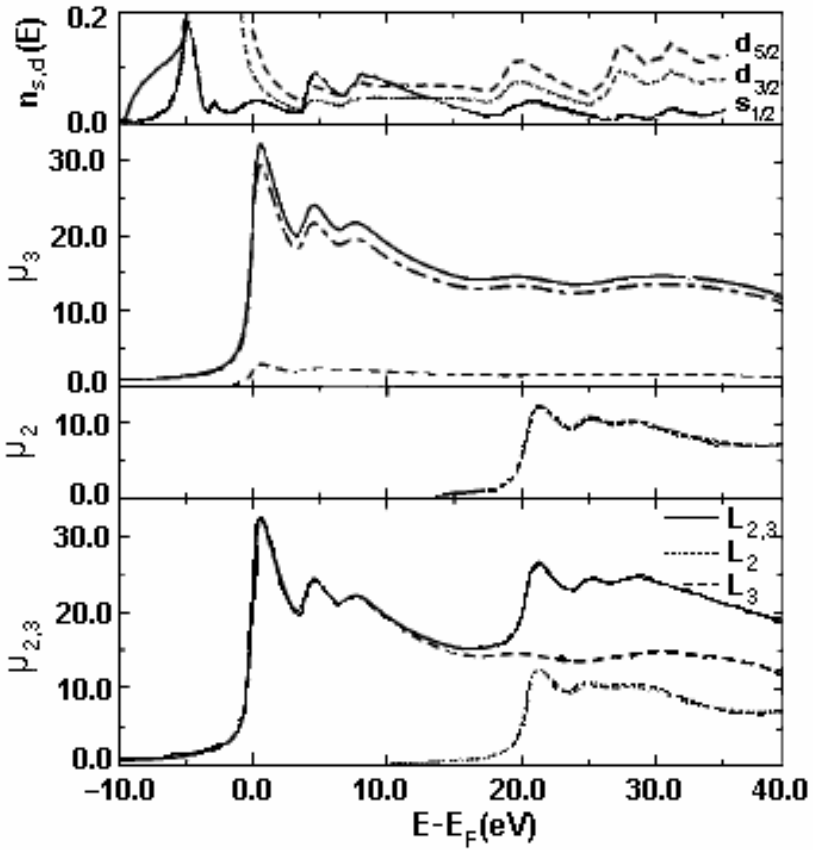

Figure 5.12 The theoretical absorption coefficient $\mu_{3,2}$ for the $L_{3,2}$ edge of Cu. The upper panel gives the $s_{1/2}$, $d_{3/2}$ and $d_{5/2}$ resolved density of states as full, dotted and dashed lines, respectively. The lower panel gives the decomposition of $\mu_{3,2}$ into L_3 and L_2 spectra. The spectra are further decomposed in the middle panels according to final states $4s_{1/2}$, $3d_{3/2}$ and $3d_{5/2}$ character. From [126].

The influence of oxidation on the solid Cu was extensively studied by Grioni et al. [125, 127, 128].

From a theoretical point of view, purely ionic Cu compounds with valence configuration Cu^0 (Cu solid), Cu^I (Cu_2O) and Cu^{II} (CuO) would have the electronic configuration $[Ar]3d^{10}4s^1$, $[Ar]3d^{10}4s^0$ and $[Ar]3d^94s^0$, respectively.

As shown above, the $[Ar]3d^{10}4s^1$ configuration cannot be applied literally to Cu solid (*fcc* single crystal) which has a not completely filled 3d band. Also for Cu_2O and CuO oxides the electronic configuration indicates depletion of the 3d band, but still differences from values expected in a purely ionic model; there are ~9.5 3d electrons and 9.35-9.4 3d electrons per Cu atom in case of Cu_2O and CuO, respectively.

The main absorption channel and contribution in the edge region is the $2p \rightarrow 3d$ transition, similar to the pure Cu crystal case.

The measured absorption spectra are also shown in **figure 5.11**. If the absorption edge of the Cu_2O sample is approximately in the same position like the pure Cu one, the CuO absorption edge is shifted

about 2 eV, lower energy. The sharp contribution at the L_3 absorption edge of CuO originates from the transition 2p → 3d but the effect of the Coulomb interaction between the strongly localized 2p hole and the rather narrow Cu 3d orbital is to localized the excited 3d electron. The final state is a so called "core exciton" and the proof that is not a density of state feature is given by the XPS measurements: the observed peak in the XAS measurement is below the XPS derived binding energy for a CuO sample [[125].

The Cu_2O spectrum exhibits features of both the Cu and CuO spectra. The edge jump is comparable, but smaller that the pure Cu one and feature rich near edge structure was observed.
The experimental results indicate that in bulk Cu samples the XANES curves give information about the degree of oxidation and hence the depletion of the 3d band. For example, one can notice in **figure 5.11** that the Cu_2O sample has also a small amount of Cu^{II} (CuO) contribution.

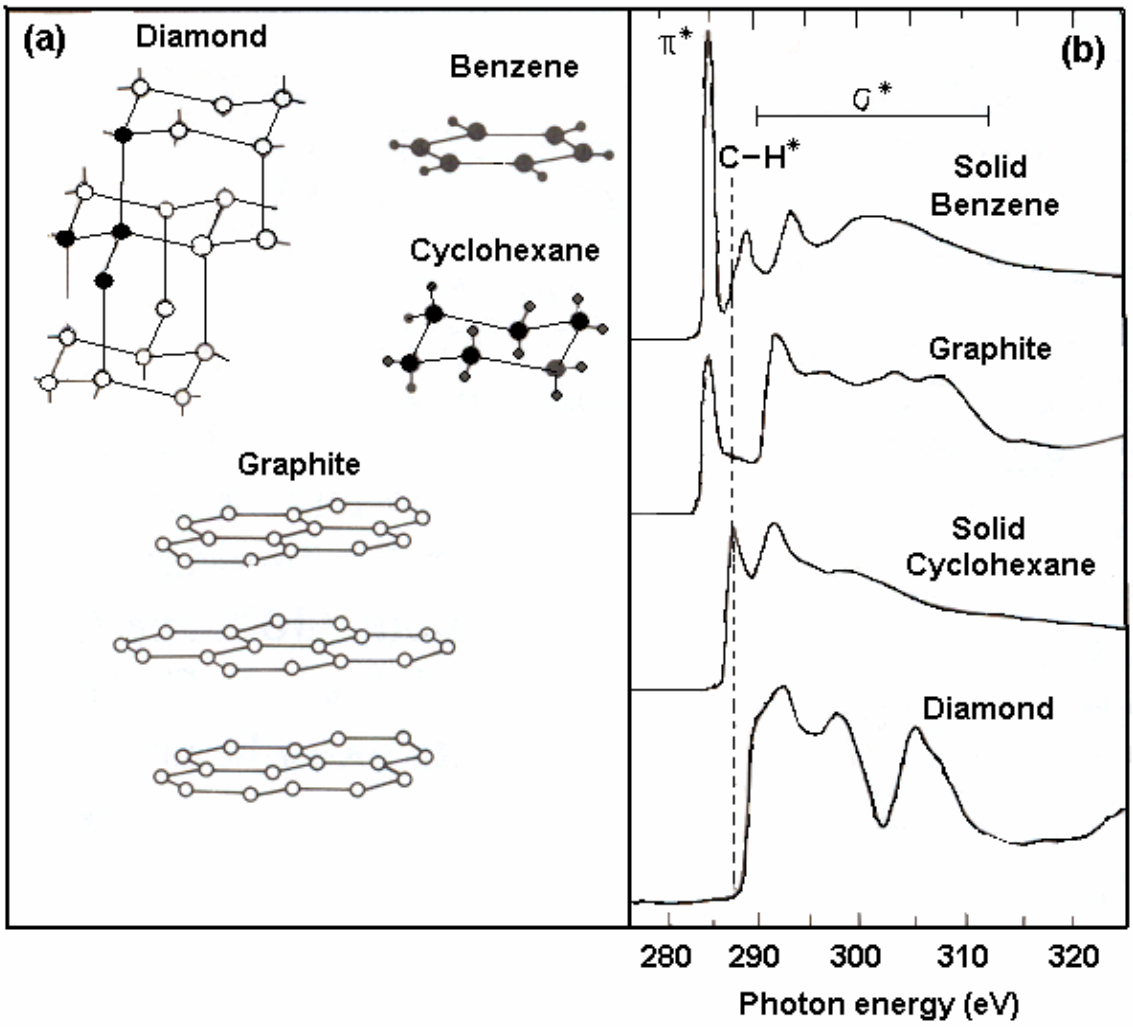

Figure 5.13. a) Structural models for diamond, benzene, cyclohexane and graphite. b) C K-edge XANES spectra of the samples; π*,C-H* and σ* features can be distinguish in the spectra. Modified from [51].

The case of absorption on copper oxides can be understand on the basis of NEXAFS features which are studied in detail for hydrocarbons. The absorption spectra of hydrocarbons give direct access to information regarding the type of bonding. Generally, the C K-edge XANES energy range can be divided into three regions characterized by specific resonance regimes: first π* resonance around 285±1 eV, then C-H* resonance around 288±1 eV and a broad, σ* region between 290 and 310 eV [51].

The C-H* resonance clearly spot the existence of C-H bond in the samples-see the benzene and cyclohexane samples in **figure 5.13**. The σ* region is has a complex structure and will not be discussed here.

The strong π* resonance, the most important feature of the present exemplification, has a sharp peak that can serve as a fingerprint of the local hybridization. The benzene and graphite samples, sp^2 hybridized, have unsaturated carbon bonds as proven by the π*, while cyclohexane and diamond have saturated bonds and sp^3 hybridization.

This means that the π* resonance may be used to distinguish between two forms of carbon from each other.

The general conclusion is that X-ray absorption spectra give a very direct view into the electronic structure of the analyzed samples.

Cu cluster XANES spectra

The investigation of embedded Cu clusters that are deposited on the cold substrate becomes more difficult since the samples are very diluted inside the rare gas matrix (Cu : Ar ~ 1 : 20).

For a better statistic, both **Auger** and **TEY XANES** spectra are recorded simultaneously.

The Auger spectra have the advantage of a better count rate, but for excitation energies in the 916-945 eV range the Cu LVV Auger line overlaps with the Ar 3s and Ar 3p lines-see **figure 5.14 a)**. Also the valence band (VB) features that corresponds to the Au substrate or the Cu clusters is recorded together with the Cu absorption spectrum but, luckily, it doesn't overlap with the absorption edge features. However, the unwanted Ar signal has to be subtracted. For that, an absorption spectrum of pure Ar matrix is recorded for the same energy range. The result of the Auger scan is the collection of photoelectrons that correspond to Ar 3s and Ar 3p lines. The subtracting procedure is sketched in **figure 5.14 b)**:

The TEY spectra do not display unwanted features. However, the measured spectra have lower signal to noise ratio than the corresponding Auger ones. The Auger and TEY Cu $L_{3,2}$ absorption spectra of

embedded Cu clusters with three different size distributions are plotted in **figure 5.15**. The TEY spectra are characterized by a lower count rate than the corresponding Auger spectra, but display the same features labeled A, B and C.

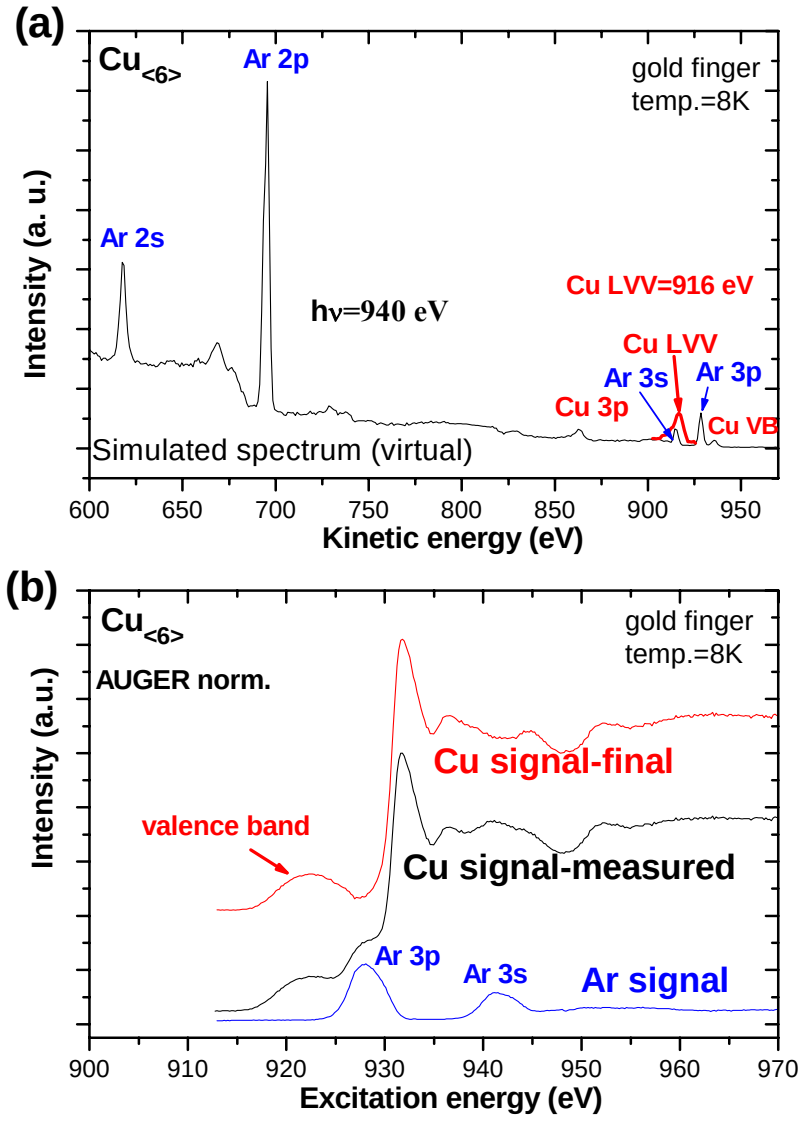

Figure 5.14. a). The survey spectrum of deposited Cu clusters ($Cu_{<6>}$) taken with an excitation energy hν=940 eV. One can clearly see that for excitation energies in the 916-945 eV range the Cu LVV line overlaps with the VB, the Ar 3p and Ar 3s lines. b) The Ar signal is subtracted from the measured Cu spectrum and only the resulting spectrum is investigated.

The count rate is lower for the TEY spectra when compared with the corresponding Auger curves. The Cu : Ar ratio has also significant effect on the count rate when measuring the Cu $L_{3,2}$ edge. The

spectrum of $Cu_{<6>}$ sample with a Cu : Ar ratio of 1:29 has visible lower count rate than the $Cu_{<10>}$ sample with a Cu : Ar ratio of 1:7.5.

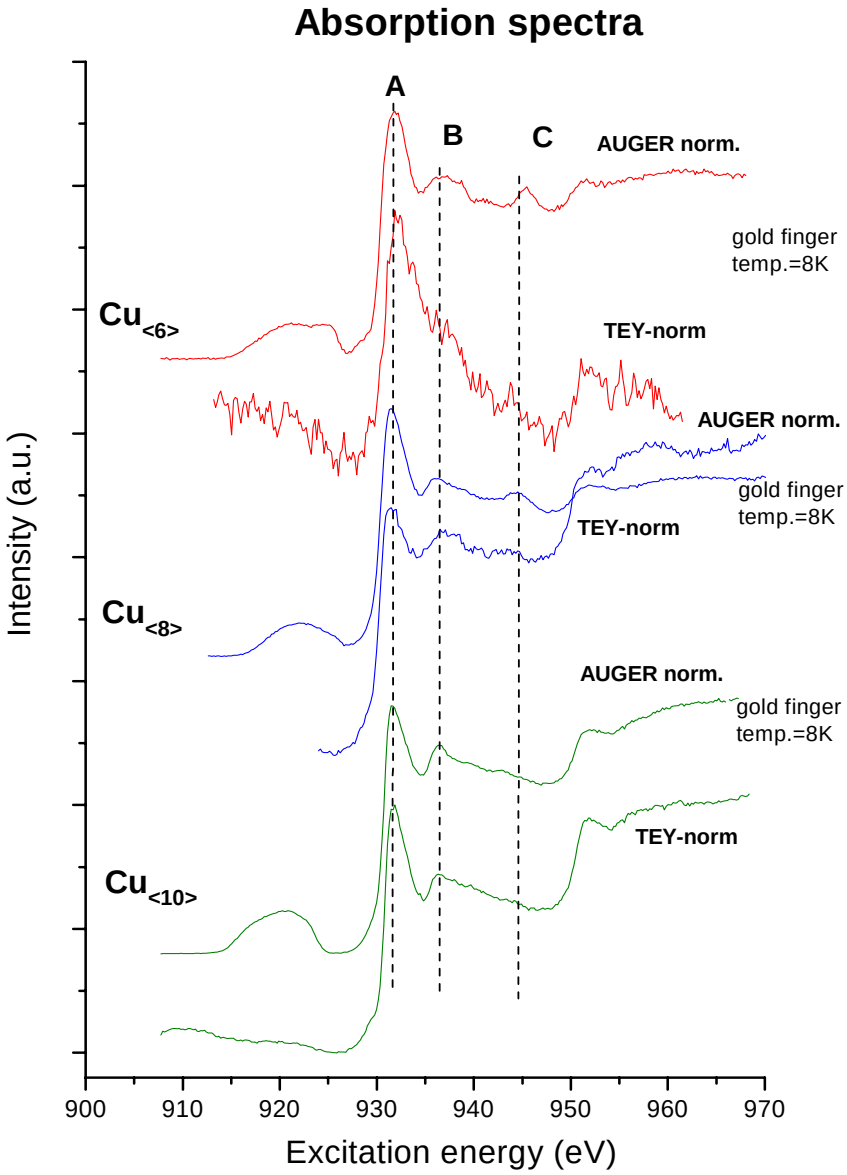

Figure 5.15. The Cu $L_{3,2}$ absorption edge spectra of small copper cluster with average sizes of <6>, <8> and <10> atoms per cluster. The signal to noise is visible lower in case of TEY spectra, but displays the same features, labeled A, B and C, like the Auger curves.

Cu $L_{3,2}$ edge absorption spectra (Auger) of Cu clusters, together with the corresponding absorption spectra of Cu atomic and *fcc* single crystal are displayed in **figure 5.16**.

One can clearly notice that the Cu cluster absorption spectra are very different from the atomic Cu spectrum. The sharp pre-edge feature in the atomic spectrum that corresponds to the $2p_{3/2} \rightarrow 4s$

transition is not to be seen in the XANES spectra (both Auger and TEY) of embedded Cu clusters. All the other discrete transitions that characterize the $L_{3,2}$ edge of the Cu atoms do not have a corresponding feature in any of the cluster absorption curves.

The cluster spectra corresponding to different samples display similar feature due to the fact that the values of the average sizes are closed to each other combined with the broad size distributions.

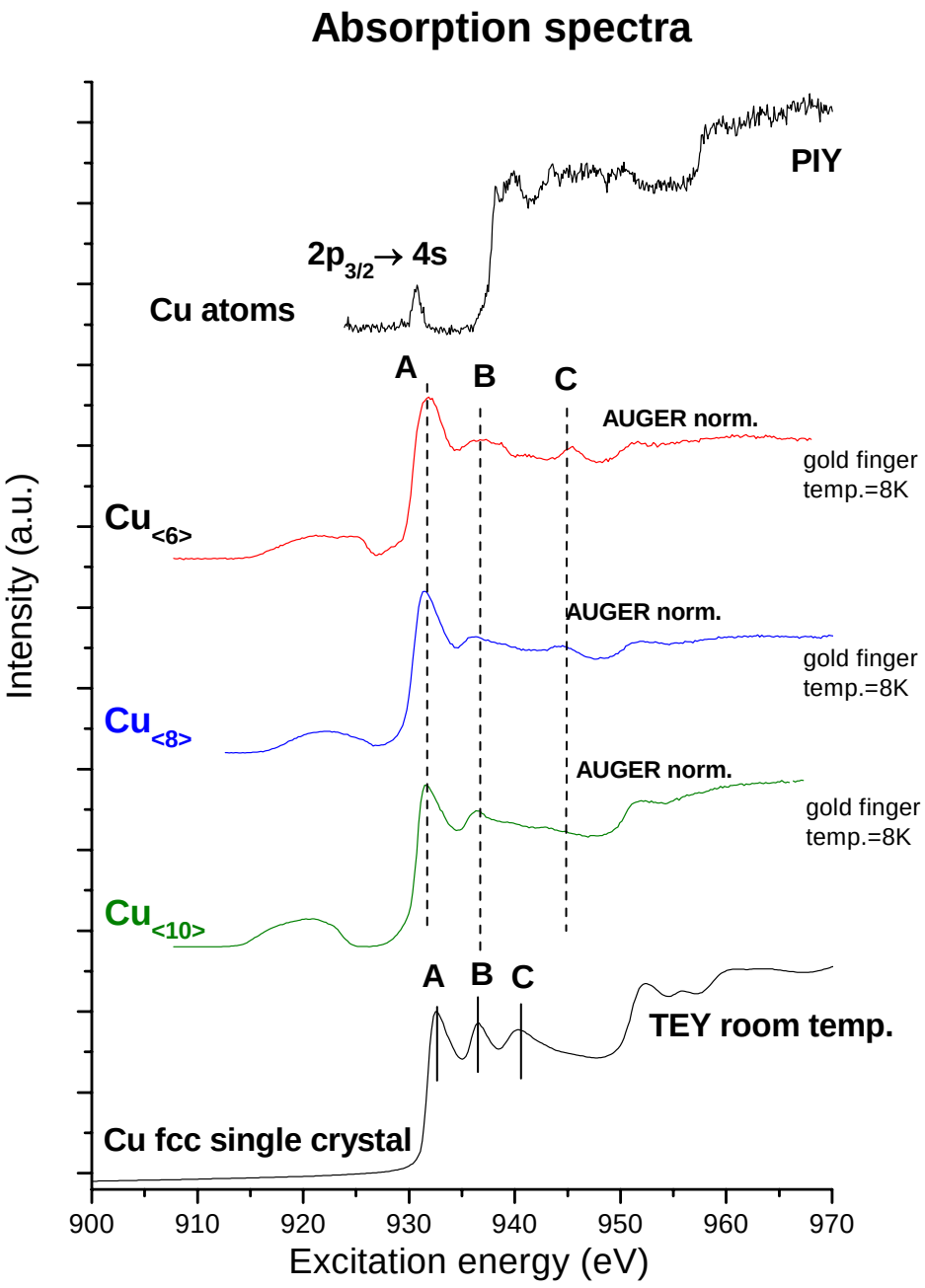

Figure 5.16. Cu $L_{3,2}$ edge absorption spectra (Auger) of copper clusters with three different size distributions; copper atomic and fcc single crystal are also shown. The absorption spectra features of copper clusters are very similar with the ones of copper single crystal and rather different from the copper atomic features.

There are obvious similarities of the cluster curves with the absorption spectrum that correspond to the Cu single crystal. There are exactly the same features labeled A, B and C, that are clearly visible in the bulk Cu L_3 edge spectrum.

The B and C features of the cluster spectra are shifted at higher energies with respect to the absorption edge when compare with the corresponding features of the bulk Cu sample.

It looks like the *valence change* occurs already for cluster sizes smaller than 6 atoms per cluster. This means that the 3d band for small Cu clusters is no more completely filled (as in Cu atoms) and experimental absorption curve is now mainly the result of 2p→3d absorption channel. The electronic structure of the Cu clusters has more similarities with the electronic structure of the Cu bulk.

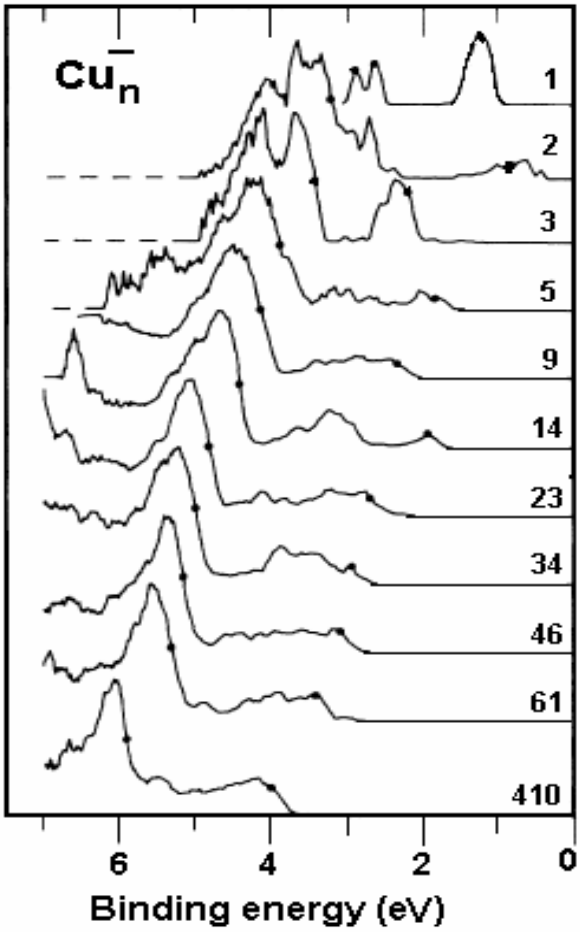

Figure 5.17. The UPS spectra of negative mass selected copper clusters in the 1-410 atoms/cluster size range, taken with excitation energy of 7.9 eV. Significant modification in the valence region occurs already for cluster sizes larger than 5 atoms/cluster. Modified from [91].

The XANES results on small Cu clusters can be compared with Ultraviolet Photoelectron Spectroscopy (UPS) data. Cheshnovsky et al. [91] investigated the evolution of the 3d band in copper

clusters by means of UPS technique. Briefly, the bare unsupported copper clusters were prepared with the help of a laser vaporization source. Negatively charge clusters up to 80 copper atoms were individually mass selected and for larger clusters the accuracy of the mass calibration was sufficient to determine the size of the larger cluster (Cu_{410}^-) to within a few atoms. Using an F_2 excimer laser at 7.9 eV as photon source, the photoelectron spectra were recorded showing the modification of the 3d band structure as function of the cluster size-see **figure 5.17**.

Cluster larger than a few atoms were found to display an increasingly sharp feature at the onset of the 3d band similar to that seen for bulk copper UPS. Already the Cu_5^- cluster display significant modification of the electronic structure when compare with the case of Cu atomic. On the other hand, these data do not allow to obtain a quantitative number for the transfer of d electrons to s states.

5.5 The theoretical simulated spectra. Comparison with the experiment

The multiple scattering resonance theory predicts similar features of the absorption curve for condensed systems having the same geometrical structure but the position of individual peaks is influence by the interatomic distances. Natoli [129] predicted a formula available for distance variations smaller than 20%:

$$(E_r-E_b)R^2=\text{constant} \qquad (5.12)$$

where E_r is the energy position of the peak of interest, E_b is a bound state at the spectrum threshold and R is the interatomic distance. The constant value can be derived from experimental data on well known systems.

In the present case the above formula has to be consider with great care. The reason is that the theoretical prediction for the structure of small Cu clusters (up to 13) suggests different geometry than for the Cu single crystal (fcc structure). For example calculation on Cu_{13} cluster predicted as most probable the icosahedral configuration [130].

The experimental data previous described are compared here with the corresponding theoretical spectra obtained by Soldatov et al. [131]. The theoretical treatment is based on an effective one-electron full multiple scattering theory with final-state potentials including a screened core hole. In particular, the approach uses spherical muffin-tin potentials and many-body effects together with inelastic losses are included in terms of an energy dependent self-energy. This theory is implemented in the *ab initio* XANES and electronic structure code of FEFF8.2 [132].

At the same time, the theory can provide a quantitative relation between the projected electronic density of states (*l*DOS) and the absorption spectra, as well as a physical description of the observed

XANES features [50]. Thus, the treatment encompasses both the excited state and the multiple-scattering path descriptions of X-ray-absorption spectra.

A consistent description of the theoretical approaches to X-ray absorption is given by Rehr [133].

The absorption spectra (both experimental and theoretical curves) are displayed in **figure 5.18**.

Since a sample corresponding to Cu atoms embedded in Ar could not be measured in the frame of the present work, the spectrum of free Cu atoms is compared with the theoretical curved that correspond to unsupported Cu atoms.

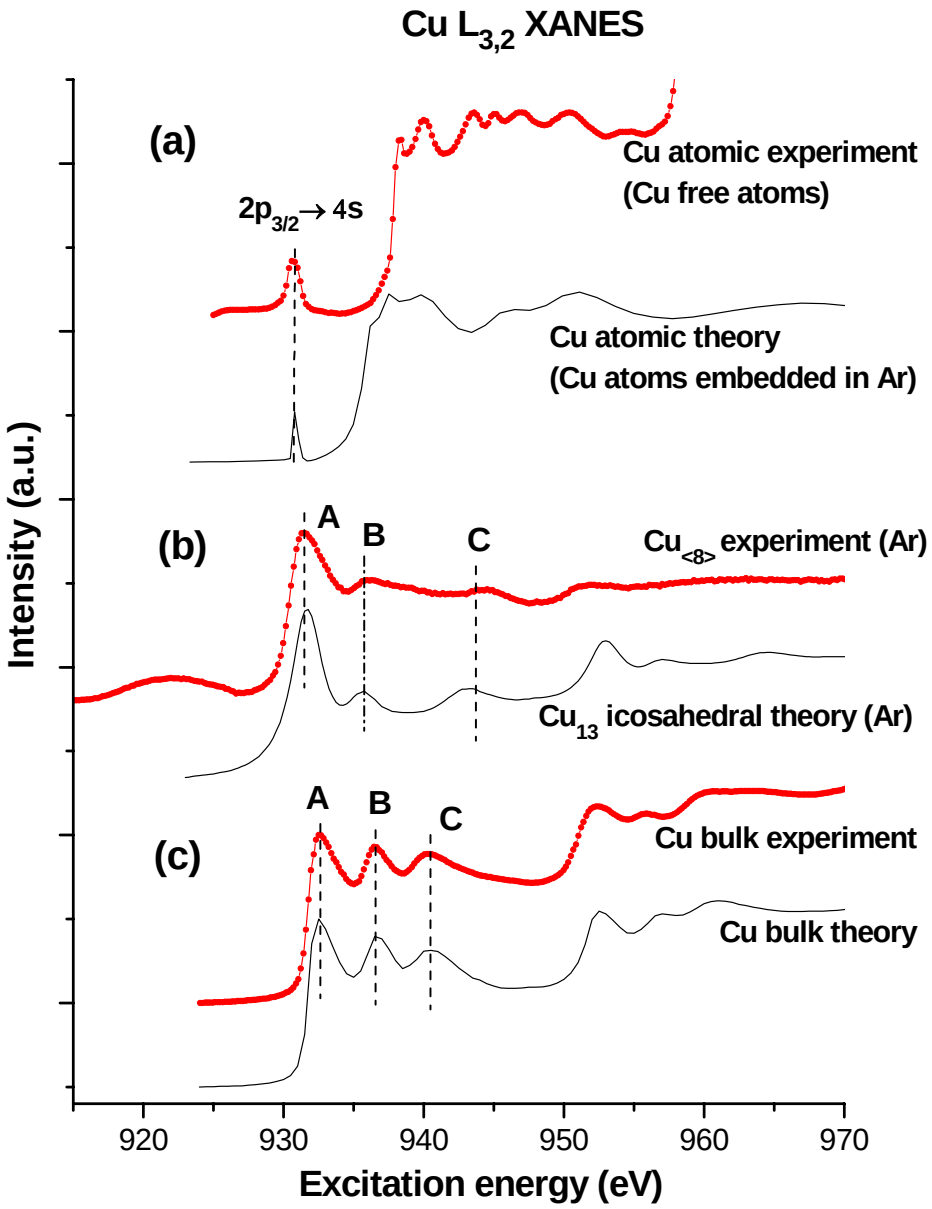

Figure 5.18. Cu $L_{3,2}$ XANES curves of atomic (a), cluster (b) and bulk (c) copper samples. The experimental spectra are marked with dot-dashed lines, the theoretical simulated curves are depicted by continuous lines.

One can clearly see that the simulated curve displays a sharp feature due to the $2p_{3/2} \rightarrow 4s$ transition (like the experimental absorption spectrum of free Cu atoms). However, excepting the previous feature, the two curves display rather different features and this is probably due to the fact that the theoretical spectrum reflects the signal from Cu atoms embedded in an Ar matrix.
Since the $2p_{3/2} \rightarrow 4s$ transition is not present in the absorption spectra of small Cu cluster embedded in Ar, one can conclude that the amount of individual metal atoms is rather low and the rare gas matrix is mainly doped with small Cu clusters.

Further, the measured spectrum of embedded $Cu_{<8>}$ clusters that are deposited on the cold substrate is compared with simulated curves of Cu_{13} cluster surrounded by a rare gas (Ar) shell. Good correlation with the experimental data is achieved for a 13 Cu atoms arranged in icosahedral geometry (**figure 5.19)**. All three feature, labeled A, B and C of the experimental curve have a correspondent peak in the simulated Cu_{13} icosahedral spectrum.

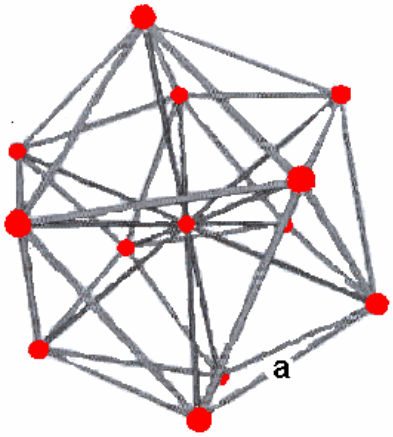

Figure 5.19. a) Atomic arrangement for the Cu_{13} cluster (icosahedral structure)

The simulated curve for the bulk Cu sample is based on the parameters of Cu single crystal: fcc structure and a lattice constant $\mathbf{a}_{bulk} = 2.556$ Å. With the previous assumptions regarding structure and bond length, a theoretical curve is obtained, reflecting clear match with the experimental absorption spectrum of the Cu fcc crystal.

The absorption spectra of $Cu_{<8>}$ sample is compared in **figure 5.20** with the simulated spectra of Cu_{13} cluster of icosahedral (with and without rare gas shell) and fcc (Ar shell) structure, Cu_{55} cluster embedded in Ar, icosahedral and fcc structure.
The atomic distance used by Soldatov for the simulations is $\mathbf{a}_{ico} = 2.416$ Å and this lattice constant for icosahedral structure have been obtained using *ab initio* calculations by the group of Johnston [134].

The value calculated by Lammers [130] is slightly larger, 2.518 Å but corresponds to a *free* Cu_{13} icosahedral cluster.

The *free* Cu_{13} icosahedral cluster with the lattice constant predicted by Johnston is given for comparison. One can notice that the simulated curve of the *Ar embedded* Cu_{13} icosahedral cluster fits better with the experiment, and the feature labeled B is significantly influenced by the presence of a rare gas shell. Without Ar shell the B peak is weaker in intensity-see *free* Cu_{13} icosahedral spectrum.

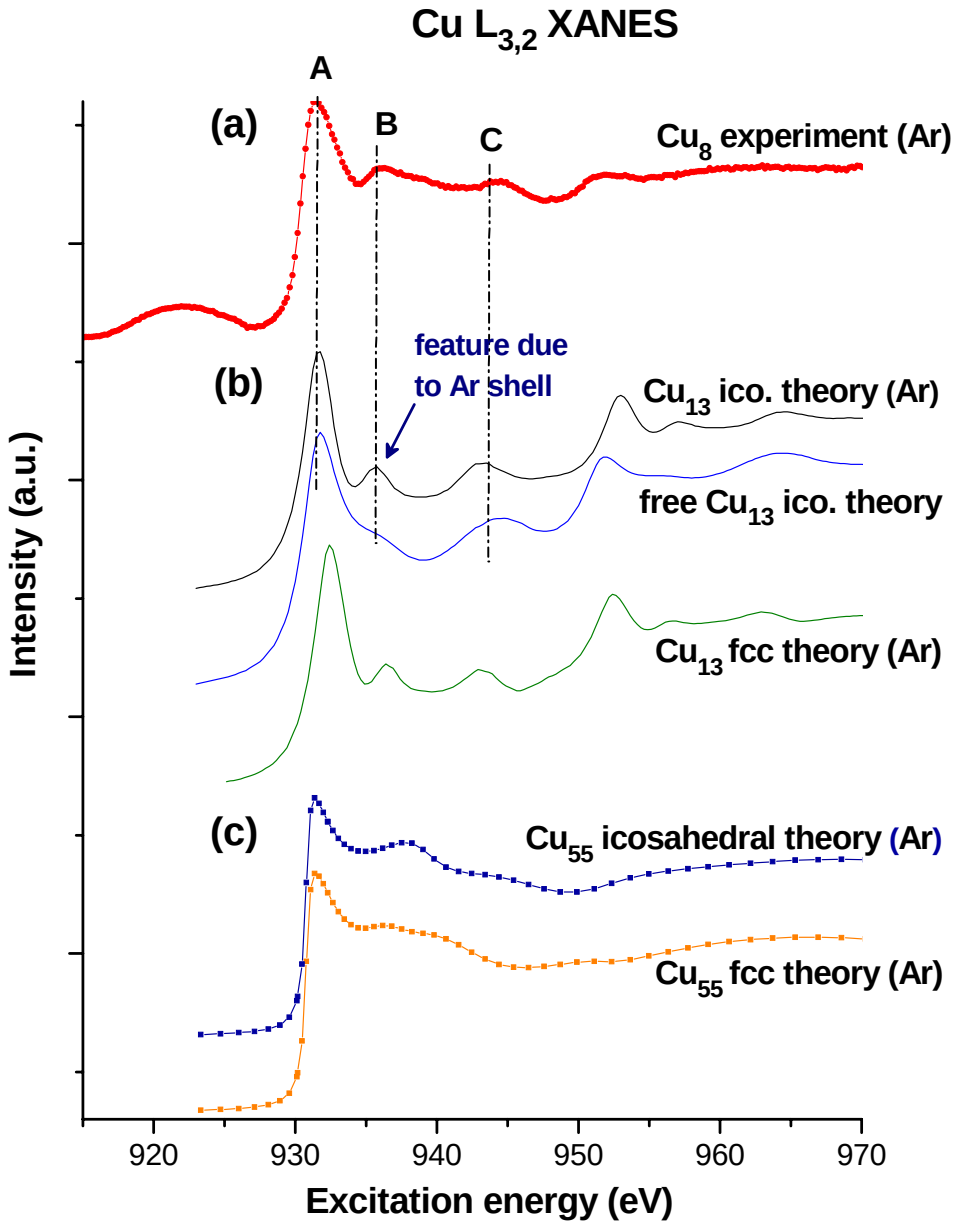

Figure 5.20. Cu L-edge XANES of experimental $Cu_{<8>}$ sample (a), theoretical Cu_{13} cluster fcc and icosahedral (b) and Cu_{55} fcc and icosahedral structure. Only L_3 edge is shown for Cu_{55} clusters, all others have both L_3 and L_2 edges.

A simulated spectrum of Cu_{13} fcc structure inside Ar is shown in the same figure. The shape is very similar with the Ar embedded Cu_{13} icosahedral cluster (the same A, B and C features). The feature C of the simulated spectrum is shifted to higher energy than the corresponding peak of bulk fcc Cu (see **figure 5.18**). According to Natoli's rule a shift to higher energy means that the bond length is reduced. However the simulated spectrum of Cu_{13} fcc structure was obtained with a bond length of the solid copper $\mathbf{a}_{bulk} = 2.556$ Å.

The Cu L_3 edge spectra of simulated Cu_{55} clusters embedded in Ar (both icosahedral and fcc geometry) are also displayed in **figure 5.20**. The two simulated spectra do not fit with the experimental results. This clearly demonstrates that the XANES spectra are rather size sensitive.

It is also interesting to compare the present results with previous investigations. Montano et al. reported the production of small Cu clusters (7 to 15 Å mean diameter) with help of a gas aggregation technique [90]. The small metal clusters were co-deposited with Ar gas on a cold Al substrate (4.2 K) and the geometric structure was investigated by means of EXAFS technique at the K edge. The bond length for copper dimer was found to be $\mathbf{a}_{dimer} = 2.23$ Å, while for cluster having a 7 Å diameter the bond length is already larger than 2.5 Å. For cluster diameter larger than 15 Å, the bond length approaches the bulk value $\mathbf{a}_{bulk} = 2.556$ Å.
Montano concluded that the fcc structure is characteristic for 13 atoms cluster or larger.
However, the present study cannot exclude the fcc geometry, but suggest that the icosahedral structure is more favorable for the Cu_{13} cluster.

5.6 The case of Cu islands on Au substrate

When the substrate temperature raises and the Ar matrix evaporates, the small Cu clusters coagulate on the Au coated sample holder. The corresponding XANES spectra of Cu $L_{3,2}$ edge are plotted in **figure 5.21**. Two samples are investigated corresponding to an original average size estimated to be 6 and 8 Cu atoms /cluster. The oxide contribution is rather low and contributes with a low intensity feature at the $Cu_{<6>}$ spectrum.
The experimental curves presented here are very much in agreement with the Cu-Au policrystalline random alloys reported by T. K. Sham [135]; the disordered alloys presented there consists of three different atomic concentration: Cu_3Au, CuAu and $CuAu_3$.
The spectrum corresponding to warm $Cu_{<6>}$ clusters is similar with the $CuAu_3$ disordered alloy while the present investigated $Cu_{<8>}$ one agrees with the CuAu spectrum. This result is somehow expected,

since the Cu film is very thin and majority of the atoms are in contact with the Au atoms from the substrate.

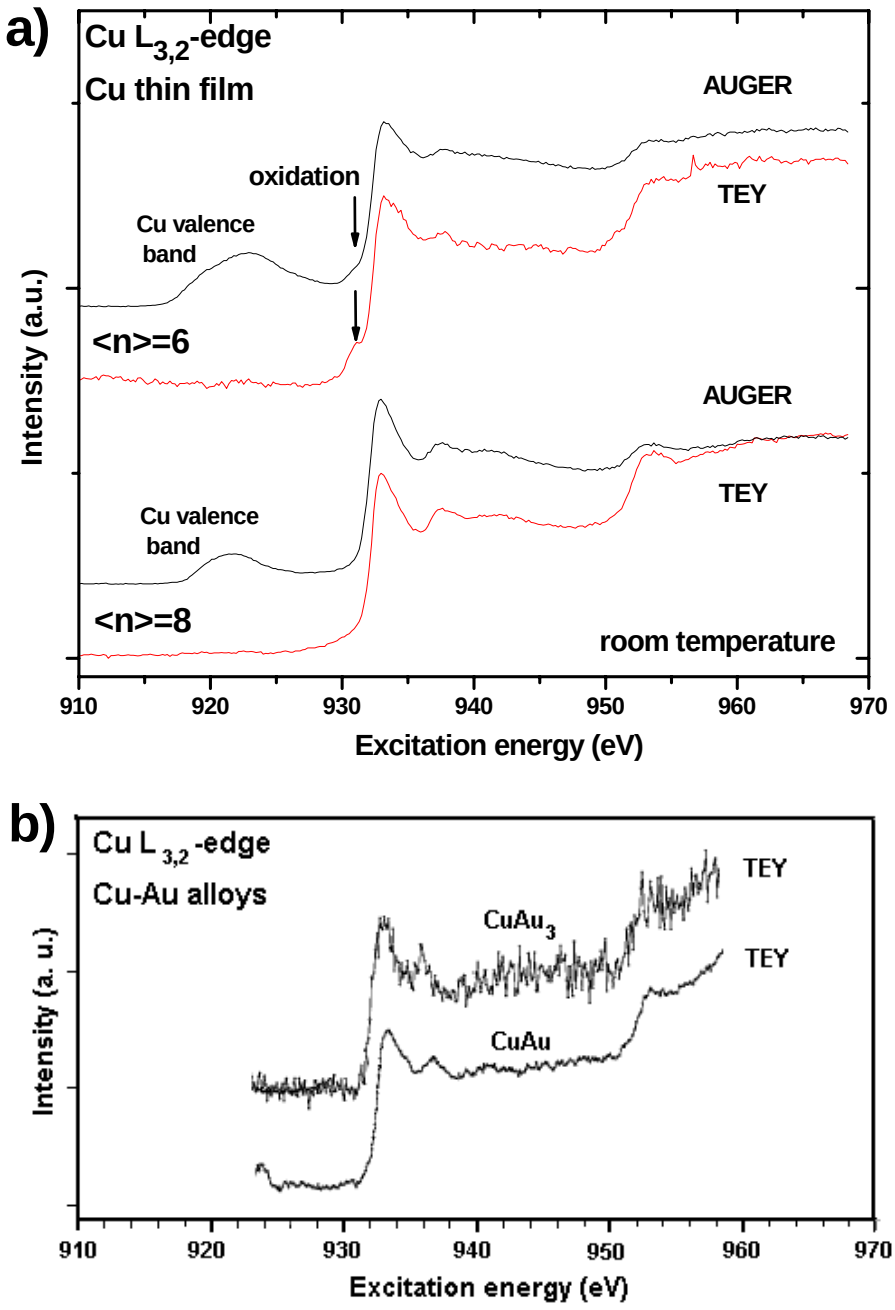

Figure 5.21. Absorption spectra in the XANES regime of Cu $L_{3,2}$ edge. The signal comes from Cu thin film (Cu islands) that results after evaporation of the protective rare gas matrix. The Au painted sample holder has now a temperature around 300K.

The Cu : Au atomic ratios were determined by considering the Cu 3p and Au 4f core level line intensities and the corresponding photoionization cross sections. The $Cu_{<8>}$ sample has a Cu : Au ratio three time larger than the $Cu_{<6>}$ sample.

Similar to Sham investigation, the TEY intensity is lower as Cu becomes more dilute on the Au substrate (see $Cu_{<6>}$ TEY). The absorption and XPS measurements on Cu-Au alloys indicated that the Fermi level shifts towards low energies with decreasing the Cu concentration (-0.4 eV for $CuAu_3$ comparable with Cu single crystal).

The Cu-Au alloys were studied also from the Au perspective [136]. It was shown that Au loses d electrons and gains s electrons. Generally, Au loses charge and Cu gains charge. The more dilute the Cu site is the more d charge is transferred; for Cu Au_3 sample Δn_d(Cu) was calculated to be 0.25.

Conclusions

Cu clusters embedded in Ar are produced by means of pick-up technique and the average sizes of the resulting clusters having about 5-15 atoms/cluster was estimated with help of a mass spectrometer. The spectroscopic investigation was performed on deposited Cu clusters that are embedded in an Ar matrix.

The stability and homogeneity of the cold deposited clusters are monitored by means of **PES** technique. The contamination (C or O) of the deposited samples is low for the first hour after deposition and the Cu/Ar ratio is quite similar for 10-30 Å depths.

The **XANES** (Cu $L_{3,2}$ edge) spectra of deposited clusters indicated different features when compared with the free Cu atoms sample. However, the clusters spectra are rather similar with the Cu fcc single crystal sample, this means that the valence change from $[Ar]3d^{10}4s^1$ to $[Ar]3d^{9.55}4s^{1.45}$ takes place for average Cu cluster sizes smaller than 6 atoms/cluster.

The simulated spectra of Cu_{13} cluster embedded in an Ar shell indicated good correlation with the measured Cu cluster spectra. As expected from the interpretation of the Cu cluster absorption spectra, a bond length contraction occurs. The value is $\mathbf{a}_{ico} = 2.416$ Å for Cu_{13} icosahedral structure.

At room temperature the Ar matrix evaporates and the small Cu clusters coagulated on the gold sample holder surface. The measured absorption spectra (Cu $L_{3,2}$ edge) are very similar with the ones of Cu-Au disordered alloys that are reported in literature.

Chapter 6. Summary

Nanoscience is concerned with the properties, interactions and processing of units containing a countable number of atoms. These units called clusters or nanoparticles have novel electronic, optical and chemical properties by virtue of their nanometer dimensions. The tradition boundaries between physics, chemistry and biology vanish and this convergence of sciences at the nanometer scale creates an exciting multidisciplinary research field.

The main scientific part of the present work was the spectroscopic investigation of deposited metal cluster and semiconductor nanocrystals. Information about the preparation of nanoparticles and their average size distribution are also provided.

In the first part of this study the photoemission investigation of InP nanocrystals was performed. The production together with the investigation of geometric and electronic structure of Cu clusters was presented in the second part of the present work.

Photoemission study on InP nanocrystals

Size selected InP nanocrystals with mean particle diameter of 3-4 nm were synthesized with the help of colloidal chemistry methods by the Weller group, Chemistry Dept., Uni. Hamburg.

The photoelectron spectroscopy technique with synchrotron radiation was applied in order to reveal the changes on the nanocrystal surface that are responsible for the dramatic improvement of the photoluminescence (PL) efficiency (up to three order of magnitude) for the HF etched samples. The photoelectron spectra of the P 2p core level were measured with different excitation energies. This made possible to distinguish between the volume and the surface atoms and to establish the type of chemical bonds existing on the nanocrystal surface.

A systematic study of the InP nanoparticle surface was required in order to reveal the processes responsible for the improvement of PL efficiency. Eight different samples, consisting of HF etched and non-etched nanocrystals capped with different organic ligands (pyridine, TOPO or TOP/TOPO mixture) were prepared and investigated. The analysis of high resolution P 2p core-level spectra (room temperature) confirmed significant changes of the nanocrystal surface structure induced by the post-preparative nanocrystals treatments. The s_1 surface component reflects signal from non passivated sites at the nanoparticle surface that are responsible for the poor PL efficiency. The s_2 surface component originates from surface sites that are efficiently capped (passivated) with TOPO ligands.

There are strong ratio variations in case of different treatments and increasing in s_2/s_1 ratio has a direct but nonlinear response in the improving of PL efficiency. The nonlinear response in the PL yield

could be explained by the fact that generally, already few unpassivated surface sites can lead to poor PL properties.

The photo-assisted treatment of InP nanocrystals with HF solution results in selective removal of the phosphorus atoms from the nanocrystal surface. The surface P atoms have energy states located inside the band gap and provide non-radiative recombination pathways. After HF etching the reconstructed InP nanocrystal surface is terminated mainly with In atoms and is perfectly passivated with tri-octylphosphine oxide (TOPO) molecules.

The present investigation has shown that there is a strong dependence between the InP nanocrystal surface and the PL efficiency. Now, the etching techniques are reproducible and the results are highly luminescent nanoparticles with a rather predictable surface structure.

Photoabsorption on deposited Cu clusters

With a help of a pick up source free and Ar embedded Cu clusters are produced with average size depending on the cluster source parameters (pressure and temperature) and oven temperature. The mass spectra clearly indicated the presence of small Cu cluster consisting of 5-15 atoms/cluster.

The Ar embedded Cu clusters were deposited on the cold substrate (10K) under UHV conditions. The rare gas shell prevents the destruction of Cu clusters at the contact with the substrate or coagulation on the substrate surface. Thin films (few tens of Å) of Cu clusters isolated inside of a rare gas matrix were deposited on the substrate and investigated by means of spectroscopic techniques.

The stability and homogeneity of the cold deposited clusters are monitored with the help of photoelectron spectroscopy technique. The contamination (C or O) of the deposited samples is low with a stable chemical composition and the Cu/Ar ratios do not depend on the film depth.

The XANES curves of small Cu clusters (with average size of 6, 8 and 10 atoms/cluster) were recorded at the Cu $L_{3,2}$ edge and compared with the corresponding ones of the free Cu atoms and the Cu fcc single crystal. The absorption spectra of deposited clusters exhibit several new features when compared with the free Cu atomic sample. However the cluster spectra are rather similar to the Cu fcc single crystal sample and this is a clear indication that the valence change from an atomic configuration of $[Ar]3d^{10}4s^{1}$ to $[Ar]3d^{10-x}4s^{1+x}$ (with $x>0$) occurs for copper clusters consisting of less than 5-6 Cu atoms/cluster.

The small Cu clusters (consisting of less than 15 atoms) have a geometrical structure different that the bulk Cu with fcc symmetry. The bond length of clusters is 6% smaller than in the solid.

At room temperature, the small Cu clusters are no longer protected by the rare gas matrix. They coagulated on the sample holder surface and form alloys.

The previous investigation indicate that the pick up technique is suitable for producing small metal clusters isolated by a shell of rare gas that can be than deposited on a cold substrate and conveniently investigated by means of spectroscopic techniques.

Future work on the field can be focus on the techniques that result in a narrower size selection and improved stability of clusters and nanocrystals. The core shell systems are promising candidates for further studies on nanoscale materials.

Acknowledgements:

First of all, I would like to thank Priv. Doz. Dr. Thomas Möller for the great opportunity of doing a Ph.D. work in his group at Hasylab/Desy. His door was always open and he had always time for my questions. I was enjoying a lot of independence in my work but I also received discrete guidance when needed. His way of doing things characterized by optimism and determination was my driving force for the whole Ph.D. period.

I want to express my special appreciation to postdocs Colm McGinley and Manfred Riedler for guiding my first steps in operating the experimental setup and various discussions. I learned a lot from both of you. Many thanks to postdoc Arun Lobo for helping me on the Cu clusters work and postdoc Christoph Bostedt for illuminating discussion about the absorption spectroscopy and spelling corrections of this thesis.

I want also to express my gratitude for the pleasant work atmosphere: postdocs Tim Laarmann, Hubertus Wabnitz and Joachim Schulz, the other members of our group, also contributed to that.

Successful experiments would not be possible without state of the art design ideas of our engineer, Ralph Döhrmann. Many thanks also for the pleasant work atmosphere and constant technical support.

I am very thankful to the colleagues from the Chemistry Department of Hamburg University for the fruitful collaboration. Special appreciations go to postdoc Dmitri Talapin for the preparation of great nanocrystal samples and useful discussion and postdoc Holger Borchert for valuable comments and help with the beamtime measurements.

Plenty of thanks are addressed to professor A. V. Soldatov and collaborators for the theoretical work on Cu cluster absorption spectra.

Professor A. Rubens B. de Castro voluntarily offered to join me for the night shift of my first beamtime. Many thanks for the pleasant time we spent during measurements and for the useful comments on the InP nanocrystals.

I am indebted to post-docs Robert Nietubyc, Eugen Osiac and Sebastian Vielhauer for helpful discussion and good tips that made my life easier when writing the thesis.

I am very obliged to the member of computer group, Otto Beimgrab, Jan-Peter Kurz, Torsten Kracht, for constant support regarding the software of the beamline and office computers.

I further want to acknowledge the help of Hasylab technical stuff and particularly special thanks to Theodor Cordes, Martin Dommach and Jens Brehling.

For my family and all the people that are not directly mentioned here but contributed to the success of the present work-my best appreciations.

References:

1 H. Haberland, *Cluster of atoms and molecules I*, Springer Verlag, 1994

2 H. Haberland, *Cluster of atoms and molecules II*, Springer Verlag, 1994

3 K. Sattler, J. Mühlbach and E. Recknagel, "***Generation of Metal Clusters Containing from 2 to 500 Atoms"***, *Phys. Rev. Lett*., **45**, 821, (1980)

4 P. Milani and W. A. de Heer, "***Improved pulsed laser vaporization source for production of intense beams of neutral and ionised clusters***" *Rev. Sci. Instrum.*, **61**, 1835, (1990)

5 A. Wucher and M. Wahl, "***The Formation of Clusters During Ion Induced Sputtering of Metals***", *Nucl. Instr. And Meth. B*, **115**, 581, (1996)

6 C. Staudt and A. Wucher, "***The Generation of Large Indium Clusters by Sputtering***", *Phys. Rev. B*, **66**, 075419, (2002)

7 A. P. Alivisatos, "***Semiconductor Clusters, Nanocrystals, and Quantum Dots***", *Science*, **271**, 933, (1996)

8 Y.-W. Mo, D. E. Savage, B. S. Swartzentruber and M. G. Lagally, "***Kinetic pathway in Stranski-Krastanov growth of Ge on Si(001)***", *Phys. Rev. Lett.*, **65**, 1020, (1990)

9 M. Bruchez Jr., M. Moronne, P. Gin, S. Weiss and A. P. Alivisatos, "***Semiconductor Nanocrystals as Fluorescent Biological Labels***", *Science*, **281,** 2013, (1998)

10 N. Tessler, V. Medvedev, M. Kazes, S.-H. Kan and U. Banin, "***Efficient Near-Infrared Polymer Nanocrystal Light-Emitting Diodes***", *Science*, **295**, 1506, (2002)

11 S. Goyal, D. L. Schutt and G. Scoles, "***Noble gas clusters as matrices for infrared spectroscopy. From small clusters to bulk-matrix limit: SF6Ar$_n$, SF6Kr$_n$ and SF6Xe$_n$ with 100≤ n≤10000***", *J. Chem. Phys.*, **102**, 2302, (1995)

12 E. W. Becker, K. Bier and W. Henkes, "***Strahlen aus kondesierten Atomen und Molekeln im Hochvakuum***", *Z. Physik*, **146**, 333, (1956)

13 M. Riedler, A. R. B. de Castro, A. Kolmakov, J. O. Löfken, C. Nowak, A. V. Soldatov, A. Wark, G. Yagovela and T. Möeller, "***Photoabsorption of NaCl clusters at the Na K-edge: Development of the bond length with the cluster size***", *J. Chem. Phys,* **115**, 1319, (2001)

14 *balzers Instruments*, 9496 Balzers, Lichtenstein

15 *Balzer-Pfeiffer GmbH*, Emmeliusstr. 33, D-35614, Asslar, Deutschland

16 *Varian Gmbh*, Alsfelderstr. 6, D-64289 Darmstadt, Deutschland

17 *VAT Deutschland GmbH*, Bretonischer Ring 7, D-85630 – Grasbrunn, Deutschland

18 M. Riedler, "*Innerschalen Photoabsorption und Photoemission von Alkalihalogenid Clustern und Halbleiter Nanokristalen****",*** **Ph.D. thesis,** Uni. Hamburg, (2000)

19 *BOC EDWARDS*, Manor Royal Crawley, West Sussex RH10 9LW, United Kingdom

20 *Vacuum Generators*, Maunsell Road, Hastings, East Sussex TN38 9NN, United Kingdom

21 *LakeShore*, Cryo-Technics, Breslauer Straβe 25, D-64572, Büttelborn, Deutschland, Temperature Diode CT-470-SD and Autotuning Temperature Controller, Model 300 - user's manual

22 Ralph Döhrmann, *Engineer*, Hasylab im DESY, Notkestr. 85, D-22603, Hamburg, Deutschland

23 *Advanced Ceramics Corp.*, 11907 Madison Avenue, Cleveland, Ohio, 44107-5026, USA, Boralectric Heating Elements, internet: http://www.tectra.de/heater.htm

24 *tectra GmbH*, Physikalische Instrumente, Reuterweg 65, 60323 Frankfurt/Main, Universal-Heizernetzteil HC3500.

25 *Cryovac*, Gesellschaft für Tieftemperaturtechnik mbH&Co. KG, Heuserweg 14, D-53842 Troisdorf, Deutschland

26 *Neocera*, Cryo-Technics, Breslauer Straβe 25, D-64572, Büttelborn, Deutschland, LTC-11 Temperature Controller

27 *Omicron Nanotechnology GmbH*, Limburger Str. 75, D-65232, Taunusstein, Deutschland

28 *Caburn MDC GmbH*, Hauptstraβe 117, D-10827 Berlin-Schöneberg, Deutschland

29 *Keithley 6512*, Programmable Electrometer, Keithley Instruments Inc., 28775 Aurora Road, Cleveland, Ohio 44139

30 *Ea 125 Energy Analyzer* User's Guide, version 1.3, (1998)

31 *ISE 5 Sputter Ion Source* User's Guide, version 1.1, (1999)

32 *DAR 400 X-ray Source and Power Supply*, version 1.1, (1998)

33 Stefan Kaesdorf, *Bedienungsanleitung*: "***Reflektron mit Energiefokussierung 2. Ordnung und zweistufiger Ionenextraktion, ausgestattet mit Elektronenstoβ***", Geräte für Forschung und Industrie, Gabelsbergerstr. 59, D-80333 München, tel. 089/52 17 95, Fax 089/5 23 48 16 (1997)

34 W. C. Wiley and I. H. McLaren, "***Time-of-Flight Mass Spectrometer with Improved Resolution***", *Rev. Sci.c Instr.*, **26**, 1150, (1955)

35 W. Gohl, R. Kutscher, H. J. Laue and H. Wollnik, "***Time-of-flight mass spectrometry for ions of large energy spread"***, *International Journal of Mass Spectrometry and Ion Physics*, **48**, 411 (1983)

36 U. Boesl, R. Weinkauf and E. W. Schlag, "***Reflectron time-of-flight mass spectrometry and laser excitation for the analysis of neutrals, ionized molecules and secondary fragments***", *International Journal of Mass Spectrometry and Ion Processes*, **112**, 121, (1992)

37 D. Attwood, *Soft X-rays and Extreme Ultraviolet Radiation, Principles and Applications*, Cambrige University Press, 2000.

38 C. Larsson, A. Beutler, O. Björneholm, F. Federmann, U. Hahn, A. Rieck, S. Verbin, T. Möller, "***First results from the high resolution XUV undulator beamline BW3 at HASYLAB***", *Nucl. Instr. Meth. A***, 337,** 603, (1994)

39 Hasylab, Experimental Stations at Hasylab, *Technischer Report* (Hasylab am Desy, 1997)

40 K. Siegbahn, C. Nordling, A. Fahlman, R. Nordberg, K. Hamrin, J. Hedman, G. Johanson, T. Bergmark, S. Karlsson, I. Lindgren, *ESCA Atomic, Molecular and Solid State Structure Studied by Means of Electron Spectroscopy*, Almquist and Wicksells, Uppsala, 1967.

41 A. Einstein, "***Über einen die Erzeugung und Verwandlung des Lichtes betreffenden heuristischen Gesichtspunkt***", *Ann. Phys*., **17**, 132, (1905)

42 S. Hüfner, *Photoelectron Spectroscopy*, *Principles and Applications*, volume 82 of Springer Series in Solid State Sciences, Springer Verlag, 1996.

43 M. Cardona and L. Ley, *Photoemission in solids I: General principles*, volume 26 of Topics in Applied Physics, Springer Verlag, 1978.

44 L. Ley and M. Cardona, *Photoemission in solids II: Case studies*, volume 27 of Topics in Applied Physics, Springer Verlag, 1979.

45 D. Briggs and J.C. Riviere, *Practical Surface Analysis* edited by M.P. Seah and D. Briggs, John Whiley&Sons, 1983.

46 G. Borstel, "***Theoretical aspects of photoemission***", *Appl. Phys*., **A38**, 193, (1985)

47 J. Pendry, "***Theory of photoemission***", *Surf. Sci*., **57**, 679, (1976)

48 K. A. Bertness, J. J. Yeah, D. J. Friedman, P. H. Mahowald, A. K. Wahi, T. Kendelewicz, I. Lindau, W. E. Spicer, "***Growth structure of chemisorbed oxygen on GaAs(110) and InP(110) surfaces***", *Phys. Rev. B*, **38**, 5406 (1988)- see nanocrystals

49 H. Gant, W. Mönch, "***Electron escape depths in germanium***", *Surf. Sci*. **105**, 217 (1981)

50 D. C. Koningsberger and R. Prins, *X-ray Absorption*, vol 92 of "Chemical Analysis, John Wiley&Sons, 1988

51 J. Stöhr, *NEXAFS Spectroscopy*, Springer Series in Surface Science 25, Springer Verlag, 1992

52 A. Erbil, G. S. Cargill III, R. Frahm and R. F. Boehme, "***Total-electron-yield current measurements for near-surface extended x-ray absorption fine structure***", *PRB*, 37, 2450, (1988)

53 A. Bianconi, "***Surface X-ray Absorption Spectroscopy: Surface EXAFS and Surface XANES***", *Appl. Surf. Sci*., **6**, 392, (1980)

54 D. Bertram, O. I. Micic and A. J. Nozik, "***Excited-state spectroscopy of InP quantum dots***", *Phys Rev. B* **57**, R4265, (1998)

55 A. A. Guzelian, J. E. B. Katari, A. V. Kadavanich, U. Banin, K. Hamad, E. Juban, A. P. Alivisatos, R. H. Wolters, C. C. Arnold, J. R. Heath, "***Synthesis of size-selected, surface passivated InP nanocrystals***", *J. Phys Chem.*, **100**, 7212, (1996)

56 O. I. Micic, K. M. Jones, A. Cahill, A. J. Nozik, "***Optical, electronic and structural properties of uncoupled and closed-paked arrays of InP quantum dots***", *J. Phys. Chem.*, **102**, 9791, (1998)

57 O. I. Micic, S. P. Ahrenkiel, A. J. Nozik, "***Synthesis of extremely small InP quantum dots and electronic coupling in their disordered solid films***", *Appl. Phys. Lett.*, **78**, 4022, (2001)

58 M. Kuno, D. P. Fromm, A. Gallagher, D. J. Nesbitt, O. I. Micic, A. J. Nozik, "***Fluorescence intermittency in single InP quantum dots***", *Nanolett.*, **0**, A-H, (2001)

59 O. I. Micic, J. R. Sprague, C. J. Curtis, K. M. Jones, J. L. Machol, A. J. Nozik, H. Giessen, B. Fluegel, G. Mohs, N. Peyghambarian, "***Synthesis and characterization of InP, GaP and GaInP$_2$ quantum dots***", *J. Phys. Chem.*, **99**, 7754, (1995)

60 U. Banin, C. J. Lee, A. A. Guzelian, A. V. Kadavanich, X. Peng, A. P. Alivisatos, W. Iakolski, G. W. Bryant, A. L. Efros, M. Rosen, "***Size-dependent electronic level structure of InAs nanocrystal quantum dots: Test of multiband effective mass theory***", *J. Chem. Phys*., **109**, 2306, (1998)

61 C. McGinley, M. Riedler, T. Möller, H. Borchert, S. Haubold, M. Haase, H. Weller, "***Evidence for surface reconstruction on InAs nanocrystals***", *Phys. Rev. B*, **65**, 245308, (2002)

62 X. Peng, "***Green chemical approaches toward high-quality semiconductor nanocrystals***", *Chem Eur. J.*, **8**, 335, (2002)

63 O. I. Micic, C. J. Curtis, K. M. Jones, J. R. Sprague, A. J. Nozik, "***Synthesis and characterization of InP quantum dots***", *J. Phys. Chem.*, **98**, 4966, (1994)

64 R. L. Wells, C. G. Pitt, A. T. McPhail, A. P. Purdy, S. Schafieezad, R. B. Hallock, "***Use of Tris(trimethylsilyl)arsine to prepare gallium arsenide and indium arsenide***", *Chem. Matter*, **1**, 4, (1989)

65 D. Talapin, "*Experimental and theoretical studies on the formation of highly luminescent II-VI, III-V and core-shell semiconductor nanocrystals*", **Ph.D. Thesis**, University of Hamburg, 2002.

66 H. Fu, A Zunger, "***InP quantum dots: Electronic structure, surface effects, and the red-shifted emission***", *Phys. Rev. B*, **56**, 1496, (1997)

67 W. Mönch, *Semiconductor Surfaces and Interfaces*, 2nd edition. (Springer Verlag, Berlin, Heidelberg, New York, 1995)

68 W. Mönch, "***Charge transfer from chemical shifts at (110) surfaces of III-V compound semiconductors***", *Solid State Commun.*, **58**, 215 (1986)

69 T. Kendelewicz, P. H. Mahowald, K. A. Bertness, C. E. McCants, I. Lindau, W. E. Spicer, "***Surface shifts in the In 4d and P 2p core-level spectra of InP(110)***", *Phys. Rev. B*, **36**, 6543 (1987)

70 W. G. Wilke, V. Hinkel, W. Theis, K. Horn, "***Surface core-level shifts on InP(110): Experiments and Madelung energy calculations***", *Phys. Rev. B*, **40**, 9824 (1989)

71 W. G. Wilke, R. Seedorf, K. Horn, "***Valence-band offset and interface chemistry of CdS/InP(110)***", *J. Vac. Sci. Technol. B*, **7**, 807 (1989)

72 R. Hesse, T. Chassé, R. Szargan, "***Peak shape analysis of core level photoelectron spectra using UNIFIT for Windows***", *Fresenius J. Anal. Chem*., **48-54**, 365, (1999)

73 G. Hollinger, E. Bergignat, J. Joseph, Y. Robach, "***On the nature of oxides on InP surfaces***", *J. Vac. Sci. Technol.A*, **3**, 2082, (1985)

74 G. Hollinger, J. Joseph, Y. Robach, E. Bergignat, B. Commere, P. Viktorovitch, M. Froment, "***On the chemistry of passivated oxide--InP interfaces***", *J. Vac. Sci. Technol. B*, **5**, 1108, (1987)

75 D. Gallet, G. Hollinger, C. Santinelli, L. Goldstein, "***In situ characterization of InP surfaces after low-energy hydrogen ion cleaning***", *J. Vac. Sci. Technol. B*, **10**, 1267, (1992)

76 G. Hollinger, G. Hughes, F. J. Himpsel, J. L. Jordan, J. F. Morar, F. Houzay, "***Early stages in the formation of the oxide-InP(110) interface***", *Surface Science*, **168**, 617-625, (1986)

77 G. Hughes, R. Ludeke, J. Vac. Sci. Technol.B , "***O 1s studies of the oxidation of InP(110) and GaAs(110) surfaces***", *J. Vac. Sci. Technol. B*, **4**, 1109, (1986)

78 K. A. Bertness, T. Kendelewicz, R. S. List, M. D. Williams, I. Lindau, W. E. Spicer, "***Fermi level pinning during oxidation of atomically clean n-InP(110)***", *J. Vac. Sci. Technol. A*, **4**, 1424, (1986)

79 M. Losurdo, P. Capezzuto, G. Bruno, "***Study of the H_2 remote plasma cleaning of InP substrate for epitaxial growth***", *J. Vac. Sci. Technol. B*, **14**, 691, (1996)

80 H. Borchert, D. V. Talapin, C. McGinley, S. Adam, A. Lobo, A. R. B. de Castro, T. Möller, H. Weller "***High resolution photoemission study of CdSe and CdSe/ZnS core-shell nanocrystals***", *J. Chem. Phys.*, **119**, 1800, (2003)

81 H. Borchert, Dirk Dorfs, C. McGinley, S. Adam, T. Möller, H. Weller, A. Eychmüller, "***Photoemission study of Onion like Quantum Dot Quantum Well and Double Quantum Well Nanocrystals of CdS and HgS***", *J. Chem. Phys*., **107**, 7486, (2003)

82 J. F. Moulder, W. F. Stickle, P. E. Sobol, K. D. Bomben, *Handbook of X-ray photoelectron Spectroscopy*, edited by J. Chastain (Perkin-Elmer, Eden Prairie, MN, 1992)

83 O. I. Micic, J. Sprague, Z. Lu, and A. J. Nozik, "***Highly efficient band-edge emission from InP quantum dots***", *Appl. Phys. Lett*., 68, 3150 (1996)

84 B. H. Erné, D. Vanmakelbergh, I. E. Vermeir, "***The anodic dissolution of InP studied by the optoelectrical impedance method-1.Competition between electron injection and hole capture at InP photoanodes***", *J. Electrochim. Acta*, **38**, 2559, (1993)

85 Z. Hens, W. P. Gomes, "***Photoanodic Dissolution of n-InP: an electrochemical impedance study***", *J. Phys. Chem B*, **104**, 7725, (2000)

86 S. Preussen, M. Herlem, A. Etcheberry, J Jaume, "***The photodissolution of InP***", *J. Electrochim. Acta*, **37**, 289, (1992)

87 S. Haq, A. Carew and R. Raval, "***Nitric oxide reduction by Cu nanoclusters supported on thin Al_2O_3 films***", *J. Catalysis*, **221**, 204, (2004)

88 V. S. Stepanyuk, A. N. Baranov, D. I. Bazhanov, W. Hergert, A. A. Katsnelson, "***Magnetic properties of mixed Co-Cu clusters on Cu(001)***", *Surf. Sci.*, **482-485**,1045, (2001)

89 S. Jayanetti, R. A. Mayanovic, A. J. Anderson, W. A. Bassett, and I.-Ming Chou "***Analysis of radiation-induced small Cu particle cluster formation in aqueous $CuCl_2$***" *J. Chem. Phys*., **115**, 954 (2001)

90 P. A. Montano, G. K. Shenoy, E. E. Alp, W. Schulze, and J. Urban, "***Structure of copper microclusters isolated in solid argon***", *Phys. Rev. Lett*., **56**, 2076 (1986)

91 O. Cheshnovsky, K. J. Taylor, J. Conceicao, and R. E. Smalley, "***Ultraviolet photoelectron spectra of mass-selected copper clusters: Evolution of the 3d band***", *Phys. Rev. Lett.*, **64**, 1785 (1990)

92 E. Ganz, K. Sattler and J. Clarke, "***Scanning tunneling microscopy of Cu, Ag, Au and Al adatoms, small clusters, and islands on graphite***", *Surface Science*, **219**, 33, (1989)

93 M. Lewerenz, B. Schilling and J. P. Toennies, "***Successive capture and coagulation of atoms and molecules to small clusters in large liquid helium clusters***", *J. Chem. Phys.,* **102**, 8191, (1995)

94 A. Bartelt, J. D. Close, F. Federmann, N. Quaas and J. P. Toennies, "***Cold Metal Clusters: Helium Droplets as a Nanoscale Cryostat*****",** *Pys. Rev. Lett.*, **7**7, 3525, (1996)

95 M. Rutzen, S. Kakar, C. Rienecker, R. von Pietrowski and T. Möller, "***Cluster aggregation: a new method for probing atomic and molecular clusters*****",** *Z. Phys. D*, **38**, 89, (1996)

96 D. Ievlev, I. Rabin, W. Schulze and G. Ertl, "***Fluorescence spectroscopy of silver clusters formed in rare gas droplets***"**,** *Eur. Phys. J. D*., 16, 157, (2001)

97 T. Laarmann, "*Elektronische und geometrische Eigenschaften von dotierten Edelgasclustern mit Schalenstruktur*", **Ph.D. thesis**, Uni. Hamburg, (2001)

98 T. Diederich, T. Döppner, J. Braune, J. Tiggesbäumker and K. H. Meiwes-Broer, "***Electron Delocalization in Magnesium Clusters Grown in Supercold Helium Droplets***"**,** *Phys. Rev. Lett.*, **86**, 4807, (2001)

99 O. F. Hagena, "***Condensation in Free Jets: Comparison of Rare Gases and Metals***", *Z. Phys. D*., **4**, 291, (1987)

100 R. Karnbach, M. Joppien, J. Stapelfeldt, J. Wörmer and T. Möller, "***CLULU: An experimental setup for luminescence measurements on van der Waals clusters with synchrotron radiation***", *Rev. Sci. Instrum*., 64, 2838, (1993)

101 O. F. Hagena, "***Nucleation and Growth of clusters in expanding nozzle flows***", *Surf. Sci*., **106**, 101, (1981)

102 U. Buck and R. Krohne, "***Cluster size determination from diffractive He atom scattering***", *J. Chem. Phys.*, **105**, 5408, (1996)

103 M. Lewerentz, B. Schilling and J. P. Toennies, "***A new scattering deflection method for determining and selecting the sizes of large liquid clusters of ^{4}He***", *Chem. Phys. Let.*, **206**, 381, (1993)

104 C. Rienecker, **"***Massenspectroskopie und Innerschalenphotoionisation von Alkalihalogenid-clustern*", **Ph.D. thesis**, Uni. Hamburg, (1998)

105 D. R. Miller, *Atomic and Molecular beam methods*, edited by G. Scoles, **vol. I**, page 14, (1988), Oxford University Press.

106 M. Wolff, "*Untersuchung des Pick-Up-Prozesses verschiedener Alkalihalogenide in Argonclustern*", **Diplomarbeit**, Uni. Hamburg, (1998)

107 A. A. Radzig and B. M. Smirnov, *Reference Data on Atoms, Molecules and Ions*, Springer Verlag, 1995

108 G. E. Froudakis, M. Muhlhauser, S. C. Farantos, A. Sfounis and M.Velegrakis, "***Mass spectra and structures of Cu+Rgn clusters (Rg = Ne, Ar***)", *Chemical Physics*, **280**, 43, (2002)

109 G. Zimmerer, "***Creation, motion and decay of excitons in rare-gas solids***" (U. M. Grassano and N. Terzi, *Soc. Italiana di Fisica, Bologna*, 1987).

110 J. Xie, J. A. Northby, D. L. Freeman and J. D. Doll, "***Theoretical studies of the energetics and structures of atomic clusters***", *J. Chem. Phys.*, **91**, 612, (1989)

111 N. W. Ashcroft and N. D. Mermin, *Solid State Physics*, Holt, Rinehart and Winston, 1976

112 G. Rocker, P. Feulner, R. Scheuerer, L. Zhu and D. Menzel, "***Core Excitation and Decay in Rare Gas Mono- and Multilayers on Metal Surface: Screening, Deexcitation and Desorption of Neutrals and Ions***", *Physica Scripta*, **41**, 1014, (1990)

113 J. Ghijsen, L. H. Tjeng, J. van Elp, H. Eskes, J. Westerink, G. A. Sawatzky, and M. T. Czyzyk "***Electronic structure of Cu_2O and CuO***", *Phys. Rev. B*, **38**, 11322 (1988)

114 M. Martins, K. Godehusen, T. Richter, T. Wolff and P. Zimmermann, "***2p photoelectron spectroscopy of the late 3d transition metal atoms***", submitted *to J. El. Spectr. Rel. Phen.*

115 R. P. Vasquez, "***CuO by XPS***", *Surface Science Spectra*, **5**, 262, (1998)

116 R. P. Vasquez, "***Cu_2O by XPS***", *Surface Science Spectra*, **5**, 257, (1998)

117 F. Forstmann and S. Ossicini, "***The influence of the rare-gas matrix on the electronic levels of isolated atoms***", *J. Chem. Phys.*, **73**, 5997, (1980)

118 K. J. Zeringue, J. ShakhsEmampour, J. C. Rivoal and Martin Vala, "***Atom-matrix interactions: An MCD study of copper atoms in argon***", *J. Chem. Phys.*, **78**, 2231, (1983)

119 G. C. King, M. Tronc, F. H. Read and R. C. Bradford, "***An investigation of the structure near the $L_{2,3}$ edges of argon, the $M_{4,5}$ edges of krypton and the $N_{4,5}$ edges of xenon, using electron impact with high resolution***", *J. Phys. B*, 10, 2479,(1977)

120 E. Rühl, C. Heinzel, A. P. Hitchcock and H. Baumgärtel, "***Ar 2p spectroscopy of free argon clusters***", *J. Chem. Phys*., **98**, 2653 (1993)

121 M. Tchaplyguine, R. Feifel, R. R. T. Marinho, M. Gisselbrecht, S. L. Sorensen, A. Naves de Brito, N. Mårtensson, S. Svensson and O. Björneholm, "***Selective probing of the electronic structure of free clusters using resonant core-level spectroscopy***", *Chemical Physics*, **289**, 3, (2003)

122 W. Wurth, G. Rocker, P. Feulner, R. Scheuerer, L. Zhu and D. Menzel, "***Core excitation and deexcitation in argon multilayers: Surface- and bulk-specific transitions and autoionization versus Auger decay***", *Phys. Rev. B*, **47**, 6697 (1993)

123 A. R. Williams and N. D. Lang, "***Core-level Binding-Energy Shifts in Metals***", *Phys. Rev. Let.*, **40**, 954, (1980)

124 U Arp, K Iemura, G Kutluk, M Meyer, T Nagata, M Sacchi, B Sonntag, S Yagi and A Yagishita, "***2p absorption spectra of atomic copper using the soft X-ray absorption and total photoion yield methods***", *J. Phys. B: At. Mol. Opt. Phys*. **27,** 3389, (1994)

125 M. Grioni, J. B. Goedkoop, R. Schoorl, F. M. F. deGroot, J. C. Fuggle, F. Schäfers, E. E. Koch, G. Rossi, J.-M. Esteva and R. C. Karnatak, "***Studies of copper valence states with Cu L_3 x-ray-absorption spectroscopy***", *Phys. Rev. B*, **39**, 1541, (1989)

126 H. Ebert, J. Stöhr, S. S. P. Parkin, M. Samant and A. Nilsson, "***L-edge x-ray absorption in fcc and bcc Cu metal: Comparison of experimental and first-principles theoretical results***", *PRB*, **53**, 16067, (1996)

127 M. Grioni, M. T. Czyžyk, F. M. F. de Groot, J. C. Fuggle and B. E. Watts, "***Unoccupied electronic states of CuO: An oxygen 1s x-ray-absorption spectroscopy investigation***", *Phys. Rev. B,* **39**, 4886 (1989)

128 M. Grioni, J. F. van Acker, M. T. Czyžyk and J. C. Fuggle, "***Unoccupied electronic structure and core-hole effects in the x-ray-absorption spectra of Cu_2O***", *Phys. Rev. B*, **45**, 3309, (1992)

129 C. R. Natoli, *EXAFS and Near Edge Structure*, volume 27 A. Bianconi, L. Incoccia and S. Stipcich, Springer Verlag, Berlin, 1983.

130 U. Lammers and G. Borstel, "***Electronic and atomic structure of copper clusters***", *Phys. Rev. B*, **49**, 17360, (1994)

131 A. V. Soldatov, Faculty of Physics, Rostov University, Sorge 5, Rostov-na-Donu, 344090, Russia.

132 A. L. Ankudinov, B. Ravel, J. J. Rehr, and S. D. Conradson, "***Real-space multiple-scattering calculation and interpretation of x-ray-absorption near-edge structure***", *Phys. Rev. B*, **58**, 7565 (1998)

133 J. J. Rehr and R. C. Albers, "***Theoretical approaches to x-ray absorption fine structure***", *Reviews of Modern Physics*, **72**, 621, (2000)

134 R. L. Johnston, Computational Chemistry School of Chemistry, University of Birmingham B15 2TT, United Kingdom

135 T. K. Sham, A. Hiraya and M. Watanabe, "***Electronic structure of Cu-Au alloys from the Cu perspective: A Cu $L_{3,2}$-edge study***", *Phys. Rev. B*, **55**, 7585, (1997)

136 M. Kuhn and T. K. Sham, "***Charge redistribution and electronic behavior in a series of Au-Cu alloys***", *Phys. Rev.* B, **49**, 1647, (1994)